Molecular Diffusion in Polyelectrolyte Multilayers

David Šustr

Univ.-Diss.

zur Erlangung des akademischen Grades
"doctor rerum naturalium"
(Dr. rer. nat.)
in der Wissenschaftsdisziplin "Biochemie"

eingereicht an der
Mathematisch-Naturwissenschaftlichen Fakultät
Institut für Biochemie und Biologie
der Universität Potsdam

und

Fraunhofer IZI-BB

Ort und Tag der Disputation: Potsdam, Golm den 10. Dezember 2020

Hauptbetreuer:	Prof. Frank Bier
Betreuer:	Prof. Assoc. Dmitry Volodkin PD Dr. Claus Duschl
Gutachter/innen:	Prof. Frank Bier Dr. Claudia Pacholski Prof. Thomas Groth

Published online on the
Publication Server of the University of Potsdam:
https://doi.org/10.25932/publishup-48903
https://nbn-resolving.org/urn:nbn:de:kobv:517-opus4-489038

Publications and presentations

This thesis presents data that were partially published in peer-reviewed journals. Some of the results were presented at national and international conferences in the form of talks or posters.

Peer-reviewed journals

Sustr, David, Claus Duschl, and Dmitry Volodkin. 2015. "A FRAP-based evaluation of protein diffusion in polyelectrolyte multilayers." *European Polymer Journal* 68: 665–670.

Prokopović, Vladimir Z., Anna S. Vikulina, **David Sustr**, Claus Duschl, and Dmitry Volodkin. 2016. "Biodegradation-Resistant Multilayers Coated with Gold Nanoparticles. Toward a Tailor-made Artificial Extracellular Matrix." *ACS Applied Materials & Interfaces* 8 (37): 24345–24349.

Prokopovic, Vladimir Z., Anna S. Vikulina, **David Sustr**, Elena M. Shchukina, Dmitry G. Shchukin, and Dmitry V. Volodkin. 2017. "Binding Mechanism of the Model Charged Dye Carboxyfluorescein to Hyaluronan/Polylysine Multilayers." *ACS Applied Materials & Interfaces* 9 (44): 38908–38918.

Sustr, David, Antonín Hlaváček, Claus Duschl, and Dmitry Volodkin. 2018. "Multi-Fractional Analysis of Molecular Diffusion in Polymer Multilayers by FRAP: A New Simulation-Based Approach." *Journal of Physical Chemistry B* 122 (3): 1323–33.

Conferences

David Sustr. "A FRAP-based evaluation of cytochrome c diffusion in polyelectrolyte multilayers." *PhD Workshop on Bioelectrochemistry and Bioanalysis* 2014, Luckenwalde, Germany

David Sustr, and Dmitry Volodkin. Poster presentation "A progressive evaluation of diffusion coefficient in polyelectrolyte multilayers by FRAP." *2nd International Conference on Bio-based Polymers and Composites* 2014, Visegrád, Hungary.

David Sustr, Antonin Hlavacek, Claus Duschl, and Dmitry Volodkin. "Assessment of Molecular Diffusion in Polyelectrolyte Multilayer Matrix." *3rd Annual conference and expo on Biomaterials* 2018, Berlin, Germany.

Acknowledgment

The work presented in this dissertation was predominantly conducted at Fraunhofer IZI-BB (a branch of Fraunhofer IBMT until 2014) located in Potsdam–Golm, Germany in a research group of Dr. Dmitry Volodkin with the supervision of Dr. Claus Duschl and later in the research group of Dr. Claus Duschl.

The preparation of the thesis was supported by the Completion Scholarship, awarded by Potsdam Graduate School of University Potsdam, provided with funding from the Graduate Fund of the State of Brandenburg.

Here, I would like to express my sincere thanks to these people:

Prof. Frank Bier, principal supervisor: Thank you for welcoming me to the Fraunhofer institute. Thank you for offering balanced opinions that were based not only on the expertise but open cooperative approach and ability of empathy as well. The combination of a supportive environment and careful criticism in precious moments of our meetings was a stimulating mixture perpetuating me in my efforts.

Prof. Assoc. Dmitry Volodkin, mentor and group leader: Thank you for welcoming me to your research group, for introducing me to the field of polyelectrolyte multilayers and for sharing your research ideas, as well as your visions. Thank you for navigating me around pitfalls on my way. Thank you for your interest in the data collected and your effort in drawing explanations of the effects presented. Thank you for introducing me to the world of science, which is oriented on measurable outcomes and self-presentation that I recognised as an indispensable part of the scientific culture. Thanks to you, I realised that any situation has a bright side that bears a potential for profit. Without your support, I could not reach this milestone.

PD Dr. Claus Duschl, head of the department and supervisor: First, Thank you for setting a stage for my endeavour, supporting me on the administrative side of my work and welcoming me to your research group after my home-group was dissolved. Second, thank you for critical discussions on my results. Thereby I recognised the value of evidence in science, as well as a critical assessment of any aspect of data or any fundament of hypotheses in order to avoid bias and remain consistent. Third, thank you for letting me play on a broad field. Thereby I realised the importance of leadership, and I obtained a chance to independently develop a grip on the management strategies, on the process of scientific endeavour and on culture in the science. Fourth, thank you for letting me experience how various forms of motivation determine the outcomes. I recognised that centric motivation is a good basis for any effort that may prove to be system-progressive. Thank you for providing me these lectures that I found to be of the highest value. Your effort invested in detailed corrections of the thesis draft is gratefully acknowledged.

Dr. Antonín Hlaváček: Thank you for the trust and cooperation that lead to fruitful results. Your unbiased opinions, breadth of scientific knowledge, and unmatched skills were essential for the success. Your maverick approach for science is refreshing and inspiring. Without your involvement, a substantial part of the work would be absent.

Research group of Prof. Robert Seckler at the University of Potsdam, especially Dr. Anja Thalhammer and Dr. Martin Wolff who welcomed me to their lab and allowed me to perform measurements on their equipment.

Finally, I would like to express my sincere thanks to those who were honestly interested in my progress, who shared their professional time with me, who showed me their kind side, or even offered a helping hand: Johannes Bernbeck, Sofia Chatzopoulou, Dr. Nenead Gajovic-Eichelmann, Christian Gehre, Beate Morgenstern, Dr. Marina Neumann, Sandra Stanke, Kamila Trávníčková, and Dr. Axel Warsinke. Moreover, I want to thank Dr. Daniel Connor and Christian Marschner for their engagement in the organisation of free-time events and other comforting side-projects.

Developers of the LibreOffice are gratefully acknowledged.

Abstract

Research on novel and advanced biomaterials is an indispensable step towards their applications in desirable fields such as tissue engineering, regenerative medicine, cell culture, or biotechnology. The work presented here focuses on such a promising material: *polyelectrolyte multilayer* (PEM) composed of hyaluronic acid (HA) and poly(L-lysine) (PLL). This gel-like polymer surface coating is able to accumulate (bio-)molecules such as proteins or drugs and release them in a controlled manner. It serves as a mimic of the *extracellular matrix* (ECM) in composition and intrinsic properties. These qualities make the HA/PLL multilayers a promising candidate for multiple bio-applications such as those mentioned above. The work presented aims at the development of a straightforward approach for assessment of multi-fractional diffusion in multilayers (first part) and at control of local molecular transport into or from the multilayers by laser light trigger (second part).

The mechanism of the loading and release is governed by the interaction of bioactives with the multilayer constituents and by the diffusion phenomenon overall. The diffusion of a molecule in HA/PLL multilayers shows multiple fractions of different diffusion rate. Approaches, that are able to assess the mobility of molecules in such a complex system, are limited. This shortcoming motivated the design of a novel evaluation tool presented here.
The tool employs a simulation-based approach for evaluation of the data acquired by *fluorescence recovery after photobleaching* (FRAP) method. In this approach, possible fluorescence recovery scenarios are primarily simulated and afterwards compared with the data acquired while optimizing parameters of a model until a sufficient match is achieved. Fluorescent latex particles of different sizes and fluorescein in an aqueous medium are utilized as test samples validating the analysis results. The diffusion of protein cytochrome c in HA/PLL multilayers is evaluated as well.
This tool significantly broadens the possibilities of analysis of spatiotemporal FRAP data, which originate from multi-fractional diffusion, while striving to be widely applicable. This tool has the potential to elucidate the mechanisms of molecular transport and empower rational engineering of the drug release systems.

The second part of the work focuses on the fabrication of such a spatiotemporarily-controlled drug release system employing the HA/PLL multilayer. This release system comprises different layers of various functionalities that together form a sandwich structure. The bottom layer, which serves as a reservoir, is formed by HA/PLL PEM deposited on a planar glass substrate. On top of the PEM, a layer of so-called *hybrids* is deposited. The hybrids consist of thermoresponsive poly(*N*-isopropylacrylamide) (PNIPAM) -based hydrogel microparticles with surface-attached gold nanorods. The layer of hybrids is intended to serve as a gate that controls the local molecular transport through the PEM–solution-interface. The possibility of stimulating the molecular transport by near-infrared (NIR) laser irradiation is being explored.
From several tested approaches for the deposition of hybrids onto the PEM surface, the drying-based approach was identified as optimal. Experiments, that examine the functionality of the fabricated sandwich at elevated temperature, document the reversible volume phase transition of the PEM-attached hybrids while sustaining the sandwich stability. Further, the gold nanorods were shown to effectively absorb light radiation in the tissue- and cell-friendly NIR spectral region while transducing the energy of light into heat. The rapid and reversible shrinkage of the PEM-attached hybrids was thereby achieved. Finally, dextran was employed as a model transport molecule. It loads into the PEM reservoir in a few seconds with the partition constant of 2.4, while it spontaneously releases in a slower, sustained manner. The local laser irradiation of the sandwich, which contains the fluorescein isothiocyanate tagged dextran, leads to a gradual reduction of fluorescence intensity in the irradiated region.
The release system fabricated employs renowned photoresponsivity of the hybrids in an innovative setting. The results of the research are a step towards a spatially-controlled on-demand drug release system that paves the way to spatiotemporally controlled drug release.

The approaches developed in this work have the potential to elucidate the molecular dynamics in ECM and to foster engineering of multilayers with properties tuned to mimic the ECM. The work aims at spatiotemporal control over the diffusion of bioactives and their presentation to the cells.

Zusammenfassung

Die Forschung an neuartigen und komplexen Biomaterialien ist unabdingbar für deren Einsatz in begehrten Bereichen wie der Gewebezüchtung, regenerativen Medizin, Zellkultivierung und Biotechnologie. Die hier vorgelegte Arbeit beschäftigt sich eingehend mit einem dieser vielversprechenden Materialien: *Polyelektrolytische Multilayers* (PEM), die aus Hyaluronsäure (*Hyaluronic Acid*, HA) und Poly-L-Lysin (PLL) zusammengesetzt sind. Diese gelartige Polymerbeschichtung ermöglicht es, (Bio-) Moleküle wie z.B. Proteine oder Medikamente zu akkumulieren und diese kontrolliert wieder abzugeben. Durch ihre Zusammensetzung und intrinsischen Merkmale können die PEM der Imitation einer *Extrazellulären Matrix* (ECM) dienen. Diese Eigenschaften machen die HA/PLL-PEM zu einem Anwärter auf verschiedene Bio-Anwendungen, wie den oben genannten. Die vorliegende Arbeit zielt auf die Entwicklung eines Ansatzes zur Einschätzung der multi-fraktionellen Diffusion in Multilayers (1. Teil), und auf die Kontrolle des lokalen molekularen Transports in und aus den Multilayers durch Laser-Stimulation (2. Teil).

Der Aufnahme- und Freisetzungsmechanismus wird bestimmt von der Wechselwirkung zwischen Bioaktiva und den Bestandteilen der Multilayers, sowie allgemein vom Diffusionsprozess. Der Diffusion eines Molekül in HA/PLL-PEM weist unterschiedliche Diffusionsraten einzelner Molekülbestandteile auf. Derzeit existieren nur wenige Ansätze zur Einschätzung der Mobilität von Molekülen in derart komplexen Systemen. Diesem Mangel will die vorliegende Arbeit durch das Design eines neuartigen Evaluations-Instruments abhelfen.
Dieses Instrument bedient sich eines simulationsbasierten Ansatzes zur Evaluation von Daten, die durch die *fluorescence recovery after photobleaching* (FRAP) -Methode erfasst wurden. Der Ansatz simuliert zunächst mögliche Szenarien der Fluoreszenz-Rückbildung, um diese anschließend mit Messdaten zu vergleichen; dazu werden Modell-Parameter angepasst, um suffiziente Vergleichswerte zu erzielen. Fluoreszierende Latex-Partikel verschiedener Größe und eine Fluoresceinlösung wurden als Kontroll- und Vergleichs-Proben verwendet, um die Ergebnisse zu überprüfen. Zusätzlich wurde die Diffusion des Proteins Cytochrom C in eine HA/PLL-PEM ausgewertet.
Dieses Instrument weitet die Möglichkeiten der Analyse von spatiotemporären FRAP-Daten, die aus der multi-fraktionellen Diffusion stammen, erheblich und gleichzeitig ist es vielseitig einsetzbar. Das Instrument hat das Potential, die Mechanismen des Molekültransports weiter zu erhellen, und eine gezielte Steuerung der Freisetzung medikamentöser Wirkstoffe zu ermöglichen.

Der zweite Teil der Arbeit widmet sich der Erstellung eines Systems zur spatiotemporären Wirkstofffreisetzung, das sich die HA/PLL-PEM zunutze macht. Dieses Freisetzungssystem umfasst verschiedene Lagen mit jeweils unterschiedlichen Funktionsweisen, die zusammen ein „Sandwich“ bilden. Die zugrundeliegende Schicht aus HA/PLL-PEM auf einem planaren Glassubstrat dient als Reservoir. Auf diese PEM ist eine Schicht sogenannter Hybride aufgebracht. Die Hybride bestehen aus thermoresponsiven Poly-N-Isopropylacrylamid (PNIPAM) -basierten Hydrogel-Mikropartikeln auf deren Gold-Nanostäbchen gebunden sind. Die Hybridschicht dient in der räumlichen Kontrolle des lokalen Molekültransports als „Schlupfloch“ an der Schnittstelle von PEM und Lösung. Die Möglichkeit der Stimulation des molekülaren Transports durch Bestrahlung mit einem Nah-Infrarot-Laser (NIR) wird hier untersucht.
Von den mehreren getesteten Ansätzen zur Aufbringung von Hybriden auf die PEM-Oberfläche stellte sich die Trocknung als beste Möglichkeit heraus. Funktionalitätskontrollen des hergestellten Sandwiches bei erhöhter Temperatur ergaben eine reversible Volumenphasenübergang der PEM-gebundenen Hybride, wobei die Sandwich-Struktur erhalten blieb. Weiterhin wurde eine effektive Lichtabsorption durch die Gold-Nanostäbchen in den gewebe- und zellschonenden NIR-Spektrumsbereich gezeigt, wobei die aufgenommene Lichtenergie in Wärme umgewandelt wurde. Dadurch wurde eine schnelle und reversible Schrumpfung der PEM-gebundenen Hybride erreicht.
Zuguterletzt wird Dextran als Modellmolekül für den Transport eingesetzt. Dieses wird in wenigen Sekunden – mit einem Verteilungskoeffizient von 2,4 – in das PEM-Reservoir aufgenommen, während es auf langsamere, anhaltende Weise freigesetzt wird. Die lokale Laser-Bestrahlung des Dextran-FITC-haltigen Sandwiches bewirkte eine schrittweise Reduktion der Fluoreszenz-Intensität in der bestrahlten Region.
Das hier vorgestellte Molekül-Freisetzungssystem verwendet die vielzitierte Photoresponsivität von Hybriden auf neuartige Weise. Die Ergebnisse der Untersuchung bedeuten einen Fortschritt in Richtung eines räumlich kontrollierten, nach Bedarf steuerbaren Freisetzungs-Systems, das wiederum den Weg zu einer spatiotemporären Kontrollierbarkeit der Wirkstoff-Freisetzung bereiten könnte.

Die in dieser Arbeit entwickelten Ansätze ermöglichen ein besseres Verständnis der Dynamik in der ECM, sowie die Entwicklung ECM-ähnlicher Multilayers. Die Arbeit hat die spatiotemporäre Kontrolle der Diffusion von bioaktiven Stoffen und deren Präsentation gegenüber Zellen zum Ziel.

Table of Contents

1. Introduction

Molecular diffusion is a phenomenon arising from the thermal motion of molecules in their environment. Diffusion universally appears when molecules, but atoms or particles as well, are translationally free. Diffusion has a dramatic influence on molecular transport on a short distance—typically on micrometer and smaller scale under common conditions. Hence, diffusion is of great importance for a broad range of processes acting on such a small scale. On a macroscopic scale, the diffusion is usually not the most prominent effect of mass transport.

This work focuses on a relatively new type of surface coatings whose fabrication and applicability is substantially influenced by diffusion—the *polyelectrolyte multilayer* (PEM). The modularity and facile control over the parameters of the PEM attracted major attention since its first description (Decher and Hong 1991). One of the parameters, that can be controlled, is the internal mobility of its components. This mobility depends, for example, on the extent of intermolecular interactions between PEM components (Nazaran et al. 2007; Selin, Ankner, and Sukhishvili 2015) or on the molecular mass of the polymers employed (Porcel et al. 2007; Xu et al. 2013). Interestingly, various mobility of the PEM components results in two different modes of PEM build-up, which are known as the linear and the exponential mode (Picart et al. 2002; Lavalle et al. 2004). The abilities of the PEM to uptake, store, and release other compounds of interest are of great importance for the application of these coatings for drug delivery and release (Tang et al. 2006; Dmitry Volodkin, Skirtach, and Möhwald 2010; Jessel et al. 2003). These abilities are controlled, except others, by the mobility of the compound of interest inside the PEM, which in turn is influenced by the mobility of the PEM building blocks (Vogt et al. 2012; von Klitzing and Möhwald 1996).

The work presented here employs a PEM composed of hyaluronic acid (HA) and poly(L-lysine) (PLL) (Picart et al. 2001). The HA/PLL PEM is typically a highly hydrated, gel-like surface coating. Various, preferably charged, (bio-)molecules can be loaded into the HA/PLL PEM at high concentrations while maintaining their native structure and functionality (Kayitmazer et al. 2013; Dmitry Volodkin, Skirtach, and Möhwald 2010). The loaded molecule is able to diffuse in the PEM while it interacts with HA and PLL (Uhlig et al. 2012; Velk et al. 2016). The whole system is in a dynamic state. Due to its qualities, HA/PLL PEM is a promising system for applications in drug release, cell culture, tissue engineering, or regenerative medicine.

This work aims at fabricating a remotely controlled, spatiotemporally addressable release system which employs the PEM as a molecular reservoir. The knowledge on mobility is a cornerstone of understanding the mechanisms of molecular interaction and transport in the PEM, thereby enabling the rational design of such application as the drug release. The value of such knowledge motivated the development of an approach for advanced assessment of molecular mobility in the PEM.

To assess the diffusion rate of molecules present in the PEM, a method called *fluorescence recovery after photobleaching* (FRAP) was employed here (Axelrod et al. 1976; Soumpasis 1983; Picart et al. 2005).

Depending on the complexity of the diffusion phenomenon, simple approaches for the evaluation of the data acquired from a FRAP procedure may meet the needs (Seiffert and Oppermann 2005; Tannert et al. 2009; Gordon et al. 1995; Hauser, Seiffert, and Oppermann 2008). Nevertheless, the diffusion in HA/PLL PEM is a rather complex phenomenon. It is documented that one chemical substance, e.g. PLL, may be present in multiple fractions exhibiting different diffusion rates (Jourdainne et al. 2008). This phenomenon is hereinafter denoted as *multi-fractional diffusion.*

The need for evaluation of data originating from such a system motivated the design of a simulation-based approach for the evaluation of the FRAP data. The aim of this work is assembling a novel tool employing this approach, particularly designed for the evaluation of spatiotemporal data originating from the multi-fractional diffusion obtained from FRAP experiments. It strives to enable a deeper understanding of molecular interactions in the PEM, and thereby it opens a door to the engineering of PEM properties for further applications in sought-after fields such as regenerative medicine, biotechnology, or cell culture. This evaluation approach is further introduced in section 2.1 and the research on this topic is presented in sections 4.1–4.4 of the chapter *Results and discussion*. These sections are based on an article published in a peer-reviewed journal (Sustr et al. 2018). The developed evaluation software is available alongside the article which is published as open-source.

The second part of the chapter *Results and discussion* (sections 4.5–4.10) aims at the application of the HA/PLL PEM as a remotely controlled drug release system. The objective of this research is the fabrication of a system that is able to store a compound of interest and eventually release it in a spatiotemporally controlled manner upon a trigger stimulus—irradiation by IR laser. To achieve this aim, a sandwich structure (hereinafter referred to as *sandwich*) comprising two layers of different functionalities is designed. The bottom layer is formed by the PEM that serves as a reservoir of the compound of interest. The top layer—attached on top of the PEM—is formed by closely packed hydrogel microparticles (hereinafter referred to as *microgels*). The microgels are prepared of *N*-isopropylacrylamide (NIPAM) copolymerised with allylacetic acid (AAA). Thereby, the microgels manifest thermoresponsive property. The microgels are further modified by surface-attached gold nanorods, that are able to transduce NIR light irradiation into heat. The composed particles obtained, hereinafter called *hybrids*, combine the properties of both components—the hybrids shrink upon irradiation by IR laser and they swell again when the laser goes off (Karg et al. 2007; 2009). Finally, the layer of hybrids deposited on top of the PEM is intended to serve as a gate controlling the molecular transport through the PEM-solution interface in a spatiotemporally controlled manner.

Molecular release systems of various designs employing some of the components discussed here (PEM, gold nanorods, PNIPAM, microgels, hybrids) have been already documented in literature (Dmitry Volodkin, Skirtach, and Möhwald 2012; Viger et al. 2014; Tang et al. 2006; Dmitry Volodkin, Skirtach, and Möhwald 2010). The release system proposed here endeavours to comprise a unique combination of capabilities. It aims at locally addressable and remotely controllable planar drug release system. Such a system has the potential to open new possibilities for research in cell culture or anywhere, where the local control over compound release is of interest. The concepts of this system are further introduced in section 2.2. In order to achieve the objective, a way of depositing hybrids onto the PEM surface was

investigated (section 4.6). Experiments testing the functionality of the sandwich under IR laser irradiation (section 4.7), as well as at increased temperature (section 4.8), are presented. The data on molecular transport collected, their interpretation, and conclusions deduced are presented in sections 4.9 and 4.10.

2. Fundamental principles and current state of the research

2.1 Multi-fractional analysis of molecular diffusion by FRAP

Knowledge about molecular diffusion may be of great value since it provides insight into molecular interactions in systems such as living cells, artificial soft matter, or a variety of advanced functional materials. Up to now, the following techniques are commonly used to assess molecular diffusion: FRAP, fluorescence correlation spectroscopy (FCS), and particle tracking. During the FRAP procedure, an area of a fluorescent sample is photobleached in a way that creates a certain pattern. The pattern gradually diminishes over time due to molecular diffusion. Macroscopically, the observed fluorescence intensity in the bleached region recovers. The rate of molecular diffusion can be obtained by mathematical evaluation of the temporal or even spatiotemporal development of the bleached pattern (Axelrod et al. 1976). The second technique—FCS—collects information on temporal fluctuations of fluorescence intensity within the focal volume of a focused laser beam. The acquired data are processed by autocorrelation and analysed by suitable models of diffusion (Elson and Magde 1974). The third technique—particle tracking—is based on following the random walk of a single particle with high precision and afterwards applying the mean square displacement analysis to deduce the underlying diffusion coefficient (Saxton 1997; Ernst and Köhler 2013). These three techniques are complementary in several aspects and have certain limitations as well. While FRAP typically follows an area of a sample of high fluorescence intensity originating from a photobleachable fluorophore, FCS and particle tracking, on the contrary, require highly diluted, stable fluorophores. In the case of FRAP, the evaluation of experimental data employs some kind of image processing that corresponds to the design of the experiment. Therefore, the evaluation procedure usually needs to be adapted to the specifics of the experiment. However, the procedure is typically based on some general concept of FRAP data evaluation. Evaluation of FCS data by the autocorrelation function may seem straightforward, nevertheless, its results are dependent on knowledge of the mechanisms involved and its precise parameters (e.g. geometry of the detection volume, bleaching and photophysical dark states of a fluorophore, viscosity of the local environment) (Müller, Schwille, and Weidemann 2014; Steger et al. 2013).

Here, the FRAP technique was employed since it leads to a rather intuitive data evaluation and since a

standard *confocal laser scanning microscopy* (CLSM) equipment is sufficient for this type of experiment. The most original approach for the analysis of FRAP data was described in the 1970s (Axelrod et al. 1976). In this approach, a circular area within a planar sample is bleached and afterwards, the temporal recovery of the average fluorescence intensity in the area bleached is followed. Three characteristic points of this recovery curve or the complete recovery curve obtained are fitted by an analytical solution that provides an estimation of the diffusion coefficient. The spatial distribution of the fluorescence intensity during the recovery is excluded from the data evaluated. It causes a loss of information but a reduction of the amount of data and simplification of data evaluation as well. This approach for the evaluation of FRAP data was designed for non-scanning fluorescence microscopes and the computational power available at that time. Further development of the FRAP procedure and corresponding evaluation methods have been enabled by the availability of confocal laser scanning microscopes. There are numerous works extending the original evaluation approach by incorporating various phenomena into the evaluation procedure such as system flow (Axelrod et al. 1976; Hallen and Layton 2010), binding kinetics (Hallen and Layton 2010; Weiss 2004), various spatial profiles of the bleached spot (Soumpasis 1983; Frank, Marconi, and Corti 2008), arbitrary geometry of the bleached area (Braeckmans et al. 2003), discrimination between two diffusive fractions (Gordon et al. 1995; Mai et al. 2013), the profile of the laser beam (Hallen and Layton 2010), two-photon excitation (Sullivan, Majewska, and Brown 2015), or exploiting simulations for validation of the analytical approach solution (Mai et al. 2013; Cinquemani et al. 2008).

Later, several evaluation approaches that take a spatial distribution of fluorescence intensity during the recovery into account were described. Usually, a time sequence of spatially uni-dimensional FRAP recovery profiles is fitted by a function obtained as an analytical solution of a certain case of recovery (Jonasson et al. 2010; Uhlig et al. 2012; Picart et al. 2005). The fitting of Gaussian is employed in the work presented here (the *A-approach*) (Seiffert and Oppermann 2005). The applicability of an analytical solution for analysis of FRAP data containing two-fractional (Tannert et al. 2009; Jönsson et al. 2008) or multi-fractional (Hauser, Seiffert, and Oppermann 2008; Vogt et al. 2012) diffusion phenomenon was also demonstrated. However, an extension of the analytical solution from single-fractional to multi-fractional analysis makes the evaluation procedure exceedingly cumbersome.

Simultaneously, an alternative approach, that employs the simulation–optimization tandem method for data evaluation, was slowly emerging (Glotsos et al. 2009; Kubitscheck, Wedekind, and Peters 1998; Irrechukwu and Levenston 2009; Alevra, Schwartz, and Schild 2012; Vinnakota et al. 2010; Sadegh Zadeh 2011; Zadeh, Montas, and Shirmohammadi 2006). Simulations are an elegant tool for identifying a solution, in particular since, nowadays, the computational power of personal computers is sufficient to find solutions for such a problem in a reasonably short period of time. The approach is widely universal —diffusion of multiple species can be simulated without any need to find an analytical solution of the phenomenon. Thus, it is not necessary to reduce the complexity of the system to the stage at which an analytical solution can be established (e.g. bleaching of well-defined pattern, single diffusive fraction, etc.). Despite these merits, the simulation-based approach encompasses quantitatively demanding calculations and handling of an ill-posed inverse problem.

In the work presented here, a new, universal, and easy-to-use tool, which allows the assessment of multi-fractional diffusion by employing the simulation–optimization-based approach (the *S-approach*), is proposed. To deduce as much useful information from an experiment as possible, a spatial dimension of the recovery profiles is fed into the evaluation process. The developed tool focuses on providing a robust solution and high flexibility (arbitrary shape of bleach pattern, multi-fractional solution, low amount of input parameters). Such an evaluation tool can enable a deeper insight into molecular motion and molecular interactions in a simple system, as well as a more complex system such as the polyelectrolyte multilayer. The A-approach and the S-approach are compared by assessment of a model system of single-fractional molecular diffusion using FRAP (section 4.1). The ability of the S-approach to evaluate two-fractional diffusion is documented in section 4.2. This is achieved using fluorescently labelled latex microparticles and fluorescein isothiocyanate (FITC) as test samples. Multi-fractional diffusion of a model protein cytochrome C (CytC), loaded into HA/PLL PEM, is also assessed using the S-approach proposed here (section 4.4).

2.2 Light-addressable gate for molecular transport through solution–PEM interface

2.2.1 PNIPAM microgels

The term *microgel* stands for a gel particle of any shape with an equivalent diameter on a scale of 0.1–100 μm (Alemán et al. 2007). Here, spherical microgels of about 1.5 μm diameter based on hydrated poly(*N*-isopropylacrylamide) (PNIPAM) dispersed in an aqueous environment were employed. The hydrated PNIPAM is renowned for its reversible thermoresponsive properties characterised by a phase transition at the *lower critical solution temperature* (LCST) of about 32°C (Heskins and Guillet 1968). When the temperature is below the LCST, the PNIPAM molecules adopt a conformation of an expanded coil that is highly hydrated. When the temperature rises above the LCST, the PNIPAM chains invert into a globular conformation, and the hydration water is expelled. The gel particles formed of PNIPAM reversibly shrink when the temperature rises above LCST in a process of *volume phase transition* (VPT) (Pelton and Chibante 1986; Pelton 2000). Thanks to their small size, the VPT is relatively rapid in comparison to the rate of PNIPAM mass (Yunker et al. 2014). The diameter of the microgel particles employed in this work decreases by about 3-fold during the phase transition, which corresponds to about a 30-fold reduction of the particle volume. The situation is depicted in the scheme of Figure 1. PNIPAM microgels are usually prepared by free-radical precipitation polymerization from a water solution of monomer, cross-linker, and initiator (Pelton and Chibante 1986). The microgels obtained this way usually comprise a harder core and a softer shell. This gradient of cross-linking density originates from the higher reactivity of the cross-linker relative to the monomer (Wu et al. 1994).

PNIPAM microgels may hold a minor charge which originates from the polymerization initiator. The properties of microgels can be extended by deliberately introducing charged groups. The charge introduction is usually achieved by co-polymerization of NIPAM with other well-designed monomers bearing a charged group (e.g. acrylic acid, allylacetic acid, vinylacetic acid…). This makes the microgels sensitive to ionic strength and to pH as well when the charged group is a weak acid or basis (Hoare and Pelton 2004; Karg et al. 2008; Snowden et al. 1996). Such charged groups slightly alter the thermoresponsiveness of microgels with respect to the thermoresponsiveness of pure PNIPAM (Nerapusri et al. 2006; Schmidt, Hellweg, and von Klitzing 2008; Zavgorodnya and Serpe 2011).

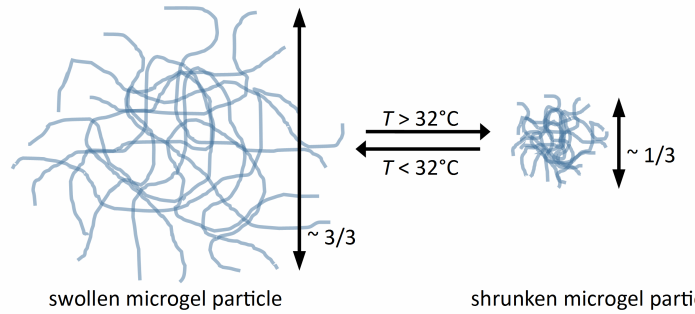

Fig. 1. Scheme depicting the temperature-controlled volume phase transition of a PNIPAM microgel particle. The transition is induced by a change of the molecular conformation of PNIPAM and the release of hydration water. At the temperature below LCST of about 32°C, the microgel is in a highly hydrated swollen state, while at the temperature above LCST, the hybrid is in a shrunken state. The diameter of the microgels employed here reduces by a factor of approximately three upon the transition. Note, that the cross-linking density of the swollen microgel core is higher than the density of its outer shell.

2.2.2 PNIPAM microgel–AuNRs hybrids

The stimulus that triggers the PNIPAM microgel response is temperature. This characteristic can be extended by grafting a photothermal transducer to the microgel. Such a transducer is able to transform light radiation into heat resulting in a local increase of temperature. Organic dyes, gold nanoparticles or specifically gold nanorods can serve as the photothermal transducer (Keblinski et al. 2006; Nguyen et al. 2016). Here, *gold nanorods* (AuNRs) adsorbed on the surface of microgels were employed. The absorption spectrum of AuNRs presents two characteristic bands that correspond to a *transversal surface plasmon resonance* (TSPR) and a *longitudinal surface plasmon resonance* (LSPR). The spectral position of TSPR is weakly influenced by the dimensions of the particle, while the spectral position of LSPR can be tuned in a relatively broad range by varying the ratio of width to length of the AuNRs (Nikoobakht and El-Sayed 2003). The aspect ratio of AuNRs employed here is about 4.4, which shifts the LSPR absorption band to the *near-infrared* (NIR) region (peak absorption centred at about 930 nm, Figure 5). This spectral region corresponds to the NIR window of biological tissues (650–1350 nm) which enables relatively deep penetration of the harmless radiation through biological tissues and living cells (Smith, Mancini, and Nie 2009). The available laser line of 1064 nm wavelength can be therefore employed for effective heating of the AuNRs while enabling their application in cell culture or biological tissues.

By attaching AuNRs to the surface of PNIPAM microgels, so-called AuNR–microgel hybrids (hereinafter referred to as *hybrids*) are obtained. The attachment can be achieved in various ways usually by spontaneous surface adsorption arising from attractive electrostatic forces. Therefore, a complementary charge has to be introduced into microgels and AuNRs. Variations of such an approach were successfully employed in several studies (Gorelikov, Field, and Kumacheva 2004; Karg et al. 2009; 2007; Fernández-López et al. 2015). In this work, the AuNRs possess a positive surface charge while the P(NIPAM-AAA) microgels possess an overall negative charge. The positive charge of the AuNRs originates from their surfactant coating (cetyltrimethylammonium bromide, CTAB) that enables the axial growth of the AuNRs during their synthesis and enhances the colloidal stability of AuNRs. The negative charge of microgels was introduced during particle synthesis by co-polymerization of NIPAM with a relatively high proportion (32 mol%) of allylacetic acid (AAA). A TEM image of the hybrids obtained by this approach is documented in Figure 2. The image documents several microgel particles and a number of AuNRs. Despite somehow inhomogeneous distribution of the AuNRs, the position of the AuNRs relative to the microgels plausibly corroborates that the AuNRs are located on the surface of microgels.

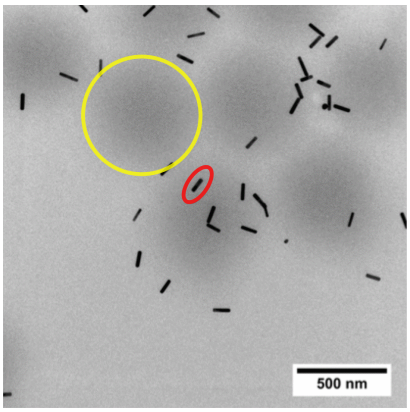

Fig. 2. Transmission electromicrograph of P(NIPAM-acrylic acid) microgel–AuNR hybrids. The microgels are visualized as diffuse round objects of about 0.5 µm diameter. One chosen microgel particle is marked by the yellow circle. The surface deposited AuNRs are visualized as contrasting rod-like objects of about 0.1 µm length. One chosen AuNR is marked by the red oval. The hybrids employed in this work contain 32 mol % of allylacetic acid instead of acrylic acid. Nevertheless, the electromicrographs of these hybrids are equivalent. The image was provided by Dr. Maren Lehmann.

Microgels polymerised around an AuNR, and thereby containing a single nanoparticle in its core, have been reported in the literature as well (Karg et al. 2006). While the microgels containing the AuNRs in their centre are heated from inside, microgels with surface-attached AuNRs are heated from their surface. The heat produced on the microgel surface dissipates into the solvent and the microgel. Due to the dissipation of heat into the solvent, the temperature rises in the microgel may be reduced. Consequentially, an incomplete volume of the microgel particle may undergo the VPT (Lehmann et al. 2018). Nevertheless, the presence of this issue is not supported by the data acquired, as well as by the temperature profiles assumed under the conditions employed here (Keblinski et al. 2006; Nguyen et al. 2016).

The suspension of hybrids provides a characteristic light absorption spectrum (section 3.1). This spectrum consists of two components: actual light absorption, which is mostly caused by the AuNRs, and elastic light scattering, which is mostly caused by the colloidal character of the microgels. The spectrum undergoes characteristic changes when the hybrids shrink or swell. The shrinking of hybrids leads to i) intensifying of light scattering that is indicated by increasing of absorbance at the blue end of the spectra and to ii) red-shifting of the LSPR absorption peak (Karg et al. 2007). The first phenomenon —intensification of light scattering upon hybrid shrinkage—is probably driven by an increase of the refractive index of the microgels due to water excretion from the microgel, that results in increased density of the polymer in the microgel (Karg et al. 2007). Besides this effect, the scattering intensity may vary with changes in the particle size as well. Nevertheless, trends of the scattering intensity variations that arise from changes of the particle size are not straightforward to assess and are beyond the scope of this work (Reufer et al. 2009; Fernández-Nieves, De las Nieves, and Fernández-Barbero 2004). Since the diameter of the employed particles is a few-fold greater than the wavelength of the probe light, our system possibly falls into a transition regime where the Mie scattering approaches the geometric optics. The second phenomenon—red-shifting of AuNRs LSPR band upon shrinking of the hybrids—can be explained by the increasing proximity of AuNRs attached to the microgel surface upon microgel shrinking. This proximity enables plasmon coupling between closely-positioned AuNRs leading to red-shifting of the LSPR absorption band (Karg et al. 2009; Fernández-López et al. 2015).

2.2.3 PEM as a molecular repository

PEM, a particular type of organic surface coatings, can be prepared in a so-called layer-by-layer process that creates the coating by alternated adsorption of oppositely charged molecular building blocks on top of each other (Decher and Hong 1991; Decher 1997). Thus, the thickness of PEM is readily controllable. Various PEMs with thickness from a fraction of nm to tens of μm can be achieved. Two polyelectrolytes of opposite electric charge are the typical building blocks of PEM. The electrostatic interaction makes the polymer molecules affine to each other. By varying the degree of polymerization or the type of the polyelectrolytes, different properties of the resulting PEM are achievable. A thin, condensed, and rigid layers may be achieved or rather thick, highly hydrated gel-like films may be obtained depending on the components of PEM and conditions of preparation. The modularity of this system enables to fabricate PEM films of a broad spectrum of properties with respect to stiffness, dynamics, chemistry, stability, or functionality (von Klitzing 2006; Dmitry Volodkin, Skirtach, and Möhwald 2010; Tang et al. 2006). Due to the nature of electrostatic interactions, which stabilize the PEM structure, PEM films are sensitive to ionic strength and pH as well, when weak electrolytes are incorporated.

The PEM employed here consists of HA of a molecular mass of 357 kDa and PLL of a molecular mass of 15–30 kDa. The HA/PLL PEM has been documented in the literature for the first time in 2001 (Picart et al. 2001). Both components—HA, as well as PLL—are naturally occurring and generally biocompatible. The HA/PLL PEM is a hydrated gel of viscoelastic properties (Bütergerds, Cramer, and Schönhoff 2017). PLL is able to diffuse within the PEM at a substantial rate enabling a charge overcompensation during

the layer-by-layer build-up process due to 'in' and 'out' migration of the PLL molecules. Thereby, the thickness of HA/PLL PEM increases exponentially with increasing number of deposited bilayers (Picart et al. 2002; Porcel et al. 2007). HA is a weak acid (pK_a ~ 3.1; in solution) and PLL is a weak base (pK_a ~ 9.4; in solution) (Burke and Barrett 2003; Wittemann and Ballauff 2004). Hence, the HA/PLL PEM is stable in buffered solutions of moderate pH, while extreme values of pH lead to decomposition of the PEM. HA/PLL PEM is known to be able to uptake a broad range of preferably charged (bio-)molecules and retain them in their native state even in high concentrations (Kayitmazer et al. 2013; Dmitry Volodkin, Skirtach, and Möhwald 2010). Ultimately, the cargo can be spontaneously released again (Kayitmazer et al. 2013; Hsu et al. 2014; Vodouhê et al. 2006). This ability makes the HA/PLL PEM a good candidate for applications in drug release or delivery systems.

2.2.4 Hybrid–PEM sandwich as a molecular gate

This work aims at investigating the applicability of the hybrids for a steerable gate that controls the molecular transport through the solution–PEM interface. The gate is intended to be formed by a layer of closely packed swollen hybrids deposited on top of PEM. The obtained structure is hereinafter referred to as a *sandwich*. Efforts towards such system are already documented in the literature (Vikulina et al. 2015). The concept of the hybrid layer, acting as a steerable gate, is based on the physical hindrance of the molecular transport. At the swollen state, the layer of closely packed hybrids covering the PEM surface should hinder the molecular transport. Upon the increase of temperature above T_{VPT} and consequential shrinking of the hybrids, the layer is anticipated to turn more porous and thereby more permeable for the molecular transport (Figure 3, Figure 4). The extent of surface coverage should control the permeability of the interface. Nevertheless, it is not geometrically possible to separate two environments completely by depositing spheres on their interface, regardless of the number of layers deposited. Therefore, it is assumed that the layer of closely packed hybrids deposited on the interface will engender rather a reduced rate of the molecular transport than a complete cessation of the transport.

For example, a monolayer of closely packed spheres deposited on a surface covers about 91% of the surface (Figure 3). The microgel particles employed here reduce their size upon thermally-triggered shrinking by about three-folds. Such shrinkage theoretically leads to the reduction of the surface area covered by the particles to about 10%.

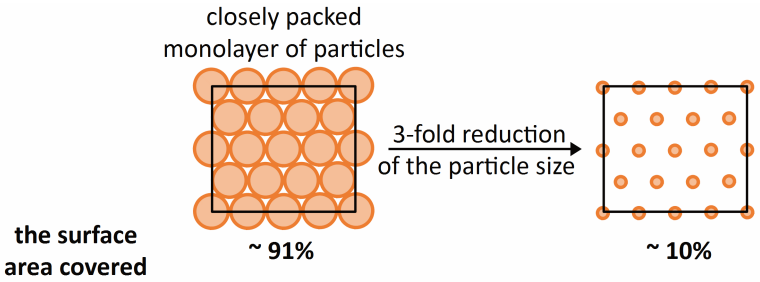

Fig. 3. Schematic diagram (top view) depicting a surface covered by a monolayer of closely packed spherical particles depicted as the orange spheres (left) and the same surface after reduction of the diameter of the particles by three-fold while the position of the particles stays unchanged (right). The area of the surface covered by the particles in the respective cases is denoted in percentage.

However, the swollen PNIPAM microgels are known to be rather soft (section 2.2.1). The shape of the particles may deform upon close packing or their soft shells may partially fuse. This would cause the surface coverage by hybrids at the swollen state to exceed the theoretical limit of 91%.

The rate of molecular transport may be reduced by the presence of the shrunken hybrids on the interface (the open gate kinetics, Figure 4) in comparison to the rate of transport when the hybrids are absent (the non-gated kinetics, Figure 4). However, the transport should be significantly reduced when the hybrids are swollen and the gate is thereby closed (the closed-gate kinetics, Figure 4).

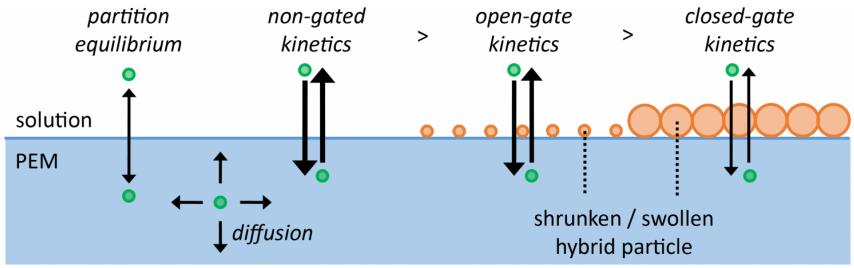

Fig. 4. Schematic diagram (side view) depicting the transport of a model molecule (the green spheres) through the solution–PEM interface. The partition equilibrium and the kinetics of the transport are indicated in the diagram as well as the molecular diffusion in the PEM. The presence of a monolayer of hybrids (the orange spheres), deposited on the PEM surface, and the swelling state of the hybrids are anticipated to influence the kinetics of the molecular transport. The layer of hybrids should thereby act as a gate controlling the molecular transport through the interface.

The ongoing molecular transport is necessarily heading towards an equilibrium state that can be characterised by a *partition constant*. The position of the equilibrium influences the overall loading capacity of the PEM, and thereby it sets a window of applicability of the system. Finally, the diffusion rate of the target molecule in the PEM plays a significant role in the loading process, as well as during the release. The overview of the situations discussed is in Figure 4.

By considering various aspects of the application intended, several prerequisites can be identified. First, low intrinsic permeability of the hybrids for the target molecule is one of the necessary conditions of the effective gating. The transport of the target molecule through the hybrids should be thereby substantially limited in comparison to the free diffusion of the target molecule in solution. Since the polymer structure of the gel matrix can be considered as an immobile scaffold that limits any molecular

transport, this prerequisite is plausibly fulfilled. Second, the gate at its closed state should engender a rate-determining step for the molecular transport in order to be effective as a gate. In other words, the layer of deposited hybrids can effectively perform as a gate only when the bottleneck introduced by the closed gate is narrower than the bottleneck introduced by any other process involved in the molecular transport. Otherwise, when, for example, molecular transport through the solution–PEM interface is the rate-determining step, the effect of opening/closing of the gate would be thereby masked.

The gating effect may be limited to certain experimental settings (e.g. only loading or only releasing of the target molecule) or a certain extent of the transport process (e.g. gradual binding of a target molecule to PEM, molecular transport creating transient concentration gradients). The ability to control the parameters of the drug release system proposed and understanding the mechanisms behind the parameters are respectable challenges. A continuous effort following this way will be rewarded by deeper comprehension of the proposed system enabling its applicability for biotechnology and regenerative medicine.

3. Material and methods

3.1 Material

DMSO	dimethyl sulfoxide, CAS 67-68-5, Fluka
FITC	fluoresceinisothiocyanate CAS 3326-32-7, Sigma
TRIS base	tris(hydroxymethyl)aminomethane, CAS 77-86-1, T1503 Sigma
NaCl	sodium chloride, CAS 7647-14-5, S5886 Sigma
HCl	hydrochloric acid, CAS 7647-01-0, 1.00317 Merck
$NaHCO_3$	sodium bicarbonate CAS 144-55-8, Roth
PEI	poly(ethylenimine), CAS 9002-98-6, 750 kDa, branched, 181978 Sigma, 50wt.% in H_2O, M_w = 94.58 g/mol
HA	hyaluronic acid sodium salt, CAS 9067-32-7, 357 kDa, Lifecore Biomedical 008172, M_w = 401.31 g/mol
PLL	α-poly(L-lysine) hydrobromide, CAS 25988-63-0, 15–30 kDa, P7890 Sigma, M_w = 209.08 g/mol
latex particles	surface carboxylated fluorescent latex particles, 0.116 ± 0.005 μm diameter, Polysciences 16662, Ex/Em 441 nm/486 nm, 2.5% (*w*/*v*) aqueous suspension
	surface carboxylated fluorescent latex particles, 0.042 ± 0.007 μm diameter, Polysciences 16661, Ex/Em 441 nm/486 nm, 2.5% (*w*/*v*) aqueous suspension
	surface aminated latex particles, 0.2 μm diameter, Micromod 01-01-202, 5.8×10^{12} particles/mL, 25 mg/mL, solid density 1.03 g/cm^3, charge density 4 μmol/g
dextran-FITC	Molecular mass of 4 kDa (TdB consultancy, freeze-dried, RT stored); 10 kDa, 70 kDa (freeze-dried, 4°C stored)
hybrids	poly(*N*-isopropylacrylamide-*co*-allylacetic acid) (P(NIPAM-AAA)) microgels, surface modified with AuNRs. Prepared by Dr. Maren Lehmann at TU Berlin (group of prof. R. von Klitzing). Synthesis by precipitation polymerization from aqueous solution of NIPAM (64.51 mol%), AAA (32.25 mol%), *N*,*N*'-methylenebis(acrylamide) (3.23 mol%), potassium persulfate (0.02 mol%). Microgel hydrodynamic radius: ~750 nm at 20°C, ~250 nm at 45°C. T_{VPT} ~ 41°C. To obtain the hybrids, microgels are surface modified by AuNRs (102 nm × 23 nm, LSPR ~ 900 nm, stabilised by 0.1 mM CTAB, synthesized by a partner in Australia) by simple surface adsorption arising from the opposite charge of the components (Lehmann et al. 2018) and purified by centrifugation. In average, 9 AuNRs are attached per one microgel particle. Stock water suspension is of about 0.25 mg/mL microgel concentration, stored at 4°C.

	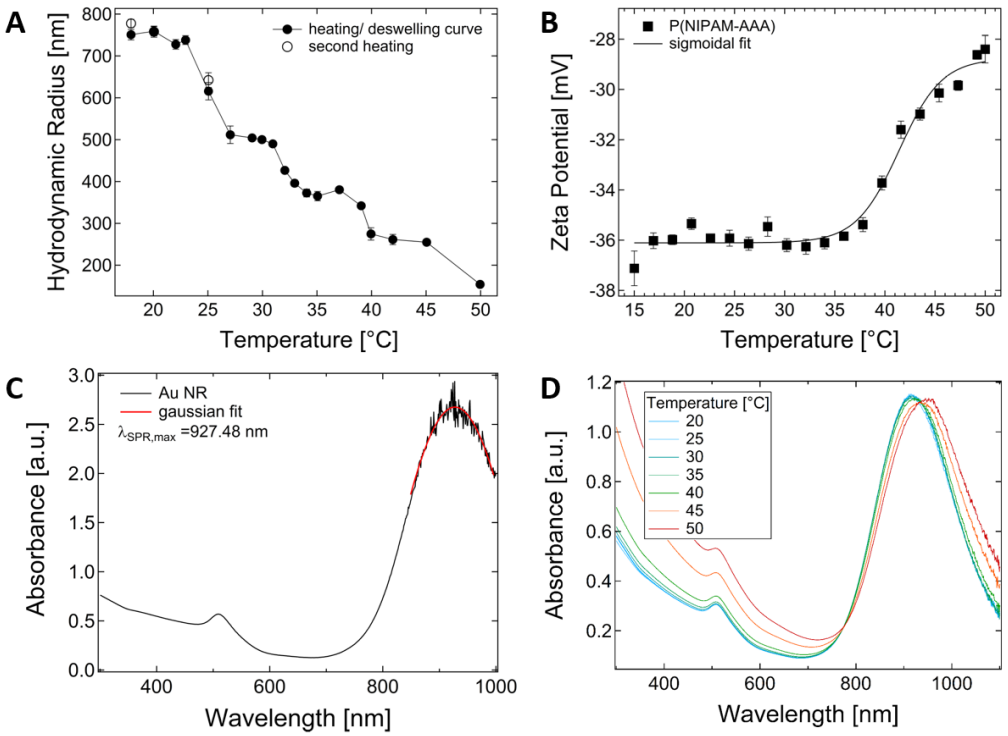 *Fig. 5. A: hydrodynamic radius of plain P(NIPAM-AAA) microgels in water suspension as a function of temperature; assessed by DLS. B: zeta potential of plain P(NIPAM-AAA) microgels in water suspension as a function of temperature; assessed by electrophoretic light scattering. The plot indicates that T_{VPT} = 41°C. C: absorption spectra of AuNRs in suspension. The AuNRs are employed for the fabrication of the hybrids by attaching them onto the surface of P(NIPAM-AAA) microgels. D: absorption spectra of the hybrids in suspension. The data provided by Dr. Maren Lehmann.*
Hellmanex III	glass cleaning solution, Hellma Analytics
buffer	10 mM TRIS, 15 mM NaCl, pH set to 7.4 by 1 M HCl, 0.22 μm filtered

3.2 Modification of latex particles by FITC

Commercial latex particles with amino-groups exposed at the surface were modified by FITC. Primarily, the water dispersant of particles was changed to 0.1 M carbonate buffer pH9.0: 50 μL of particle suspension was centrifuged (12000 g, 2 min), the supernatant discarded, pellets re-suspended in 50 μL of the carbonate buffer by a vortexer and in an ultrasound bath (3 × 10 s).

Afterwards, 19.47 μL of 1 mg/mL FITC in DMSO was added to the sample to reach a nominal labeling ratio of 10:1 (FITC: amino groups on the particle surface), shaken overnight at room temperature in darkness.

Afterwards, free FITC label was removed. Therefore, the sample was centrifuged (12000 g, 30 min), the supernatant was discarded, water was added to reach 50 μL of final volume and the sample was re-suspended with help of a vortexer and an ultrasound bath (3 × 10 s). This separation cycle was repeated five times. The diameter of unmodified and FITC-labelled particles were determined by *dynamic light scattering* (DLS) (Zetasizer Nano ZS 633 nm, Malvern, UK). The data indicate that the modification did

not alter the size of particles any substantially and the particle suspension after the modification is well-stabilized.

3.3 Preparation of a sample for FRAP experiment

Two glass slips (#1, ~ 0.15 mm thick, Menzel, Germany) were employed as a top and a bottom window of a thin chamber. A frame of double-sided adhesive tape (3M, USA) was used to attach the glass slips together in a defined distance while creating the sealed chamber between them. The thickness of the adhesive tape, and thereby the height of the chamber, is about 0.08 mm. Usually, 4 μL of a sample were dispensed and trapped between the glass slips. The chamber protects the sample from evaporation, flow of liquid and it permits water bath sonication of a sample as well.

3.4 FRAP measurements

FRAP measurements were performed using CLSM setup (Zeiss LSM510 meta / Axiovert 200M, Zeiss, Germany) employing the 488 nm line of an Ar-ion laser or the 405 nm line of a diode laser. An objective of low numerical aperture (Zeiss LD-Achroplan 20x/0.4 corr) was deliberately employed for FRAP measurements in order to achieve a *z*-profile of the focused laser beam close to cylindrical geometry.
A chosen *region of interest* (ROI) within the sample was primarily twice scanned at low laser intensity to obtain a reference image. Afterwards, a rectangular area within the ROI was bleached by scanning the laser at its full power fifty or four hundred times (lasting a few seconds usually) over the area to be bleached. Afterwards, the recovery process was recorded by scanning at low laser intensity over the ROI thirty or sixty times. The time between successive scans was chosen according to the expected rate of diffusion to 0.5 s or 1.0 s. Pixel scanning time was chosen as long as possible (1.6 or 3.2 μs, respectively) to accumulate enough signal while reducing signal noise. Recorded images have a *xy*-resolution of 512 pixels × 512 pixels. The actual dimension of ROI was adjusted according to the expected rate of diffusion so that both fast and slow recovery processes are observable within the chosen area. The bleached region was 15 pixels × 512 pixels large. The width of this region (15 pixels) provides a good compromise between a region wide enough to accumulate a sufficient amount of bleached molecules and a region narrow enough for approximating the recovery profiles by the Gauss function. In an ideal case, the recovery profiles are of Gaussian shape when the foregoing bleaching instantaneously creates an infinitely thin bleached region. Bleaching of a rectangular area with the long side being parallel to the scanning direction of the microscope (*y* axis) is the most time-efficient mode of bleaching achievable with the aforementioned CLSM equipment. This bleaching mode has been employed here. The time-lapse photomicrographs acquired during one FRAP experiment are saved in one file including information on the instrumental setup. The experimental setup allowed us to observe a 1D diffusion process in a limited 3D environment. Thanks to this spatial reduction, the amount of data to be evaluated is significantly reduced and an evaluation is faster.

3.5 FRAP data pre-processing

The acquired time-lapse photomicrographs of one FRAP experiment are cropped in the direction perpendicular to the direction of recovery (about 128 pixels on both sides) to limit edge effects emerging during the recovery process. Afterwards, the photomicrographs are averaged along the same dimension, which results in a uni-dimensional raw FRAP profiles (ImageJ 1.51, Wayne Rasband, NIH). Please note, image lines, which were included in averaging, contain redundant information. Hence, a signal-to-noise ratio increases while vital information remains untouched by the averaging. Resulting profiles were transferred into spreadsheet templates (Excel 2010, Microsoft) for data corrections and further analysed.

The stack of raw FRAP profiles originating from one FRAP experiment is primarily normalized and corrected for spatial inhomogeneities of fluorescence (post-bleach profiles are divided by a master pre-bleach profile which was prepared by averaging ten spatiotemporally near points of pre-bleach profiles). Post-bleach profiles are afterwards corrected for unwanted bleaching which occurs during scanning and consequential edge effect (every post-bleach profile is multiplied by an optimized constant to reach a value of the profile baseline close to unity). Edge effects caused by diffusion from outside the ROI may appear when unwanted bleaching was significant. The area affected by this edge effect is identified and excluded from further evaluation. A schematic overview of an photomicrograph time-lapse transformation into FRAP profiles is outlined in Figure 6.

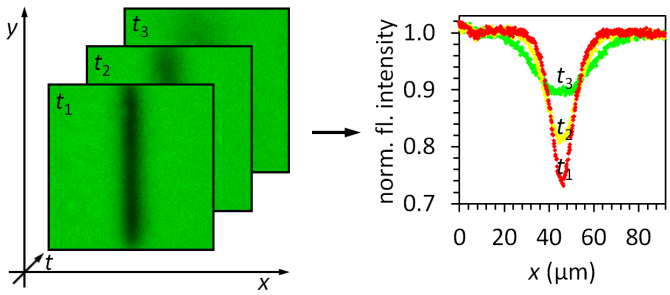

Fig. 6. Schematic representation of a time-lapse of FRAP images recorded during the recovery process (left) and the corresponding corrected 1D FRAP profiles (right) extracted from the images.

3.6 FRAP data evaluation by the A-approach

As it is described in literature (Seiffert and Oppermann 2005), FRAP recovery profiles of a single fraction can be approximated by a Gauss function, which is an analytical solution of a recovery process following an instantaneous bleaching of an infinitely thin region. Measurements should adhere to these requirements to keep evaluation by this approach reliable. Deviations from this approximation can be partially amended by an introduction of the time shift t_0 (as it will be described in equation 3 and equation 4).

Corrected FRAP profiles are primarily fitted by a Gauss curve defined as:

$$I(x,t)=I_0(t)-A(t)\cdot\exp\left(\frac{-x^2}{2w^2}\right) \qquad \text{eq. 1}$$

where $I(x, t)$ denotes the fluorescence intensity at a distance x from the centre of the dip and at a time point after bleaching t, $I_0(t)$ stands for the fluorescence intensity of the background (ideally its value is constant over the entire ROI and close to 1), $A(t)$ denotes the depth of the dip at the time t, w denotes a width of the Gaussian between inflection points. All four parameters (width of the dip, spatial position of the dip, depth of the dip, intensity of the background) are free for fitting with every single FRAP profile during Gaussian fitting. Fitting is performed as a minimization of the *sum of squared deviations* (SQD) of every single measured FRAP profile from its respective Gaussian fit. After fitting a Gaussian function to every FRAP profile, the diffusion coefficient D is evaluated as a half of slope of the plot w^2 versus t:

$$D=\frac{w^2}{2t} \qquad \text{eq. 2}$$

This plot is linear only in case of single-fractional diffusion. When more fractions are involved in the diffusion process, this plot deviates from a linear behaviour and its slope may serve only as a hint of the rate of diffusion of a major fraction. The slope at the onset of this plot rather corresponds to the recovery of fast fractions, while at later time points (when the influence of fast fractions disappears) the slope rather represents slower fractions.

The dimensionality of diffusion d may be evaluated from the slope of the plot $\log(A)$ versus $\log(t + t_0)$:

$$\log(A)=\frac{-d}{2}\cdot\log(t+t_0)+const. \qquad \text{eq. 3}$$

where the newly introduced parameter t_0 refers to a time shift correcting deviations from the approximation of instantaneous bleaching of an infinitely thin region. The time shift can be found by varying its value until the plot $\log(A)$ versus $\log(t + t_0)$ become linear (here implemented as maximization of the coefficient of determination of an expected linear function). Nevertheless, because also this plot tends to deviate in a case of multi-fractional diffusion, usually only the first 10 points were used for evaluation of d. Evaluation of D and d from fitted Gaussians is graphically depicted in Figure 7.

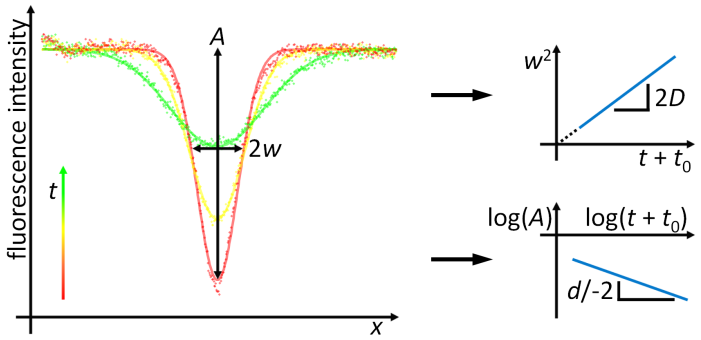

Fig. 7. Schematic representation of the main steps of single-fractional analysis using the A-approach. First (left), Gauss functions are fitted into corrected 1D FRAP profiles. Second, the diffusion coefficient D (right top) and the dimensionality of diffusion d (right bottom) are obtained from appropriate time sequences of the parameters.

The relative amount of the immobile fraction K_{rel} is evaluated from the time development of the dip depth $A(t)$ by fitting the function:

$$A(t)=\frac{M}{4\pi D(t+t_0)^{d/2}}+K \qquad \text{eq. 4}$$

where $A(t)$ denotes the depth of the dip at time point t, M stands for the overall reduction of fluorescence intensity caused by bleaching, D is the diffusion coefficient, t denotes time after bleaching, t_0 is the correction for the time shift, d denotes the dimensionality of diffusion and K denotes the partial depth of dip attributed to the immobile fraction. Values of D and d are transferred from the previous evaluations (eq. 2, eq. 3) and fixed during the fitting. D and d tend to be underestimated when a substantial amount of the immobile fraction is present. At the same time, a presence of these values during fitting is essential for estimation of an amount of the immobile fraction. The lower limit of the d value is 1, since values lower than 1 do not reflect reality. M, t_0 and K are free parameters for fitting. The input values $A(t)$ are acquired directly from the FRAP profiles, not from fitting the Gaussian function, because the assessment of immobile fraction amount must be independent from the evaluation of D as much as possible. Fitting is performed as a minimization of SQD between measured data and fitted function.

Afterwards, K_{rel} is obtained by relating K to the depth of the dip of the first post-bleach FRAP profile:

$$K_{rel}=\frac{K}{A_0} \qquad \text{eq. 5}$$

where K_{rel} stands for the relative amount of the immobile fraction, K denotes the depth of the dip attributed to the immobile fraction resulting from equation 4 and A_0 denotes the depth of the dip just after the bleaching.

Such an approach for the evaluation of the amount of the immobile fraction requires not more than two

fractions presented in the sample—a single mobile fraction with a certain *D* and possibly an immobile fraction as well. Otherwise, an evaluation of the amount of the immobile fraction would give only approximate results. After the information on amount of the immobile fraction is obtained, a contribution of this fraction can be subtracted from the raw FRAP profiles—from the input data. This step is based on an assumption, that the FRAP profile of the immobile fraction is time invariant and the shape of the immobile fraction profile is identical to the first post-bleach FRAP profile. Thus, the contribution of the immobile fraction may simply be subtracted from the raw FRAP profiles and the whole evaluation procedure can then be repeated. Results of this repeated evaluation allow extracting D of the pure mobile fraction.

3.7 FRAP data evaluation by the S-approach

3.7.1 General description

The S-approach consists of two consecutive steps: 1) simulation of possible single-fractional scenarios of fluorescence recovery; 2) fitting a linear combination of the single-fractional scenarios to the measured recovery profiles. The corrected post-bleach FRAP profiles (as described in section 3.5) serve as input data for the evaluation performed by the S-approach.

Primary, the first post-bleach profile is used as a starting point for the simulation of the temporal development of recovery profiles within a chosen range of diffusion coefficients. The simulation employs Fick`s law for estimation of the diffusion process observed. Calculations are based on the finite-difference method with a spatial mesh matching the resolution of measured data (usually hundreds of nm) and a temporal mesh much finer than the repetition time of scanning during the measurement (usually 0.1 ms). To further improve the numerical stability of the simulation, a five-point stencil method is applied on the input data (the profile of preceding time step) of the simulation engine. To suppress possible edge effect during simulation (diffusion may substantially spread out of the ROI) the spatial size of simulated profiles may be extended during simulation and afterwards cropped to the original size to be saved (usually a 3-fold extension of the spatial size was used). Output data of the simulation are single-fractional post-bleach recovery profiles in a 2D matrix (one spatial and one temporal dimension), saved separately for every simulated diffusion coefficient. The spatiotemporal dimensions of output data from simulation match the dimensions of the experimentally acquired data.

Second, the data of the real measurement are compared with possible linear combinations of simulated single-fractional recovery scenarios until the best fit (characterised by minimization of the sum of squared deviations) is found. A searching engine is based on the *non-negative least squares* (NNLS) algorithm regularized by the Tikhonov–Phillips method, which is a common approach in solving inverse ill-posed problems (Provencher 1982). Solving such a problem typically requires finding a balance between the amount of meaningful information used as input for an evaluation and the amount of output information. In other words, we are searching for the simplest solution that explains most of our

observed data. The need for the simplest solution is in accordance to the principle of parsimony in a meaning of Occam`s razor. The employed Tikhonov–Phillips regularization penalizes more complicated solutions and thus promotes simpler solutions.

When the program presented here finds an optimal match between real measurement and linear combination of simulated data, three sets of results are obtained: FRAP profiles of a composed model, corresponding residuals and the relative amount (weight) of diffusing fractions. A schematic overview of evaluation process performed by the S-approach is shown in Figure 8.

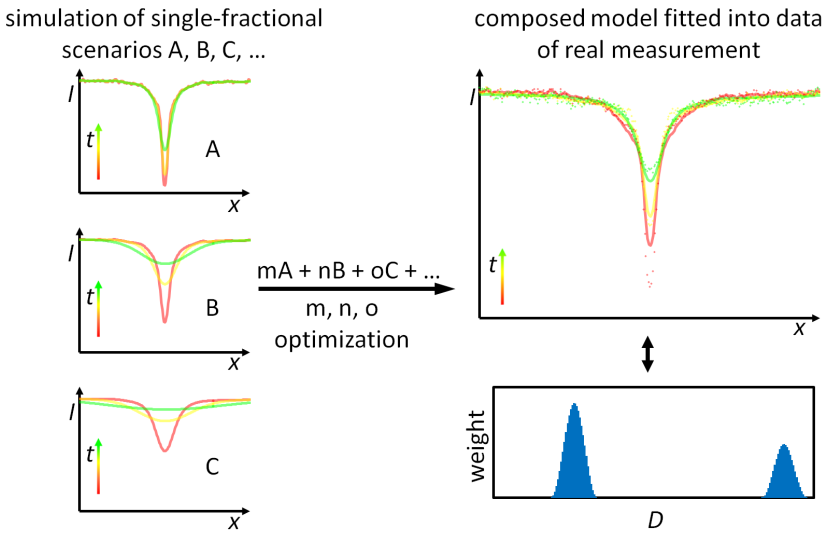

Fig. 8. Schematic representation of the S-approach for FRAP data evaluation. Primary, possible scenarios of FRAP profile development are simulated using a certain set of diffusion coefficients (left). Second, the parameters of a linear combination of simulated single-fractional scenarios are optimized until a sufficient fit between the composed model (solid line) and measured data (points) is found (right top). Resulting optimized parameters correspond to the relative weights of diffusing fractions with corresponding diffusion coefficients D (right bottom).

All calculations of the S-approach are performed within a newly designed Java-based program with a graphical user interface. Main aspects of this program are universality towards evaluated data, simplicity of use and independence on the operating system used. This program is designed to evaluate unidimensional FRAP profiles for the characterisation of unidimensional diffusion. It ensures simplicity and swiftness of the evaluation. Nevertheless there are no theoretical restrictions towards evaluation of data of higher dimensionality with an equivalent evaluation procedure.

3.7.2 Mathematical apparatus

A set of experimentally measured FRAP profiles $m(x, t)$ with the distribution of diffusion coefficients $p(D)$ can be written as:

$$m(x,t) = \int p(D)\, c(D,x,t)\, dD \qquad \text{eq. 6}$$

where x denotes a spatial coordinate and t the time. The term $c(D, x, t)$ describes the concentration of any component with diffusion coefficient D at position x and time t and is given by the Fick's law:

$$\frac{\partial c}{\partial t} = D \frac{\partial^2 c}{\partial x^2} \qquad \text{eq. 7}$$

A finite difference method was utilized for iterative computation of $c(D, x, t)$ from any starting condition $c(D, x, t = 0)$. The concentration c in time $t + \Delta t$ at position x can be written:

$$c(x, t+\Delta t) = c(x, t) + D \Delta t \, gradient(x, t) \qquad \text{eq. 8}$$

The distribution of diffusion coefficient $p(D)$ can be approximated by a set $P(D)$ of N discrete values referring to the interval of diffusion coefficients between D_{min} and D_{max}. Utilizing this approximation, equation 6 can be transformed into a least square problem allowing the estimation of $P(D)$:

$$Min \sum_x \sum_t \left[m(x,t) - \sum_{i=1}^{N} P_i c(D_i, x, t) \right]^2 \qquad \text{eq. 9}$$

The summation is over all data points of all concentration profiles within the spatial and time interval considered for analysis. Non-negativity of the $P(D)$ coefficients was achieved by the NNLS algorithm from Lawson and Hanson (Lawson and Hanson 1995).

Regularization has found widespread applications, for example, for the size-distribution analysis by dynamic light scattering as well as for processing data of analytical ultracentrifugation experiments (Provencher 1982; Phillips 1962; Johnson and Straume 1994). Here, regularization was introduced to avoid non-realistic oscillations in estimated set of P values. In this way equation 9 was extended by adding a Tikhonov–Phillips regularization term (Phillips 1962), such that the value of integrated second derivative of the distribution $P(D)$ serves as an additional penalty in the fit optimization:

$$Min \left\{ \sum_x \sum_t \left[m(x,t) - \sum_{i=1}^{N} P_i c(D_i, x, t) \right]^2 + \lambda \sum_{i=2}^{N-1} \left(P_{i-1} + P_{i+1} - 2 P_i \right)^2 \right\} \qquad \text{eq. 10}$$

From the set of all possible distributions $\{P(D)\}$ that lead to a statistically acceptable fit of the raw data, the constrain of Tikhonov–Phillips regularization based on the second derivative term reflects our assumption that the actual distribution of diffusion coefficients has no sharp peaks. The regularization penalty leads to an increase in the variance σ of the fit with an increasing magnitude of the regularization parameter λ. The relative variance increase $F = \sigma(\lambda)/\sigma(\lambda = 0)$ follows a Fisher distribution and can be exploited to adjust the magnitude of the regularization parameter such that the quality of

the regularized fit still remains statistically indistinguishable from the unconstrained best fit on a given confidence (Johnson and Straume 1994; Bevington and Robinson 2003). Because of a large number of data points, the effect of the constraint on the number of degrees of freedom can be neglected.

3.8 Preparation of HA/PLL PEM loaded with CytC

The PEI(HA/PLL)$_{23}$HA polyelectrolyte multilayer deposited on a glass fibre (0.1 mm in diameter, 1 cm long) was prepared by the layer-by-layer assembly. Glass fibre (cleaned by 2% Hellmanex III, followed by 1 M HCl and water) was sequentially incubated in solutions of appropriate polyelectrolytes with intermediate washing steps using an automated dipping robot (DR3, Riegler & Kirstein) until the PEI(HA/PLL)$_{23}$HA composition was achieved. Each incubation of the substrate in 0.5 mg/mL solution of appropriate polyelectrolyte lasted 10 minutes. The intermediate washing in buffer consisted of three steps lasting for 3 min each. The multilayer assembly and further experiments with multilayers were performed in 10 mM TRIS buffer of pH 7.4 supplemented with 15 mM NaCl. The multilayers were loaded with FITC labelled CytC by incubating them in about 50 μL of 30 μM buffer solution of FITC labelled CytC for an hour at RT. Afterwards, the fibre was washed three times with the buffer and further kept in 100 μL of the buffer for series of FRAP experiments performed at progressing time after loading.

3.9 Preparation of HA/PLL PEM employed in the sandwich

Buffer solutions of 0.5 mg/mL concentration of PLL and HA were freshly prepared by diluting frozen aliquots. PEI solution was usually reused from previous runs since this solution is used only briefly during the first contact with clean glass slips. A Teflon holder for glass slips was pre-cleaned to get rid of scales of old PEMs by sonication in 1 M HCl. Eight glass slips (14 mm diameter, #1, borosilicate glass D263M, Schott AG) were placed into the holder. The holder was placed into a glass beaker filled with a sufficient amount of 2% Hellmanex III solution in DI water. The cleaning by Hellmanex proceeded at 60°C, 15 min, with agitation by a magnetic stirrer. Afterwards, the water washing followed: beaker was filled by DI water until overflow, the holder with glasses was raised from water, water discarded, and the holder with glass slips was replaced back. The washing cycle was repeated five times. To reduce traces of detergents, washing in HCl followed: a sufficient amount of 1 M HCl in DI water was filled into the beaker with glass slips. Cleaning proceeded at 60°C, 15 min, followed by five-times repeated water-washing as mentioned above. The HCl washing was repeated twice. Afterwards, clean glass slips are kept in the clean beaker filled by DI water.

The setup for PEM deposition was prepared. In total, nine clean glass beakers of 50 mL volume are employed in the PEM build-up process (3-times PE solution, 6-times washing buffer). Beakers are filled with 20 mL of PE solution or 30 mL of buffer. Beakers are afterwards placed on appropriate positions (as depicted in Figure 9) into a temperature-controlled water bath controlled by a feedback loop with target temperature set to 37°C. The heat transfer is enhanced by agitation by a magnetic stirrer.

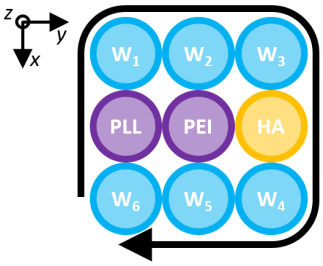

Fig. 9. A diagram of the layout of beakers (top view) with solutions of polyelectrolytes (PLL, PEI, HA) or washing buffer (W_1, W_2, ...) as employed during the preparation of PEM by the layer-by-layer approach. The dipping robot sequentially submerges the glass substrates into appropriate solutions. The curved arrow indicates sequence of a single dipping cycle, that results in the deposition of one polyelectrolyte bilayer. The cyclic repetition of the sequence leads to a step-wise deposition of polyelectrolytes on the surface until 24 bilayers are achieved. The beakers depicted by violet colour contain solution of positively charged polyelectrolytes (PEI and PLL). PEI is deposited only once as an initiator layer. The beaker depicted by yellow colour contains solution of negatively charged polyelectrolyte (HA).

A self-made dipping robot, consisting of controller OWIS L-Step 13/2 (later company LANG GmbH), 3-axis robotic arm driven by step-motors, and a PC running a control software Win-Commander 4.5, was employed for the PEM deposition (Figure 10). The dipping robot procedure comprises of PE-dips and wash-dips. One PE dip (*HA, PLL, PEI*) lasts 10 minutes with intermediate *z*-axis movement by +/-5 mm once every minute in order to improve the transport of PE molecules to the sample surface. The wash dips (W_1, ..., W_6) last for 3 min, employing simple static dip. The sequence followed by the dipping robot is: W_6 *PEI* W_1 (W_2 W_3 *HA* W_4 W_5 W_6 *PLL* W_1)*24 W_2 W_3. The time required to move the sample from one solution to the following solution is about 35 seconds. No substantial drying takes place during this time period. The glass slips are dipped into the incubation solution by the whole area at every incubation step. The total run time of the robot depositing 24 bi-layers is about 17 hours.

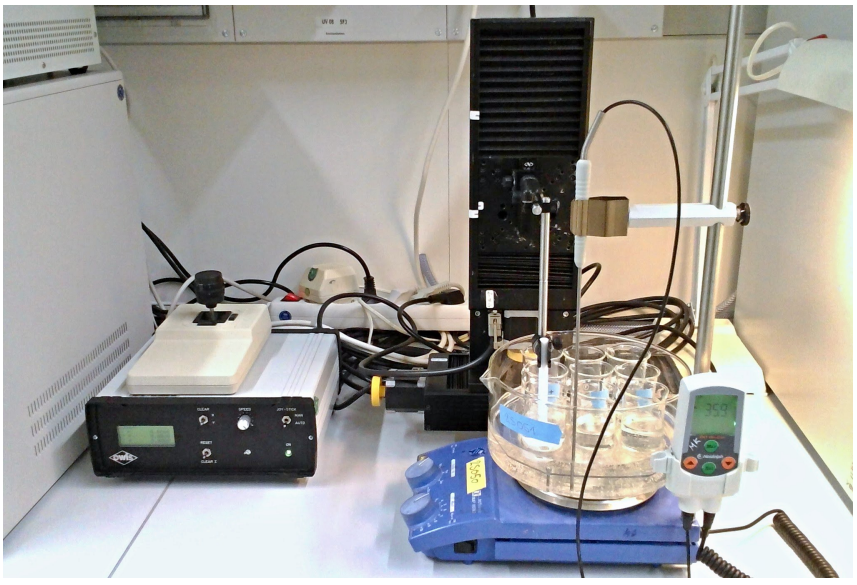

Fig. 10. A photograph of the dipping robot. On the right side, foreground, the setup of nine beakers (Figure 9) in a temperature-controlled water bath is documented. A PTFE holder of glass slips, that is dipped into a solution in the beaker at position W_6, is attached to the three-axis robotic arm of black colour placed on

the background of the right side. A control unit of the robotic arm, that serves as a PC interface, is documented on the left side of the image.

During preparation, the volume of PE solutions decreases from 20 mL to about 10–15 mL due to evaporation and solution transfer. PLL and mostly HA solution turns turbid after the PEM preparation probably due to reverse release of PE from PEM into solutions. The prepared PEM-coated glass slips are stored in the buffer at 4°C.

The presence of deposited PEM can be briefly assessed by visual observation. The PEM on glass slips displays light interference patterns when observing a reflected light by a naked eye. Typically, the prepared PEM is about 4 μm thick when freshly prepared (so-called *native PEM*), not more than 0.5 μm thick when dry, and about 2.5 ± 0.7 μm ($x \pm s$, n = 12) thick after following rehydration (so-called *plain PEM*). This topic is discussed in section 4.9.2. The thickness of the PEM is relatively uniform over most of the glass surface. Artefacts manifested by altered PEM thickness are present in the areas where the glass slip is in contact with its holder and in the area where a hanging drop of solution is trapped during the transfer of the glass slips between solutions during PEM deposition procedure (Figure 11). These areas are avoided during experiments employing microscopy imaging. The central part of the prepared PEM, accessible by the hi-NA objective of a microscope, is usually without the artefacts.

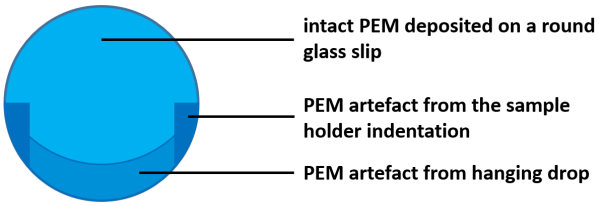

Fig. 11. A schematic diagram of a glass slip of 14 mm diameter with deposited PEM. The denoted areas of the PEM are affected by an artefact that is manifested by altered PEM thickness. This altered thickness is caused by i) the presence of a drop of solution hanging at the bottom of the glass slip during the transfer of the glass slips between solutions of the PEM deposition procedure and by ii) a pinch of the glass slip in an indentation of the holder of the glass slips. A major proportion of the PEM area is intact.

3.10 Fabrication of the incubation and the imaging chamber

For a purpose of incubation of the PEM deposited on a glass slips in various solutions, two house-made chambers were designed and fabricated out of poly(methyl methacrylate) (PMMA). Both chambers have an outer dimension of a standard microscopic slide. The incubation chamber is a single piece with three wells for incubation of up to three glass slips with solutions of volume up to 400 μL approximately (Figure 12). The other chamber—the imaging chamber—enables microscopy observation of PEM deposited on the glass slip by the objective of high NA and simultaneous incubation in a solution of volume up to 400 μL approximately (Figure 13). It comprises of two pieces: a bottom holder and a fixing rim. A small amount of silicone grease has to be applied between the glass slip and a bottom rim of the holder in order to operate this chamber in a liquid-tight manner. Both chambers have been fabricated using a milling machine Roland Modela MDX-40A.

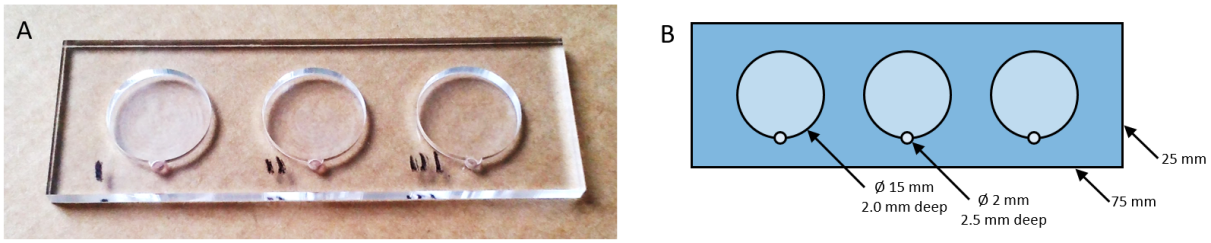

Fig. 12. A: a photograph of the incubation chamber fabricated out of PMMA sheet, 3.0 mm thick. B: a schematic diagram of the chamber with its dimensions denoted.

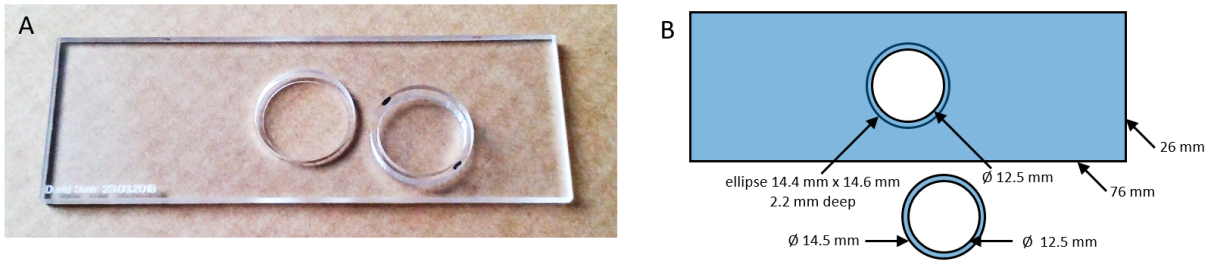

Fig. 13. A: a photograph of the imaging chamber fabricated out of PMMA sheet, 2.6 mm thick. B: a schematic diagram of the chamber with its dimensions denoted.

3.11 Fabrication of the hybrid–PEM sandwich

The procedure of hybrid deposition on the PEM surface was developed during the work presented here. Several approaches were tested and various conditions were employed until a procedure that provided satisfying results was established as a standard preparation procedure. This standard procedure is described here. For a description of other tested approaches and discussion of the corresponding results, see section 4.6.

The incubation chamber with three wells for glass slips is cleaned (mechanically by a wet tissue paper followed by sonication in 50 mM HCl), 3 glass slips with both side deposited PEM are placed into the wells and 200 μL of 0.5 mg/mL PLL solution in the buffer is dispensed into every well. After 15–30 min of incubation at RT with two to three intermediate mixing steps, the PLL solution is discarded and the glass slips in wells are five times washed by 200 μL of the buffer with agitation. Afterwards, 200 μL of cold hybrid suspension is dispensed over the PEM surface. The incubation chamber is placed into a pre-cooled dry chamber (a Petri dish filled by dry silica gel with $CoCl_2$ saturation indicator) and placed into 4°C as long as needed to fully dry out the suspension (usually about 1.5 days).

Afterwards, the glass slips may be removed from wells of the incubation chamber and the bottom side of the glass slips is cleaned from PEM by tissue paper soaked with 50 mM HCl. The prepared sandwiches (glass slips with deposited PEM and hybrids as a top layer) can be stored dry and later mounted into the imaging chamber for further experiments in a liquid environment.

3.12 Imaging of the sandwich

Most of the imaging experiments were performed with the Zeiss PALM instrument in the epifluorescence or the transmission mode. Certain imaging experiments were performed with the Zeiss LSM510 instrument in a confocal mode, transmission mode, or the differential interference contrast (DIC) mode.

The PNIPAM microgels produce an image in standard transmission microscopy even without employing any contrast-enhancing technique despite their transparent nature. This phenomenon is discussed in section 4.5. Every microgel particle acts equivalently to an optical lens probably because of its spherical shape and since the refractive index of the microgels is typically higher than the refractive index of the surrounding water-based medium. The microgels are visualized as bright objects with a dark outline when they are positioned more distant from the objective than is a position of the object plane. Oppositely, the microgels are visualized as dark objects with a bright outline when they are placed closer to the objective than the actual position of the object plane. Gas bubbles act oppositely since their refractive index is lower than the refractive index of water. When the object plane crosses the centre of the microgel particle, the image of the particle is of very low contrast and thus it practically disappears from the sight. The *z*-colocalization of the centre of a spherical particle, as determined from confocal fluorescence images, with the *z*-position of maximal reduction of the contrast of an image of the particle in transmission mode was experimentally confirmed (data not presented). Images acquired in a simple transmission mode cannot be employed for accurate size evaluation of the visualized microgels since the apparent size of microgels is somehow dependent on the relative position of the object plane and microgels. Despite that, this approach can be employed for evaluation of the distance between repeating units (e.g. a crystallized, closely packed, monolayer of PEM deposited microgels or hybrids). The curved PEM surface is visualized in transmission mode dominantly due to light refraction as well. The light interference on the hydrated PEM layer—another possible effect creating contrast in transmission mode —was assessed by an experiment indicating that the effect is insignificant or not present at all (data not presented).

The thickness of the PEM layer deposited or the sandwich can be determined by refocusing the microscopy image as well as from acquired *z*-stack image series recorded in DIC, fluorescence, or confocal mode. The *z*-position of the glass substrate surface and position of the deposited layer top surface can be visualised side-by-side by partial removal of the deposited layer in the imaged area. This can be easily achieved by scratching the deposited layer off from the glass substrate by a fine tip tool (e.g. pipette tip) since the hydrated PEM behaves as a soft gel. Nevertheless, determining a *z*-distance between various layers is complicated by a mismatch between refractive indices of the objective immersion medium and the sample medium. An oil immersion objective is usually employed here for observation of a sample in a water-based environment. In this case, the actual *z*-distance is underrated by approximately 14% since the refractive index of water is about 1.33 and of immersion oil about 1.51. This error can be afterwards corrected by recalculating the actual *z*-distance. The data presented in this work indicate the corrected value. Noteworthy, the same applies for the confocal microscopy as well.

Due to the shallow depth of field of here employed hi-NA objectives and due to the transparent nature of the imaged system, it is possible to achieve good optical sectioning in transmission mode with sufficient discrimination between images originating from various *z*-positions. The calculated *z*-resolution of here employed systems in transmission mode is about 0.5 μm. The *z*-step of the acquired transmission *z*-stacks is usually 1 μm or 2 μm.

3.12.1 Microscopy coupled with IR laser

The Zeiss PALM microscopy system enables (except others) imaging the sample in transmission or fluorescence mode and irradiate the chosen spot/area of the sample by IR laser simultaneously. The power and the focal *z*-position of the IR laser are adjustable. The system comprises Zeiss Axiovert 200M inverted microscope, PALMcombisystem module equipped with IR laser module (LaserQuantum, ventus1064, 1064 nm, maximal nominal output power 5 W, continuous wave (CW) mode), EXFO X-Cite Series 120 fluorescence lamp, 63x 1.25NA oil objective, and a colour camera Axiocam ICc1 rev4. The theoretical resolution of this setup is 115 nm/pix of the RGB Bayer mask.

The following settings were found to be optimal for the purse of the performed experiments. Bright-field transmission imaging: illumination lamp power 25%; blue chromatic correction filter; Köhler settings of the condenser (when possible; settings readjusted after every change of a liquid since the surface of liquid in a chamber has a variable meniscus shape). Fluorescence imaging: the intensity of the excitation light is highly attenuated before entering the microscope to limit the fluorophore bleaching; FITC fluorescence filter cube; acquisition of either single photomicrographs or time-lapse sequences (acquisition rate 1 image/5 s; about 3 s of excitation light illumination per one cycle). During the experiments employing the time-lapse acquisition, it is advantageous to increase the gain of the camera in a step-by-step manner, since photobleaching gradually reduces the fluorescence intensity by a few folds per minute of time-lapse acquisition (determined from time-lapse imaging of PEM loaded dextran-FITC). The focus drift influencing the time-lapse experiments was occasionally compensated by a manual discontinuous re-focusing when needed.

3.12.2 Confocal microscopy

The confocal microscopy system employed here, Zeiss LSM510meta, enables imaging of the sample in confocal and transmission mode simultaneously. The acquisition of the emission fluorescence light originating from a discrete slice of a sample (the confocal imaging) provides much better *z*-resolution when compared to the epifluorescence imaging. A transmission mode with DIC contrast, available on this setup, can be utilized as a technique complementary to the standard transmission microscopy. It visualizes differences of light path length in transparent structures of a sample such as microgels and fine surface structure of the PEM. The system comprises Zeiss Axiovert 200M inverted microscope, Zeiss LSM510meta module, feedback-controlled air-heated thermostatic chamber of the microscope and a control PC running Zeiss ZEN2009 control-software.

The following settings were found to be optimal for purpose of performed experiments: 40x/1.3NA oil immersion objective; laser line 488 nm; image acquisition in transmission and fluorescence mode simultaneously or transmission DIC mode only; Köhler settings of the condenser. *z*-stack scanning parameters: pixel dwell time: 2.06 μs/pixel, distance between slices: ~ 0.5 μm, optical slice thickness: ~ 2 μm (FWHM), image *xy* resolution: 776 pixel × 776 pixel (the optimal resolution). *z*-stack time-lapse scanning parameters: 5 slices per one stack, distance between slices: 1 μm, optical slice thickness: ~ 2 μm (FWHM), repetition rate of the time-lapse: 15 s, pixel dwell time: 1.03 μs/pixel.

Chosen experiments were performed at elevated temperature. For that purpose, the microscopy chamber was heated up using an air heating system with feedback control. The usual set-temperature was 45–50°C. Nevertheless, the air temperature determined by the feedback sensor significantly differs from the temperature of the sample plausibly due to a thermal bridge between the sample and the objective/nosepiece of the microscope that is a major heat sink. Therefore, the temperature changes of the sample are delayed behind the air temperature changes as well. The sample was covered by a small transparent lid during the time-lapse acquisition at increased temperature to limit the evaporation of liquid from the microscopy chamber. Moreover, the temperature inside the microscopy chamber may spontaneously rise up to ~28°C within several hours of the microscope operation at RT conditions due to heat produced by the instrument.

Under thermally stable conditions, the focus drift is minimal. When the system is out of the thermal equilibria—mostly during the experiments performed at the increased temperature—the rate of drifting rises up to units of micrometers per minute. Small metal weights placed on the sample stage were employed to compensate for the focus drift during time-lapse image acquisitions. Moreover, the acquisition of images in a *z*-stack mode enables visualization of the studied coating (PEM or sandwich) in at least some images of the acquired *z*-stack.

For evaluation of the fluorescence intensity, the acquired *z*-stacks were first overlaid along *z*-axis keeping the maximum pixel value from the stacked images. Afterwards, a region of 100 pixel × 100 pixel was chosen and average fluorescence intensity in this region can be plotted against time as a time development of the fluorescence intensity.

3.13 Spectroscopy analysis

The process of shrinking and swelling of hybrids is followed by a variations in light scattering intensity and by red-shifting of the LSPR band of the surface-attached AuNRs (section 2.2.2). Hence, spectroscopy was employed to corroborate the thermoresponsivity of the hybrids attached to the PEM surface. A temperature-controlled spectrophotometer Agilent 8453 / Agilent 8909OA was employed for the measurements. A spectroscopy cuvette (Sarstedt, macro, 1 cm light path, polystyrene, applicable for wavelengths greater than 350 nm) served as a container of the liquid medium of the sample and as a heat mediator as well. The sample—14 mm glass slip with various surface deposited layers—fits diagonally into the cuvette in a tight way enabling no free space for the sample to move. The position of

the glass slip in the cuvette is carefully adjusted so the light passes only through the central area of the slip.

Baseline measurements: The purpose of the baseline measurement is to determine the absorbance arising from components of the setup different than the sample. The measurement is repeated before every thermal cycle measurement to ensure comparability between the acquired spectra. Measurement performed at RT. The sequence of the measurement: blank on empty spectroscopy cell, measure empty cell, measure empty cuvette, measure cuvette with 3 mL of DI water, measure cuvette with 3 mL of DI water with stir bar and clean glass slip inserted.

Thermal cycle measurement: The measurement of the absorption spectra of the sample at different temperatures. The sequence of the measurements: starting at RT, the instrument is blanked on the last baseline measurement. A sample composed of the glass slip with one side deposited sandwich, 3 mL of DI water and a stir bar is inserted into the spectroscopy cell. The thermal cycle measurement is set up with the temperature of the sample stepwise following this order: 10–15–20–25–30–35–40–45–50–45–40–35–30–25–20–15–10°C. Dwell time after achieving the target temperature on the spectroscopy cell was 4 minutes. Practically, the temperature of the sample at the moment of measurement is delayed by about 0.5–1.0 °C behind the nominal temperature of the cell. Importantly, the DI water is degassed by keeping it under vacuum and only shortly before measurement used for the sample preparation, otherwise the gas dissolved in the water exudes itself in a form of bubbles on the walls of cuvette at the elevated temperature. At the low temperatures, the air humidity may condensate on the outer walls of the cuvette. Therefore a low humidity environment is required for the thermal cycle measurements.

3.14 Loading experiment

This type of experiment aims at the observation of kinetics and equilibria of spontaneous loading of a chosen molecule from the surrounding medium (loading medium) into the sandwich. FITC labelled dextran of 4 kDa molecular mass was chosen as the molecule of interest (section 4.9). Both Zeiss PALM and Zeiss LSM instruments were employed for the loading experiments. Various settings of the loading experiment were tested and gradually improved. The procedure described here is found to be the most appropriate to the aim of the experiment and the equipment employed.

First, the sandwich deposited on a glass slip is mounted into the imaging chamber; 150 μL of the buffer is dispensed over the sandwich; a scratch in the sandwich is introduced by a scratching of the sandwich by a pipette tip in a single stroke; the chamber with the sample is covered by a transparent polymer lid with two holes for inserting a tubing for liquid dispensation and removal by a hand-operated syringe (Figure 14). The sandwich is let to re-hydrate for a few minutes. Meanwhile, the imaging chamber with the sample is mounted into the microscope stage. A representative area of the sample, including the scratch and a confluent microgel region, is chosen. The time-lapse image acquisition is triggered; 50 μL of 0.5 mg/mL dextran-FITC solution is dispensed into the 150 μL of buffer already present in the incubation chamber from the syringe. The solution in the chamber is five times mixed by repeated aspiration and

exspiration of about 50 μL volume of the incubation solution (~ 5 seconds in total). Afterwards, the loading solution is let to stand over the sandwich while acquiring the time-lapse fluorescence photomicrographs documenting the fluorescence intensity in the PEM.

Several measurements failed due to insufficiently mixed loading solution. The data originating from these measurements were excluded from further evaluation. Several experiments were performed at a controlled temperature of about 45°C. Therefore, the whole chamber of the microscope was heated up using an air heating system with feedback. Nevertheless, the temperature of the sample is substantially delayed behind the temperature of the air even after several hours of equilibration. Therefore, the actual temperature of the sample is known only approximately.

3.15 Release experiment

This type of experiment is focused on the assessment of the release kinetics of the molecule of interest from the PEM of a sandwich preloaded by the molecule of interest. Dextran-FITC of 4 kDa molecular mass was found to be the optimal molecule of interest (section 4.9). Zeiss PALM instrument is employed for this type of experiments. Various settings of the release experiment were tested and gradually improved. An optimal setting corresponding to the aim of the experiment and the equipment employed is described here.

The sandwich is first pre-loaded with dextran-FITC: the glass slip with the top-side deposited sandwich is mounted into the imaging chamber and the loading solution (dextran-FITC of 4 kDa molecular mass, 0.125 mg/mL solution in buffer) is dispensed evenly over its surface. A scratch in the sandwich is introduced by a single stroke of a pipette tip over the surface; the chamber with the sample is covered by a transparent polymer lid with two holes for inserting a tubing; two tubes with 1 mL syringes attached to their other ends are lead through the lid into the sample chamber (Figure 14). The dead volume of every tube is about 100 μL. The sandwich is let to incubate with the loading solution for 2h at RT until it is washed away during the first stage of the release experiment.

Experimental procedure: The incubation chamber with the sample and loading solution is mounted into the stage of the microscope. A representative area of choice—including the scratch and a confluent microgel region—is imaged in the transmission mode and in the fluorescence mode. The *active-phase of the release experiment* follows. The time-lapse acquisition of fluorescence photomicrographs is triggered and the chamber is step-by-step 5-times washed by 200 μL of fresh buffer (lasting about 50 s in total) using one syringe filled with buffer and the second empty syringe for aspiration of wash solution. Afterwards, the *passive phase of the release experiment* follows. The buffer is let to stand in the chamber while the time-lapse acquisition of the photomicrographs continues. An area of choice of the sandwich can be irradiated by the IR laser (1064 nm, CW; adjustable parameters: intensity, focus, switching on/off) during the release experiment. The irradiation is possible at transmission and fluorescence mode as well. Nevertheless, the laser intensity may slightly vary due to different optical elements involved in different imaging modes.

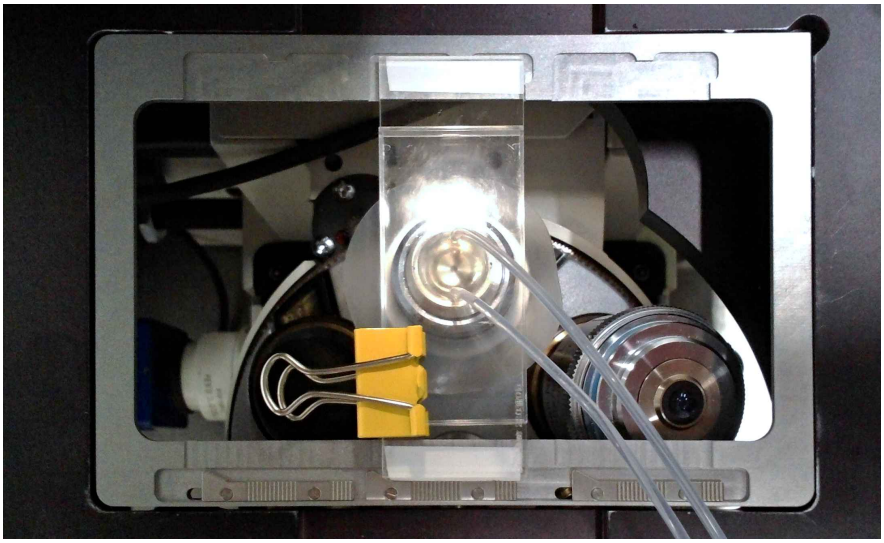

Fig. 14. A photograph of the experimental setup employed for liquid handling during the release experiment. The PMMA imaging chamber with a glass slip that bears a deposited sandwich is inserted in the metal table of a microscope. A transparent cover lid that reduces evaporation from the chamber is attached to the body of the chamber by the yellow binder clip. Two Teflon tubes, that lead through holes in the cover lid into the chamber, serve for dispensing and aspirating of the medium. The other end of each tube is connected to a 1 mL syringe for manual solution handling (not in the image).

4. Results and discussion

4.1 Evaluation of a single-fractional FRAP data

A sample composed of a single type of microparticles that are characterised by a single diffusion coefficient was utilized for validation of the evaluation procedure of the FRAP data. The sample consists of a stable aqueous suspension of fluorescent latex microparticles of 0.116 μm or 0.042 μm diameter. According to the Stokes–Einstein equation, these particles diffuse with diffusion coefficient of 4.2 $\mu m^2/s$ or 12 $\mu m^2/s$, respectively (at 25 °C). Samples of several dilutions were prepared (1, 2, 4, 8 dilution factor) to assess the influence of interactions between particles (i.e. restricted diffusion) and a range of particle concentration applicable for the measurement. The data obtained were evaluated by the A-approach, as well as by the S-approach. Data presented in this section are based on thirty images recorded during fifteen seconds of the recovery process.

4.1.1 The A-approach

Assumptions of this evaluation procedure about the data to be evaluated are straightforward. However, the results of the analysis become easily misleading when data do not fulfill some of these assumptions (e.g. well-defined shape of bleached profile, instantaneous bleaching, single-fractional diffusion). As it was described in section 3.6, a complete evaluation requires three separate fitting steps.

First, FRAP profiles are fitted by Gaussians and the corresponding diffusion coefficient D can be directly evaluated as described by equation 1 and equation 2 (section 3.6). The fitting procedure is usually able to identify a correct fit of the Gaussians on a first run. Occasionally, the fitting procedure fails at later time points of the recovery process when the depth of a fluorescence dip becomes smaller than the noise level or the diffusion spreads the dip substantially beyond the ROI. Nevertheless, already a few correctly fitted FRAP profiles are usually sufficient for the accurate determination of D.

Second, the parameter t_o is varied in an iterative way until the relation, characterised by equation 3 (section 3.6), becomes linear. The dimensionality of diffusion d is thereby obtained. This relation is fairly susceptible to irregularities introduced by the data acquired, that are influenced by the instability of the offset or of the sensitivity of the detector and other variables. At later time points of recovery, the values optimized become often unstable. Therefore, only early stages of recovery with a uniform trend are suitable for the optimization of t_o. Even a careful choice of the time interval included into the optimization of t_o does not necessarily result in a robust value of dimensionality of diffusion d.

Third, the acquired data of temporal development of the depth of the dip $A(t)$ are fitted by the relation described in equation 4 (section 3.6). Parameters D and d of equation 4 are transferred from the preceding steps of the evaluation, while parameters t_o, K and M are free for fitting. The amount of immobile fraction in the sample can be thereby obtained. Results of this evaluation are fairly susceptible

to irregularities introduced by the acquired data as well. Moreover, space of fitted parameters does not necessarily present only one well-defined minima of SQD but may contain several minima in case of noisy input data or poorly shaped recovery profiles. The fitting procedure may thereby identify a solution of the local minima of SQD, which does not represent reality. Robustness of the evaluated amount of immobile fraction is thus substantially dependent on the quality of input data.

Results of the fitting, summarized in Table 1, are based on optimal but real experimental conditions, thus representing the best practically achievable outcome. From the table it can be concluded that results of the A-approach match the anticipated values and trends. The obtained values of *D* of the microparticles match the anticipated values of 4.2 or 12 $\mu m^2/s$ for 0.116 and 0.042 μm sized particles, respectively. Further, the values of *D* do not vary with the dilution factor. It indicates that interactions between particles, as well as the overall intensity of the fluorescence signal acquired, do not interfere with the evaluated *D* within the dilution range employed. Next, the evaluated dimensionality of diffusion *d* is close to unity in all cases. It confirms that the setting of the experiment (employing a low-NA objective and bleaching of a prolonged rectangular area) practically reduces the dimensionality of the diffusion observed from a restricted 3D space to 1D. Next, the evaluated amount of the immobile fraction is negligible or zero for all samples. This result fulfills our expectations for pure single-fractional diffusion. Further results indicate that the amount of bleached fluorophores *M* increases with increasing dilution factor. We have not found a satisfactory explanation for this observation until now. Our measurements indicate, that this observation cannot be fully explained by depletion of excitation photons due to absorption in the sample neither by scattering of the excitation light by latex particles. Finally, the SQD obtained after Gaussian fitting increases with an increase of the dilution factor. This correlation is caused by the reduction of the fluorescence signal with increasing dilution factor while the noise of the data recorded remains unchanged.

Table 1. Results of evaluation of data from FRAP experiment with a single diffusive fraction by the A-approach using 0.116 or 0.042 μm sized particles.

particle diameter (μm)	0.116				0.042			
particle dilution factor	1	2	4	8	1	2	4	8
D ($\mu m^2/s$) [a]	4.7 ± 0.4	4.6 ± 0.3	5.0 ± 0.3	4.8 ± 0.8	14.5 ± 0.4	14.8 ± 0.7	15.4 ± 0.8	15.3 ± 0.7
d [b]	0.90 ± 0.09	0.87 ± 0.07	1.07 ± 0.26	0.80 ± 0.25	0.99 ± 0.07	0.99 ± 0.03	0.93 ± 0.04	0.93 ± 0.09
amount of immobile fraction (%)	1 ± 2	1 ± 2	2 ± 3	5 ± 4	0 ± 0	0 ± 0	0 ± 0	0 ± 0
M (μm^d) [c]	2.7 ± 0.2	3.4 ± 0.1	4.6 ± 0.5	4.7 ± 0.2	3.5 ± 0.3	4.2 ± 0.3	4.4 ± 0.5	6.0 ± 0.3
SQD [d]	0.34 ± 0.03	0.43 ± 0.01	1.07 ± 0.12	2.51 ± 0.23	0.20 ± 0.04	0.35 ± 0.02	0.81 ± 0.08	2.29 ± 0.11

[a] *D* was evaluated from initial 2.5 seconds of recovery.
[b] *d* was evaluated from the initial 5 seconds of recovery.
[c] *M* quantifies the fluorescence dip produced during pattern bleaching.
[d] SQD correspond to the difference between all 30 measured FRAP profiles and their respective Gaussian fits.
Displayed numbers represent mean value ± standard deviation (based on triplicates).

4.1.2 The S-approach

The S-approach allows us to evaluate multi-fractional diffusion without any precedent information about the number of fractions. Both single-fractional and multi-fractional diffusion can be assessed. In contrast to the A-approach, no particular shape of the recovery profile is required—FRAP profiles are evaluated as they are. The S-approach evaluates a whole set of data from FRAP experiment at once, unlike the analytical solution where evaluation proceeds in a step-wise manner. This freedom makes data evaluation more potent but it also requires more careful assessment of uncertainty of the results.

Results of the evaluation by the S-approach are documented in Figure 15 and are also summarized in Table 2. Diffusion coefficients obtained by the S-approach are in good agreement with expected values. According to the Stokes–Einstein equation, the expected diffusion coefficients for the 0.116 and 0.042 μm sized microparticles used are 4.2 and 12 $\mu m^2/s$, respectively. The results are also in line with results obtained by the analysis of the identical data by the A-approach (Table 1). This proves the ability of the S-approach to provide accurate results.

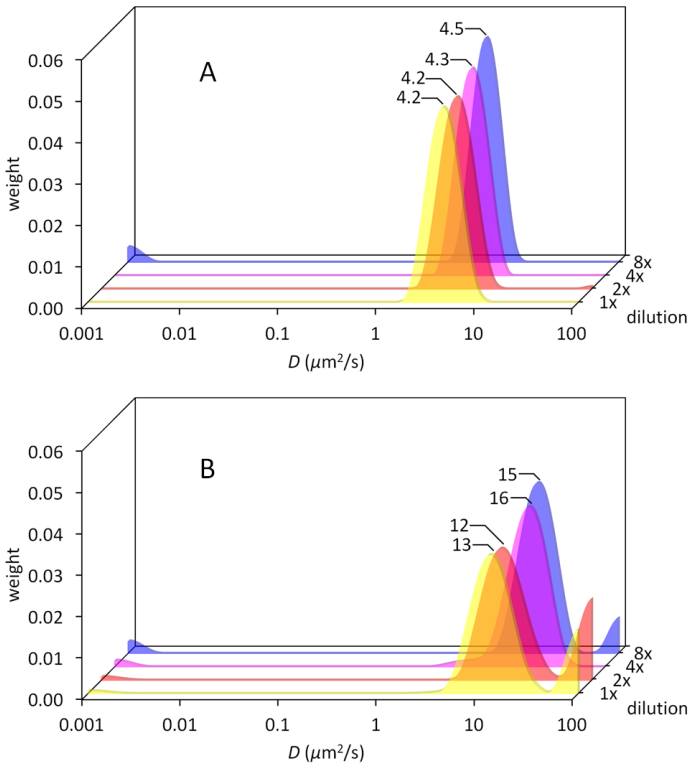

Fig. 15. Distribution of diffusion coefficients obtained by the S-approach for 0.116 (A) and 0.042 μm (B) sized particles, respectively. The distributions presented are averaged distributions form triplicate measurements. Values denoted at peaks are diffusion coefficients at peak maxima. Regularization parameter λ = 10.

Table 2. Results of evaluation of data from FRAP experiments with a single diffusive fraction by the S-approach using 0.116 or 0.042 μm sized particles.

particle diameter (μm)	0.116				0.042			
particle dilution factor	1	2	4	8	1	2	4	8
D (μm²/s) [a]	4.2 ± 0.1	4.2 ± 0.1	4.3 ± 0.1	4.5 ± 0.1	13 ± 2	12 ± 2	16 ± 2	15 ± 1
SQD [b]	0.12 ± 0.01	0.07 ± 0.02	0.30 ± 0.20	0.36 ± 0.07	0.07 ± 0.01	0.13 ± 0.05	0.21 ± 0.07	0.35 ± 0.09

[a] D was evaluated as peak maximum of the distribution of diffusion coefficients resulting from S-approach analysis.
[b] SQD corresponds to the difference between all 29 FRAP profiles and their corresponding fits found by the S-approach.
Displayed numbers represent mean value ± standard deviation (based on triplicates).

The regularization parameter λ was set to 10 for all evaluations. This value was chosen just high enough to keep evaluated distributions of the diffusion coefficient presented in this section in a form of a single compact peak. An optimal value of λ depends on the *signal to noise ratio* (S/N) of the input data and on the amount of input data. The S/N ratio is related to the quality of the input data and it usually falls into the interval from 30 to 50 in experiments presented in Figure 15. (S/N was calculated as the ratio between the depth of the dip of the first post-bleach profile and the standard deviation of the noise of the FRAP profile.) The amount of input data is practically an amount of well-shaped FRAP profiles. Various experiments will differ in both parameters but variations within experiments presented here are not significant. A value λ equal to 10 is a good approximation for most of the cases presented here and keeping this value fixed simplifies comparison between different experimental results. More results on the use of the regularization can be found in section 4.3.

4.2 Evaluation of a two-fractional FRAP data by the S-approach

A sample consisting of two components of different diffusivity was used to test the ability of the S-approach to resolve two differently diffusive particle fractions. The slow diffusing component was a stable suspension of FITC-conjugated latex microparticles (0.2 μm in diameter) and the fast diffusing component was hydrolysed FITC. The FITC conjugated particles and hydrolysed FITC were exploited for this experiment to ensure comparable fluorophore behaviour of both components. A ratio between these two components within the sample was varied. Data presented in this section are based on sixty images recorded during sixty seconds of the recovery process.

The results presented in Figure 16 demonstrate the ability of the evaluation procedure to resolve two diffusive fractions within one sample and to identify the diffusion coefficients of the fractions. D of 0.2 μm sized microparticles is approximately 2.2 μm²/s according to DLS measurements, and D of fluorescein (or hydrolysed FITC respectively) is given to be approximately 420 μm²/s (Culbertson, Jacobson, and Ramsey 2002).

The results of the evaluation by the S-approach are displayed in Figure 16. The D values of FITC decrease from 437 to 209 μm²/s with increasing FITC concentrations from particle:FITC ratios of 4:12 to 0:16. Fluorescein is known to form dimers at higher concentrations, which would alter its diffusion rate. Nevertheless, just about 0.025% of fluorescein should be present in dimeric form at its highest

concentration (25 μM) used in our experiments (dimerization constant of fluorescein dianion is about 5 M^{-1}) (Arbeloa 1981; Speiser and Chisena 1988). The actual amount of dimers may differ because of a shift of the dimerization constant caused by differences in ionic strength, pH and because the behaviour of FITC may differ from fluorescein. This dimerization phenomenon could partially explain the observed down-shift of *D* of FITC but probably additional effects are involved.

D of FITC fractions at high particle:FITC ratios (over 12:4) readily drop to values of approximately 100 $\mu m^2/s$. Surprisingly, the peak of this fraction is present even in case, when no FITC was added (a '16:0' ratio of Figure 16). The origin of the fraction corresponding to this peak is not clearly known. Nevertheless results indicate that this peak may correspond to FITC residuals being still present after the coupling reaction or to fluorophore attached to some molecular fragments released from the particle surface after the coupling reaction.

D of latex particles remains at a value of approximately 1.7 $\mu m^2/s$ for most mixing ratios. It agrees well with the value 2.2 $\mu m^2/s$, which corresponds to *D* determined by DLS. The position of this peak starts to shift to lower values, when the fluorescence signal of this fraction becomes significantly weaker as the mixing ratio drops. This shift may be caused by an artifact of the data evaluation originating from the assumption that the bleaching procedure is much faster than the observed diffusion and the first post-bleach FRAP profile is recorded immediately after bleaching. Because this assumption is not completely fulfilled, the first post-bleach profile is not the actual starting point of diffusion for all fractions as recovery through diffusion of particles is already underway at this stage. As the recovery process takes place, the fast fractions recover swiftly. On the contrary, the slow fractions still form a well-defined dip in the FRAP profile. However, in comparison to the first post-bleach profile, the dip appears narrower than expected since mostly the fast fraction caused broadening of FRAP profile in the first post-bleach image. Consequentially, the diffusion rate of the slow fraction is underestimated, when the fast fraction dominates.

A sample consisting of pure hydrolysed FITC (a '0:16' ratio of Figure 16) shows only a single peak as it is expected but its position is somehow down-shifted (partially explainable by dimerization of fluorescein as described above).

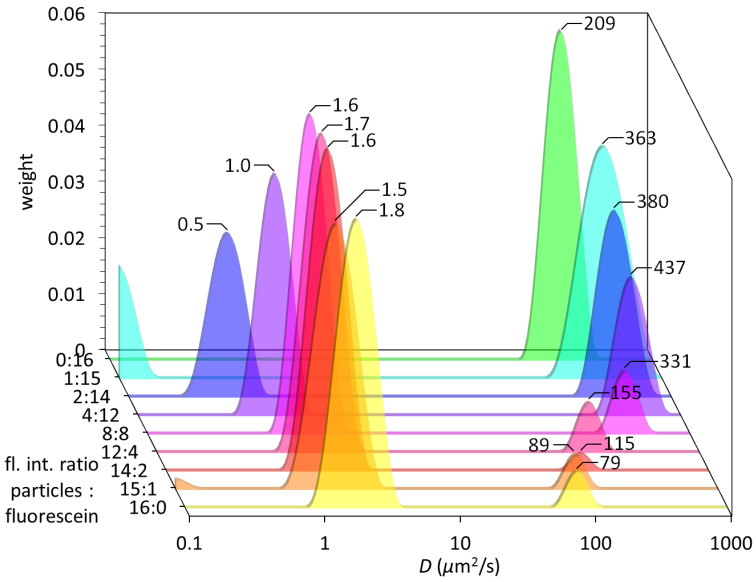

Fig. 16. Distribution of diffusion coefficients of samples with two diffusive fractions (0.2 μm sized particles and FITC) obtained by the evaluation of FRAP experiments using the S-approach. The fractions were mixed at defined ratios corresponding to their fluorescence intensity (the depth axis). Values denoted at peaks are diffusion coefficients at peak maxima. The diffusion coefficient of particles is 2.2 μm²/s as determined by DLS measurement and the diffusion coefficient of hydrolysed FITC is given to be approximately 420 μm²/s (Culbertson, Jacobson, and Ramsey 2002). Regularization parameter λ = 10.

The distributions presented in Figure 16 are of a peak width of a quarter decade of D approximately. It can serve as an indication of resolving power of the S-approach applied to this particular set of data with the regularization parameter λ set to be 10. Because the regularization procedure generally tends to merge overlapping peaks, the distance between two peaks should be at least about half a decade of D (~ three fold difference) in order to be resolved. The S/N ratio of input data of Figure 16 usually falls into an interval between 40 and 110.

A mixture of monomeric and dimeric FITC molecules, as well as a mixture of latex particles (0.1 and 0.5 μm in diameter), have been assessed for multi-fractional analysis by S-approach as well. Unfortunately, it was not possible to resolve two distinct fractions in either case. This may be explained by an insufficient S/N ratio of the input data.

4.3 Regularization and limitations of the S-approach

The S-approach uses a regularization of possible solutions during the optimization phase to balance the amount of information on the output to the amount and quality of information on the input. The better the quality and the larger the quantity of the input data, the weaker the regularization may be applied and thus the higher the resolving power becomes. We have observed that the quality of our data was mostly hampered by noise of the detector (photomultiplier tube used in the CLSM setup). Better S/N ratios could be possibly obtained with better detectors. The quality of input data for multi-fractional analysis was negatively influenced also by deviations from the assumption of instantaneous bleaching. The influence if this issue can be reduced by the combination of installing a high power laser module

and employing a fluorophore prone to bleaching in order to reduce the bleaching time. To avoid this problem at all, the bleaching process could be integrated as a part of a simulation-based evaluation. We have decided not to include a simulation of the bleaching process into our S-approach because it would require the introduction of additional parameters describing the bleaching process to be optimized or knowing them in advance (Song et al. 1996; 1995).

The slower the observed components diffuse, the more FRAP profiles can be recorded. When a fast recovery is observed (such as that of hydrolysed FITC) it may take only several seconds until a bleached pattern disappears in the noise. Here, we use a scanning rate of two images per second or one image per second. Higher scanning rates would not improve the results any further, because it would lead to a significant increase of noise of FRAP profiles recorded with our CLSM setup.

The program (NBJ-FRAP-1) presented in this work employs the Tikhonov–Phillips method of regularization. This regularization method penalizes solutions with higher values of the second derivatives of the distribution of diffusion coefficients. Strength of the regularization may be varied by adjusting the parameter λ. When the strength of regularization is chosen too weak, the evaluation procedure may generate a distribution that consists of several closely-positioned diffusive fractions instead of the actual single diffusive fraction—the peak decomposition takes place. When a higher strength of regularization is chosen, peaks in the distribution tend to become broader and smoother. When two peaks are close enough, they tend to merge into a single peak—the decomposed peaks merge.

One of important aspects of simulation-optimization methods is the computational burden. The weight of the burden is ruled by the chosen parameters of simulation and optimization. The simulation procedure of a usual simulation-based evaluation presented in this study spans minutes up to tens of minutes with a standard up-to-date PC. The subsequent optimization procedure (NNLS algorithm) usually requires just minutes in order to find a solution.

Some critical factors inherent to the FRAP technique itself are listed with regard to the S-approach: low signal-to-noise ratio, the duration of the bleaching is comparable to the duration of recovery, the non-linear correlation between fluorophore concentration and fluorescence intensity, fluorescence recovery through chemical reactions or any other recovery mechanisms different from the spontaneous diffusion, photoactivated side-reactions, competition between diffusion and binding reaction, local heating of the sample caused by scanning or the bleaching procedure and more. These factors may be present to a certain extent in most of the FRAP experiments. However, their influence should be minimized to keep the data evaluations valid or they should be included into the evaluation process.

4.4 Multi-fractional analysis of CytC diffusion in HA/PLL PEM

The final step of this work deals with the evaluation of multi-fractional diffusion of a biomacromolecule (protein) loaded into a polyelectrolyte multilayer. FITC labelled CytC and PEI(HA/PLL)$_{23}$HA have been

chosen as a model protein and a well-studied biologically relevant multilayer, respectively. The multilayer is a few micrometers thick. Figure 17 represents the evolution of the distribution of diffusion coefficients of CytC loaded into the multilayer as a function of time elapsed after loading. During storage in the buffer, the fast diffusing fractions of CytC diminish after some time and the slow diffusing fractions start to dominate. These results are in a good agreement with previous findings (Velk et al. 2016) demonstrating that a distribution of diffusive fractions of the protein lysozyme loaded into a similar HA/PLL multilayer changes in a comparable manner. This phenomenon may be explained by gradually increasing extent of interactions between protein molecules or between protein and polymer(s) during the time course of storage. The observed change is rather slow probably due to multiple cooperative interactions in the multilayers.

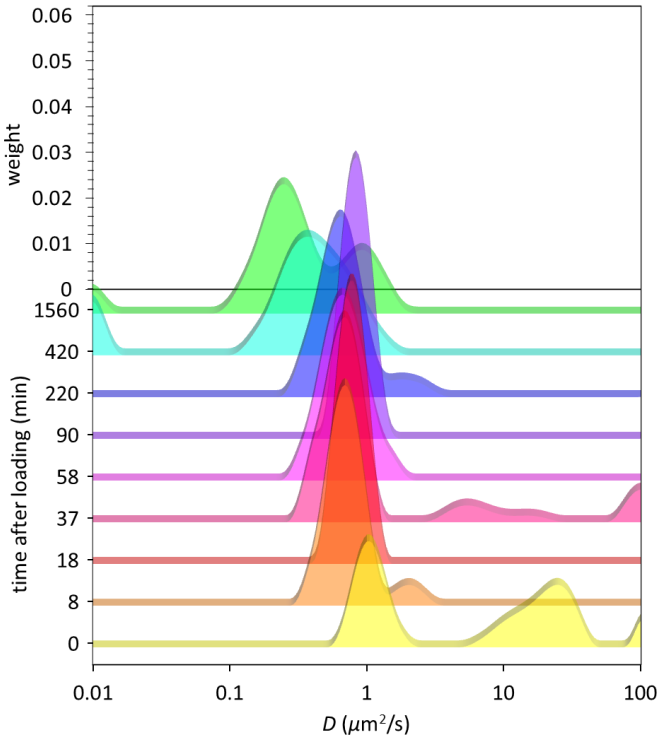

Fig. 17. Distribution of diffusion coefficients of CytC loaded into $(HA/PLL)_{24}$ PEM as a function of time after loading has started (t = 0 min).

We believe that the approach developed will enable a deeper understanding of diffusion in multilayers and its effect on the properties of the multilayer (Xu et al. 2013; Jourdainne et al. 2008; Nazaran et al. 2007; Picart et al. 2002; Lavalle et al. 2004). This is a key to assemble biologically active multilayers with adjusted composition and tailor-made properties as a platform to guide cellular behaviour (Aggarwal et al. 2014; Zhao et al. 2016; Muzzio et al. 2016; 2017).

4.5 Characterisation of PNIPAM microgels bearing Au nanorods

The following chapters of the section *Results and discussion* present the second part of the work that deals with fabrication of the light-addressable drug release system. The concepts and components of this system were introduced in section 2.2.

To estimate properties of the employed hybrids (PNIPAM microgels surface modified with AuNRs) and possibilities of their observation, the hybrids were imaged at various sample conditions and imaging settings. First, the stock suspension of hybrids was observed as a drop sitting on a clean glass slip by means of transmission light microscopy. The single hybrid particles in suspension are identifiable, nevertheless producing rather limited image contrast. Moreover, the random walk of the hybrids in their environment does not allow the acquisition of sharp photomicrographs. Hybrids are dominantly present as single particles in suspension with the tendency to accumulate on the suspension–air interface (as discussed in this section below).

Second, the drop of the suspension was let to dry up on plain glass in an open atmosphere. The processes following the drying of plain PNIPAM microgels on a hard surface are already documented and discussed in literature (Wei et al. 2013; Horigome and Suzuki 2012). The photomicrographs of the dry remnant obtained after drying of the hybrid suspension are presented in Figure 18.

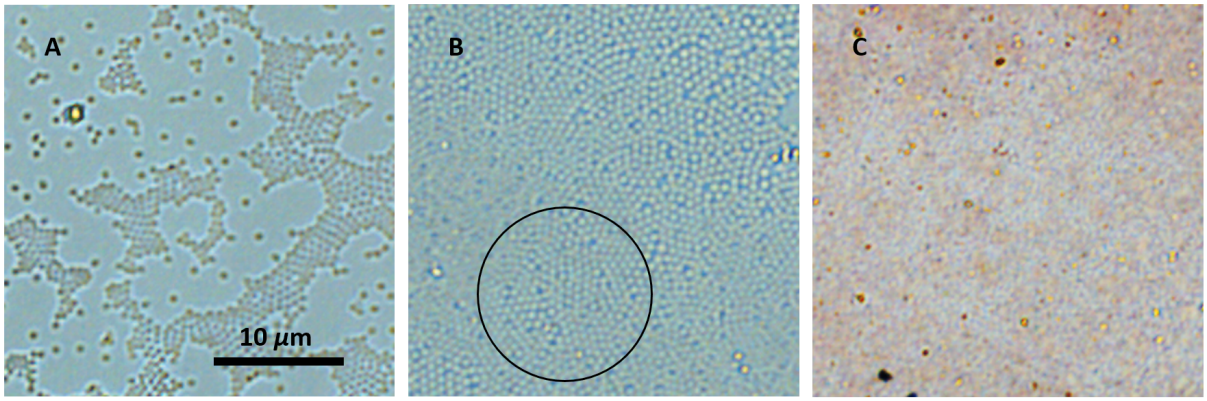

Fig. 18. Colour transmission photomicrographs of a remnant left after drying a drop of the hybrid suspension (10 μL) on a plain glass surface. The three micrographs presented correspond to different positions of the dry remnant: A: an outer edge of the dry remnant; B: approximate halfway between the outer edge and the centre of the remnant; C: centre of the remnant. Images were acquired at RT. The black circle of the image B denotes an area of prominent periodic order of hybrids.

The hybrids are identifiable in the images A and B as round objects of an approximate diameter of 0.5 μm. The hybrids are visualized as dark objects with a bright outline in the image A and as bright objects with a dark outline in the image B. The image C depicts a multilayer of hybrids, where single hybrids are not distinguishable. The hybrids are of red hue that is pronounced in areas where multilayers of hybrids have formed (image C). The size of dry hybrids is rather uniform. The images document a gradient of the number of deposited hybrids per area rising from the outer edge of the dry remnant (image A) to the centre of it (image C). Separate hybrids, as well as small islands of densely assembled hybrids, are

documented in image A. Periodically ordered assemblies of hybrids in a monolayer are documented in image B (for example the region denoted by the black circle). A multilayer of hybrids is documented in image C.

Figure 18 documents that the **hybrids are observable by means of transmission microscopy** in a dry state. Hybrids are visualized as dark objects with a bright outline when positioned closer to the objective than is the position of the object plane (image A) or bright objects with a dark outline when positioned more distant (image B). When the object plane coincide with the centre of hybrids, the hybrids appear sharp but of poor contrast. It renders the hybrids indistinguishable from their background. This observation can be possibly explained by light refraction and light scattering on the hybrid particles due to their higher refractive index in comparison to the surrounding environment and approximately spherical shape (section 2.2.2). In aqueous solution, this phenomenon is less pronounced probably due to the smaller difference in refractive indices of the hybrid particle and the solution. Importantly, the transmission photomicrographs of the microgels/hybrids can not serve for the evaluation of their absolute size, since the apparent particle size in the acquired images is dependent on the distance between hybrid and the object plane. The **reddish hue of hybrids** is caused by the presence of AuNRs, while the plain PNIPAM microgels are colourless (Figure 5). Noteworthy, there are no salt crystals present in the dry remnant that indicates that the amount of dissolved salts (and therefore ionic strength) in the suspension was rather low.

The image A and mostly the image B (e.g. the area denoted by the black circle) depicts areas of deposited monolayers of **periodically ordered** hybrids with rather short-range quasi-hexagonal order that resembles a crystalline structure. Formation of such two-dimensional arrays upon drying of PNIPAM microgels was described in the literature for the first time already in 1986 (Pelton and Chibante 1986) but not further studied for many years afterwards. The interest in these structures started to rise in 2005 (Tsuji and Kawaguchi 2005b; 2005a). These areas of periodically ordered hybrids are employed here for a relatively accurate evaluation of the average particle-to-particle distance between hybrids (*the lattice constant*) that is characteristic for the sample. The periodic order is a feature typical for **close packing of particles** that are assumed to be one of the prerequisites of effective control over the molecular transport through the gating layer of the hybrids deposited. Nevertheless, the presence of the periodic order is necessary but not sufficient condition of the close packing. Several phenomena may lead to short-range periodic order of surface-deposited hybrids without any close packing. Ordered layers of surface-deposited microgels with spacing between particles dependent on their charge are well described in the literature (Zavgorodnya and Serpe 2011; Schmidt et al. 2010; Schmidt, Hellweg, and von Klitzing 2008; Uhlig et al. 2016). Further, closely packed (and thereby periodically ordered) hybrids attached to a surface may eventually shrink, that results in a state of conserved periodic order but not close packing. Control over this mechanism—the steering of the interparticle void by controlling the swelling state of the particles deposited on the surface—is the core idea of the work presented here.

The assessment of **the packing density of deposited hybrid monolayers** by a simple visual inspection of a transmission photomicrograph cannot be accurate due to the following reasons. First, the visualized size of a hybrid particle is accurate only when the object plane crosses the centre of the

hybrid. Nevertheless, hybrids do not produce any contrasting image in that situation as was discussed in the paragraph above. Second, the shape of hybrids may deform after surface-attachment of the hybrids. A 'pancake'-like shape (Zavgorodnya and Serpe 2011) or 'sombrero'-like shape (Horecha et al. 2010) of microgels after their attachment to the hard surface are documented in the literature. The transmission images produced by the hybrid particle of the same size but the different shapes may substantially differ. Hence, the visual inspection of transmission photomicrographs may serve only as a guide for assessing particle size and packing density.

Finally, the packing density of the deposited hybrid monolayers can be assessed by considering the lattice constant in comparison to the **actual size of a particle**. Matching values of the lattice constant and the particle size under the conditions given indicate close packing. The evaluated lattice constant is not influenced by the position of the object plane, unlike the observed size of a particle. Nevertheless, the assessment of the packing density is complicated by the uncertainty of the actual particle size used as a reference. The size of a hybrid particle is assumed to vary with changes of its environment (e.g. ionic strength, pH), molecular interactions (e.g. interaction with PLL: section 4.9.1), due to physical deformation after attachment, or due to thermally-triggered swelling/shrinking. Therefore, the reference value of the particle size should originate directly from the actual sample in order to limit the influence of these variables.

The hydrodynamic radius of particles obtained by the DLS measurements cannot serve as a good reference value of the hybrid particle size for several reasons. First, the hydrodynamic radius of only unmodified microgels is available since the suspension of modified hybrids is not compatible with the requirements for the DLS measurement. Furthermore, modification of a P(NIPAM-AAA) microgel particle by gold nanorods plausibly leads to a local change of polymer hydration and reduction of particle size. The inequality of the microgel hydrodynamic diameter and hybrid particle size of the particles employed here is discussed in section 4.8.2. Second, the PNIPAM microgels are reported to have a gradient of cross-linking density decreasing from their core to the surface (Wu et al. 1994) leading to a kind of 'hairy' outer surface and thereby somehow to a fuzzy definition of the microgel size. Third, the microgels or hybrids may plausibly deform, collapse, or stretch upon surface deposition (as is discussed above in this section) in the process of particle packing.

The actual particle size can be estimated from the particle-to-particle distance determined inside a compact and stable multilayer deposit of particles or inside particle clusters. The direct physical contact between particles in such multilayers or clusters ensures that the lattice constant evaluated and the particle size are equivalent. The value of particle size estimated on the basis of particle-to-particle distance may serve as a reference value for subsequent evaluation of the packing density of other sample areas or other samples under carefully assessed equivalent conditions (figures 21, 23, 24, 27). Finally, by aggregating all relevant values obtained at various experimental conditions (sections 4.6–4.10) on the basis of this evaluation, it can be estimated that the actual particle size in the deposit accounts to about 0.9 μm at the swollen state (figures 19, 21, 23, 24, 25, 26, 27, 29) and about 0.6 μm at the shrunken state (figures 18, 23, 24, 25). Close adherence of the hybrid diameter to either of these values indicates that these two values correspond to the fully swollen and fully shrunken state of a hybrid particle,

respectively. The comparison of these values with the hydrodynamic radius of unmodified microgels is discussed in section 4.8.2.

The smallest resolvable lattice constant of the sample depicted in Figure 18, image B is about 0.60 μm (evaluated as the average distance between 24 closely positioned resolvable hybrid particles in the periodically ordered zones of the image B). The information about the actual size of the hybrids in this sample is not available. Since the photomicrographs of Figure 18 are acquired after the spontaneous dry-up of the sample in an open atmosphere of ambient humidity, the hybrids documented are probably shrunken to a certain extent. Being aware of limitations, the comparison between the lattice constant obtained and the hydrodynamic diameter of shrunken microgels determined by DLS (~ 0.5 μm, Figure 5) indicates, that the periodically ordered hybrids are closely packed or at least close to this state.

Another interesting phenomenon is documented by image A of Figure 18. Separately deposited hybrids, as well hybrids packed in areas of the periodic order, are present simultaneously next to each other. This observation indicates that there is a competition between hybrid-hybrid interaction, wetting forces, and maybe hybrid-surface interaction during the dry-up of the suspension. This discussion is further developed in section 4.6.1.

Hybrids were observed to spontaneously **adsorb on the suspension–air interface** and form there a periodically ordered interface monolayer. This phenomenon is described in the literature for PNIPAM microgels on the water–air interface (Geisel, Richtering, and Isa 2014; Horigome and Suzuki 2012; Minato et al. 2018). The process of surface adsorption is probably driven by minimization of the surface tension. The presence of this phenomenon for hybrids and microgels alike indicates that the surface wettability of the hybrids does not differ substantially from the surface wettability of the plain PNIPAM microgels. It is difficult to acquire an image of the hybrids adsorbed on the suspension-air interface in a satisfactory quality. Nevertheless, the interface monolayer was successfully transferred onto the underlying plain glass surface by carefully dragging the sitting suspension drop over the plain glass surface. A similar approach, that employs the Langmuir trough, is described as a possible way for the preparation of deposited closely packed microgel layers in literature (Geisel, Richtering, and Isa 2014).

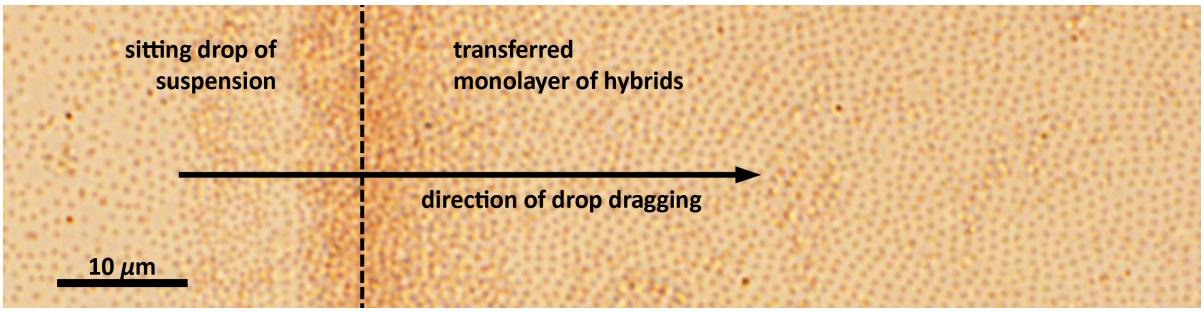

Fig. 19. Colour transmission photomicrograph of a layer of deposited hybrids obtained by transferring a monolayer of hybrids, spontaneously formed on the suspension–air interface, onto the plain glass surface. The left side of the image corresponds to the position where the drop of the hybrid suspension was initially sitting. From this position, the drop was dragged in the direction of the arrow while the interface layer of periodically ordered hybrids was transferred onto the glass surface and attached there. Image acquisition followed immediately after the transfer. Image was acquired at RT.

The result obtained by dragging a suspension drop over a plain glass surface is depicted in Figure 19. The left part of the image corresponds to the position where the drop of the hybrid suspension was initially sitting. The drop was dragged from this position in the direction of the arrow denoted. Thereby, the periodically ordered interface layer was transferred onto the glass surface and attached there. Between the area where the suspension drop was initially sitting and the transferred monolayer is a zone of increased layer thickness arising from partial drying of the sitting suspension drop. Microgels attach on the glass surface in the area of the sitting drop as well, nevertheless, rather in a disordered manner. By transferring the suspension–air interface monolayer onto the glass surface, a periodically ordered monolayer of hybrids was deposited. The lattice constant determined in the periodically ordered region is about 0.88 μm (based on the average distance between 51 closely positioned particles). It can not be conclusively determined whether the deposited monolayer is formed by closely packed or only periodically ordered hybrids, since no reference value of the actual particle size is available. Moreover, the processes of transferring the hybrids may be of complex nature and influencing the actual size of particles.

Noteworthy, the PEM surface is more hydrophilic than the glass surface and therefore it behaves rather like a water phase not enabling adherence of the hybrid particles. Therefore, transferring the periodically ordered interface layer of hybrids onto a glass surface is not an applicable approach for the deposition of hybrids on PEM. A different approach needs to be employed for this purpose.

4.6 Preparation of the sandwich

One of the cornerstones of this work is a successful attachment of hybrids on the PEM surface, which results in a layered sandwich structure. The sandwich should be sturdy enough to withstand the shear forces arising from liquid handling as well as the force arising from irradiation by IR laser at conditions similar to the laser tweezers. It is speculated, that the best performance of the hybrid deposit as a steerable gate can be achieved when the deposit consists of a few layers of closely packed hybrid particles. Aside this optimal case, hybrids may theoretically attach to the PEM as a thick multilayer, a monolayer, or not confluently at all. A multilayer deposit, that is too thick, would probably prevent an anticipated molecular transport through the solution–sandwich interface irrespective of the swollen/shrunken state of hybrids. On the other hand, a monolayer or even an incomplete layer of hybrid deposited may result in leaking of the gate towards molecular transport at a rate, that masks the intended gating effect.

A method of hybrid attachment on the PEM surface had to be developed for the purpose of this application. Up-to-date literature describes several methods of microgels attachment onto a hard surface employing drying (Tsuji and Kawaguchi 2005b; 2005a; Horecha et al. 2010; Uhlig et al. 2016; Wei et al. 2013; Schmidt et al. 2010), long term sedimentation (Weng et al. 2016), centrifugation (South et al. 2009), dip-coating (Zhang et al. 2005; Schmidt, Hellweg, and von Klitzing 2008), transfer using a Langmuir trough (Geisel, Richtering, and Isa 2014), or spin-coating (Burmistrova and von Klitzing 2010;

Schmidt et al. 2008; Jaber et al. 2011). The attachment of charged PNIPAM-copolymer microgels onto a PEM surface is sparingly documented in the literature (Serpe, Jones, and Lyon 2003; Zavgorodnya and Serpe 2011). The attachment of PNIPAM microgels or even their hybrids to the HA/PLL PEM surface is not well described until now. The surface deposition methods documented in the literature focus predominantly on hard surfaces. Here, the hybrids need to be attached on a soft and hydrophilic surface of the HA/PLL PEM. Hence, the applicability of the methods documented in the literature for the task presented here is limited. General concepts of these methods may be plausibly applicable after some optimization for deposition on the HA/PLL surface. Results achieved by employing common incubation, drying, sedimentation, and centrifugation are described in the following paragraphs of this section.

The AuNPs are known to strongly attach to the HA/PLL PEM surface. This interaction is supposedly arising from positive interaction between AuNPs and the PLL. Since the PLL can freely diffuse within the PEM, it migrates to the PEM surface and it is described to form surface-attached PLL-AuNPs complexes (D. Volodkin et al. 2010). The ability of PLL to diffuse in PEM, as well as the ability to load into the PEM in amounts overcompensating the negative charge of the HA resulting in overall positive charge of the PEM, are well documented (Picart et al. 2002). This mechanism is the basis of the exponential growth-mode of the HA/PLL PEM. Therefore, it can be reasonably anticipated, that one of the possible mechanisms leading to the attachment of the hybrids to the PEM surface is the attractive interaction between PLL–AuNRs. In order to enhance this attachment, the PEM to be modified is saturated with PLL shortly before attachment. The PEM is incubated with 0.5 mg/mL buffered solution of PLL for about 15 minutes while sporadically agitating. The incubation is finished by 5 steps of water washing with agitation. The PLL-rich PEMs obtained are assumed to enhance the attachment of hybrids onto the PEM surface. This assumption is supported by the results obtained during preparations of sandwiches under various settings and mostly during preparations based on a wet process (sedimentation and centrifugation). This practise was therefore adopted as a part of a standard procedure of sandwich preparation.

4.6.1 Incubation of hybrids with PEM followed by drying and rehydration

The most straightforward approach for hybrid attachment on the PEM surface is a common incubation of the PEM with the suspension of hybrids (Vikulina et al. 2015). This approach was tested as a first choice. The HA/PLL PEM was incubated with 200 μL of hybrid suspension at no-flow conditions at RT and in an open atmosphere. The temporal development of the system was followed by means of transmission microscopy.

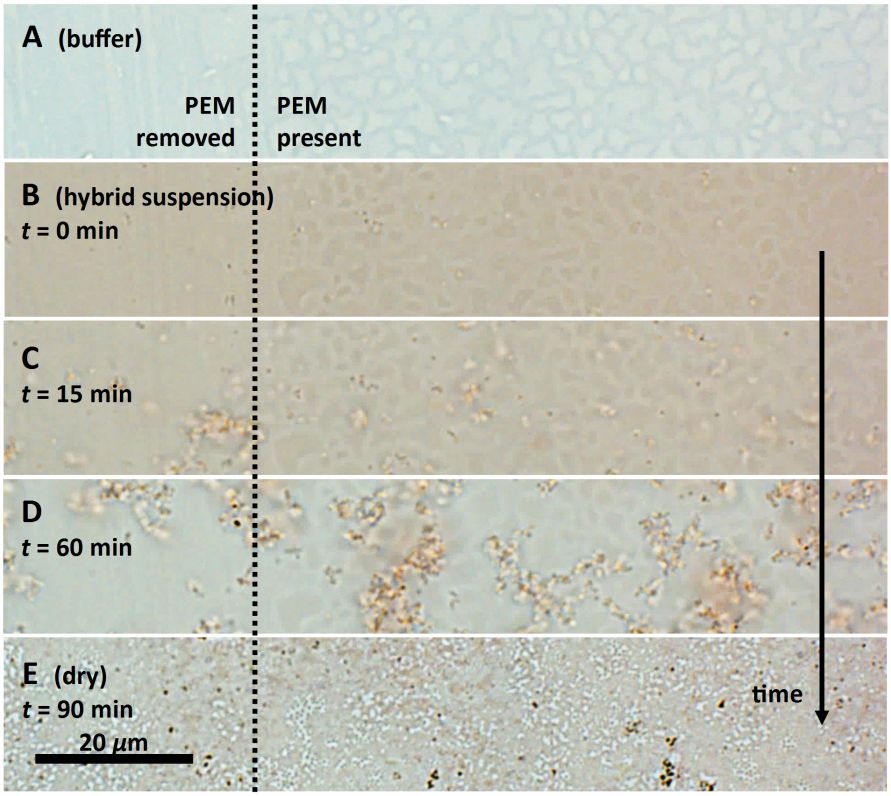

Fig. 20. Time-lapse of colour transmission photomicrographs depicting incubation and concomitant spontaneous drying of the hybrid suspension on the PEM surface. Image A: PEM in buffer environment; image B: buffer exchanged for 200 µL of microgel suspension and a starting point of spontaneous development; image C: the system after 15 min of spontaneous development; image D: the system after 60 min of spontaneous development; image E: the system after 90 min of spontaneous development—the suspension dried up. The left side of every image presents the region of the sample with mechanically removed PEM (the scratched region). The right side of every image presents the area of the sample with deposited PEM. Images were acquired at RT. The acquisition of the time-lapse was influenced by a slight focus drift.

The image A of Figure 20 depicts the onset state of the PEM before the application of the hybrid suspension. The left part of the micrograph depicts the area of deliberately removed PEM, that serves as a control zone. It documents the presence of scraps of the PEM. The right part of the micrographs, that corresponds to the native PEM, documents its island structure. The time sequence of Figure 20 captures two simultaneous processes. First, hybrids spontaneously form clusters in the suspension of RT, which gradually sediment. Second, the volume of suspension reduces due to evaporation until it completely dries up (image E). Drying of the suspension is accompanied by a gradual deepening of the meniscus shape of the suspension, which leads to an increase in overall brightness of the acquired micrographs.

Importantly, Figure 20 documents that the **PEM can be visualized** in the hydrated state by means of transmission microscopy without employing a contrast-enhancing technique. Experiments not presented indicate, that the visualization of the PEM is dominantly caused by light refraction on the curved surface of the PEM. The light interference on a PEM layer has a rather insignificant influence on image formation if any at all (data not presented). Further, the visualized island structure pattern of the native PEM deposit is a phenomenon common to a thin HA/PLL PEM (Picart et al. 2001). As is described in the literature, the islands gradually coalesce into a confluent layer as the PEM becomes higher during

its build-up. The island structure appearing here is an undesired phenomenon, that arises from poor control of some parameter of PEM preparation procedure—possibly a concentration of HA or PLL in the dipping solution due to the transfer of the polyelectrolytes between solutions leading to the formation of HA/PLL complexes in the dipping solution and thereby stripping the free polyelectrolytes from their solution.

The gradual **formation of hybrid clusters in suspension**, as depicted in Figure 20, is probably a consequence of an increase of hybrid suspension temperature during image acquisition and thereby reducing the suspension colloidal stability. The hybrid suspension at 4°C was observed to be rather colloidally stable while at RT the stability is somehow reduced. When the suspension of clusters is cooled down from RT to 4°C, the clusters have a tendency to fall apart again. This is plausibly a consequence of the surface modification of the negatively charged microgels by the positively charged CTAB-stabilised AuNRs, eliminating the overall charge of hybrids. On the one hand, this feature makes the applicability of the suspension at room temperature troublesome. On the other hand, this process indicates, that the hybrids do not repel each other. The capability of hybrids to reside close to each other is probably one of the key factors of the successful preparation of closely packed hybrid deposits. Otherwise, the charged microgels are known to repel each other even when bound to surface and thereby the microgels assemble on the surface at a particle-to-particle distance mainly determined by the particle charge (Zavgorodnya and Serpe 2011; Schmidt et al. 2010; Schmidt, Hellweg, and von Klitzing 2008; Uhlig et al. 2016).

From Figure 20, several reasons, why a simple **incubation of the PEM with the hybrid suspension cannot lead to the formation of a sandwich,** can be concluded. First, there is no dominant force, that would bring the hybrids from their suspension to the PEM surface. The hybrids could be possibly brought to the surface by sedimentation or centrifugation as is described in section 4.6.3. Second, hybrids in suspension at room temperature have a tendency to aggregate and gradually form clusters. These clusters sediment in a range of minutes. Nevertheless the clusters contact the PEM surface only at a few spots, while most of the hybrids do not reach the surface (documented in Figure 22, left side). Third, brief contact between PEM and hybrids, that arises from Brownian motion or forced flow of the suspension (e.g. pipette-mixing), does not lead to attachment of hybrids onto the surface. As can be concluded from incubations performed with various procedures, the hybrids or its clusters need to be kept in contact with the PEM surface for longer time periods (range of minutes or more) in order to firmly attach. As is discussed in this section below and in section 4.6, it is anticipated, that the attachment arises from an attractive interaction between hybrids and PLL, that is available from the PEM. This process is assumed to depend on the availability of PLL on the surface of the PLL-rich PEM. Moreover, stable attachment plausibly requires some time to establish.

The PEM covered by the cluster containing suspension was afterwards allowed to **dry up in an open atmosphere**. Preparation of packed 2D arrays of PNIPAM microgels on a hard surface by drying the microgel suspension and the processes following the drying are discussed in the literature (Tsuji and Kawaguchi 2005b; 2005a; Horecha et al. 2010; Horigome and Suzuki 2012). The system investigated here differs from those documented in the literature since the PEM surface is soft and highly hydrated while

the surfaces documented in the literature are rather hard. Nevertheless, the drying approach proved to be applicable for the preparation of the system being developed here as well. After a complete dry-up of the hybrid suspension on the PEM surface, the resulting deposit was rehydrated by dispensing of 200 μL of buffer over the dry sample. The rehydration is usually complete within a minute after the buffer administration, as can be inferred from transmission microscopy observation (data not presented). After **the sandwich is rehydrated**, no further substantial changes are observable in a range of hours. The rehydrated sandwich obtained was imaged by means of photomicrography in transmission mode.

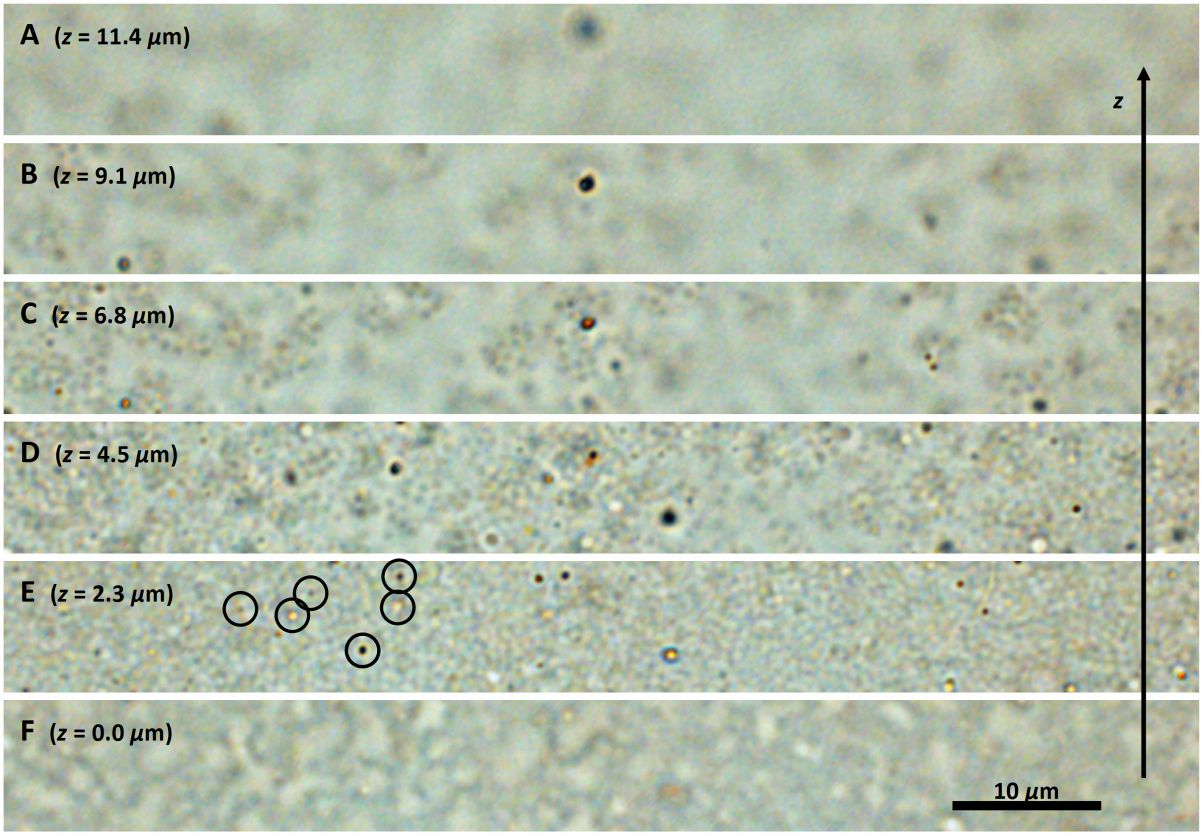

Fig. 21. z-stack of colour transmission photomicrographs documenting the hybrid deposit fabricated by drying the hybrid suspension and rehydrating by the buffer. Image A corresponds to a z-position in the solution just above the deposit. Image F visualizes the PEM layer. Images B-E document the hybrid deposit. z-distance between subsequent images is 2.27 μm. The black circles of image E denote some of the presented 'spherical inclusions'. The accumulated z-distance is denoted in the captions of the images. Images are acquired at RT. The images document a different area of the sample displayed in Figure 20.

The result of rehydration is documented in Figure 21 as a z-stack of photomicrographs acquired in transmission mode. Image F depicts the island structure of the PEM. On top of the PEM are deposited hybrids (images C, D, E). The multilayer hybrid deposit withstands shear forces arising from solution mixing during the solution exchange without any major decomposition. It indicates that the hybrids are attached to the PEM surface as well as to each other which results in a stable confluent multilayer deposit. The average distance between two closely positioned swollen hybrids in the deposit is about 1.0 μm (an equivalent of the lattice constant, evaluated on 16 closely-positioned hybrids at upper levels of the multilayer deposit). This particle-to-particle distance is equivalent to the particle size since it is

evaluated on directly-attached hybrids. Finally, transparent objects, with a size of approximately 0.5–1.5 μm, trapped inside the hybrid deposit but appearing substantially different from hybrids, are distinguishable in the microphotographs. Some of them are denoted by black circles appearing in image E. Similarly as other particle-like objects of refractive index higher than that of its environment, the objects appear bright or dark depending on their relative position to the object plane (section 4.5). Therefore, it can be concluded that these objects are of approximately spherical shape, as it is corroborated by the z-stack confocal images acquired in separate experiments (data not presented). These objects are hereinafter referred to as the *spherical inclusions*.

The **spherical inclusions** in the hybrid deposit (documented by figures 21, 45, 46) plausibly arise during the process of drying. Only the state before and after the formation of the inclusions was observed. These inclusions are plausibly formed of the PEM material that separates from the compact PEM layer and leaves a locally thinner PEM layer behind (data not presented). This process can be explained by elevated ionic strength during the drying process, rendering the PEM softer or even fluid. This explanation accords with the process of PEM softening during suspension drying suggested in the following paragraphs.

The hybrid layer is rather **compact and confluent** in comparison to the precursor hybrid clusters present before drying. However, the thickness of the layer varies with position. In some areas, only a monolayer of hybrids was deposited while on other areas the deposited multilayer is up to 10 μm thick. The position of the regions presenting the thicker deposit spatially correlates with the position of the hybrid clusters presented before drying. This indicates that the hybrid clusters presented in suspension were brought to the PEM surface while being partially reformatted during the drying process as is schematically depicted in Figure 22.

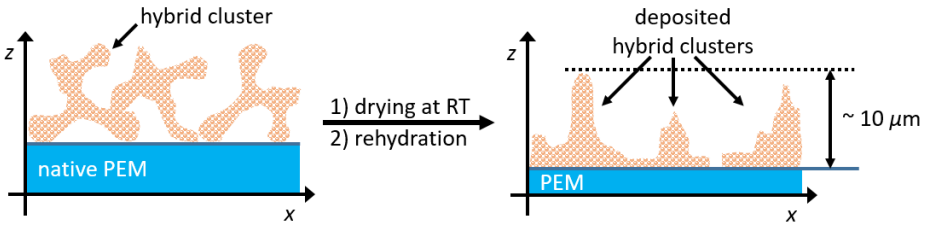

Fig. 22. Schematic diagram (cross-section) of the PEM covered by hybrid suspension representing the sedimented hybrid clusters before the drying–rehydration procedure at RT (left image) and after the procedure (right image).

The process of cluster re-formation and the attachment of hybrids to the PEM surface during drying is possibly explained on the basis of **capillary forces** pressing the microgels towards the surface (Wei et al. 2013). Simultaneously, increasing ionic strength during drying of the suspension results in a **screening of electrostatic interactions** and thereby weakening of the bonds forming the clusters and PEM. The increasing ionic strength plausibly increases the mobility of PLL in PEM. This is of importance since **PLL is anticipated to act as a glue for the sandwich** (section 4.6). The simultaneous pressing of hybrids towards the softened PEM surface and the weakening of already existing bonds probably lead to

gradual interconnection of the sandwich components on a molecular scale and formation of hybrid-PEM attachment. Noteworthy, this process happens despite a relatively low salt concentration in the suspension before drying as the PEM is several times washed by water before administration of the water suspension of hybrids. A closer observation of the processes shortly before dry-up and during rehydration could shed more light on this phenomenon.

The **reduction of height of the deposited hybrid layer** by removing the upper layers while keeping the basal layer (the layer directly attached to PEM) intact would enhance the quality of the system. Such attempts are reported as successful in literature (Schmidt et al. 2008; 2010) and a similar approach was tested here. The sandwich with the deposited hybrid multilayer (prepared by the drying method) was incubated in diH_2O at RT or at 4°C for about half an hour, followed by active agitation of the water, and finally sonication in a water bath at RT or at 4°C for several seconds. Neither of the approaches resulted in a substantial reduction of deposit thickness or change of its structure (data not presented). Nevertheless, this result documents an endurance of the hybrid–PEM attachment as well as the hybrid–hybrid attachment. It corroborates the hypothesis, that the stability of the deposit does not arise exclusively from the forces forming the hybrid clusters at RT (section 4.5), but it is stabilised by another effect as well—probably the interaction with PLL discussed in this chapter.

4.6.2 Sedimentation of hybrids followed by drying and rehydration

The attempt documented here to deposit hybrids on the PEM surface is based on sedimentation of hybrids without the need to remove the aqueous phase. It is anticipated, that sedimentation of single hybrids from their suspension may result in a more uniform deposit in comparison to the deposit achieved by drying of hybrid clusters. Therefore, the suspension should be cooled in order to prevent the hybrids from forming clusters. It is known from visual observations of the hybrid suspension, that sedimentation of the single hybrids proceeds on a scale of days while the hybrid clusters sediment substantially faster. A native PEM was therefore incubated with 200 μL of the hybrid suspension at 4°C in a wet chamber (protecting the suspension from drying) overnight. The beginning and the end of the incubation process are depicted in Figure 23.

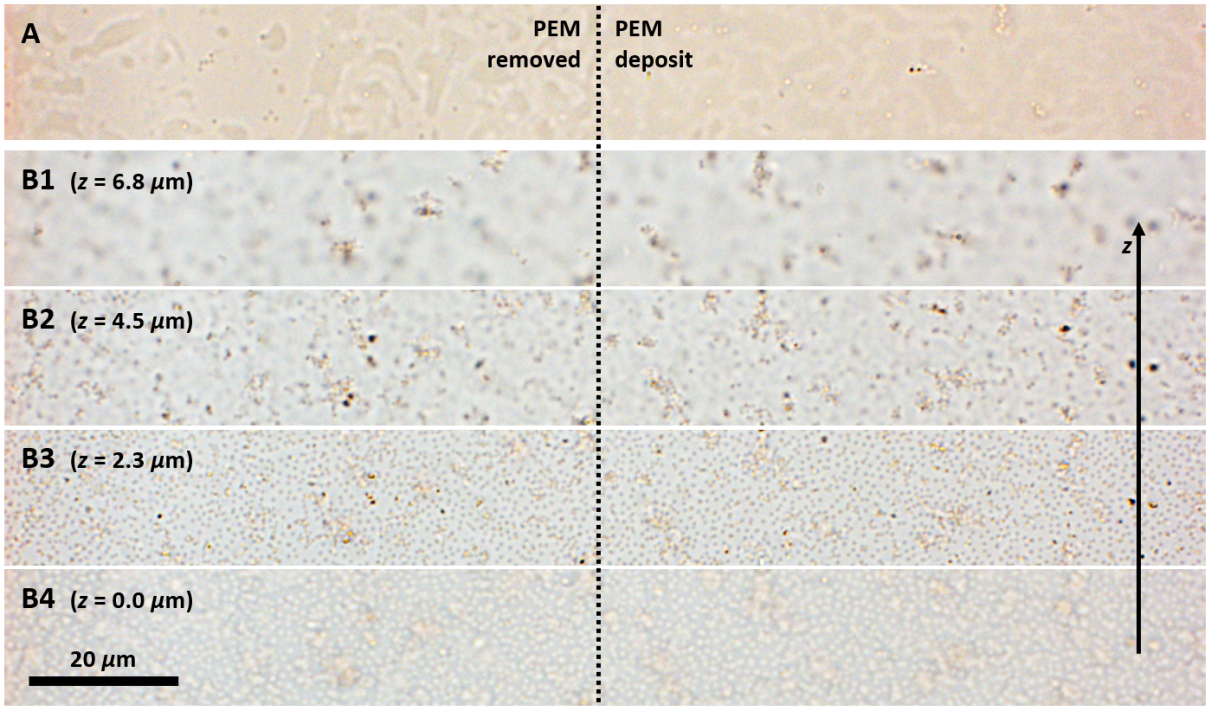

Fig. 23. Colour transmission photomicrographs depicting a hybrid suspension dispensed on the HA/PLL PEM before (image A) and after (image B) sedimentation overnight at 4°C. Image B presents a z-stack of photomicrographs depicting the state after the sedimentation. The image B4 corresponds to the z-position of the PEM while the image B1 corresponds to a z-position in the suspension. The hybrid deposit is displayed in between. The z-step between subsequent images is 2.27 μm. The accumulated z-distance is denoted in the captions of the images. Images A and B correspond to different locations of the same sample. The reference region where the PEM is deliberately removed (the scratched region), is present on the left side of the images. The images were acquired at RT.

Image A, representing the state at the beginning of incubation, documents sporadically distributed hybrids in the vicinity of the PEM surface and on the glass surface where the PEM has been removed by scratching. Various z-positions of hybrids on the surface are manifested by different brightness of hybrids as visualised by transmission microscopy. A few hybrid dimers, that are identifiable in the suspension, served for evaluation of the particle-to-particle distance accounting to 0.86 μm (evaluated as the average distance between 12 hybrid pairs in suspension; only some of the pairs are presented in the image displayed). This particle-to-particle distance is equivalent to the particle size since it was evaluated on the hybrids directly attached to each other (section 4.5). Image B, representing the state after overnight incubation at 4°C, documents the PEM surface covered by single hybrids and small clusters. The hybrids attached to the PEM surface are predominantly random-distributed. There is nearly no area of the deposit that exhibit a periodic order. The particle-to-particle distance, evaluated from the PEM-attached hybrid clusters, accounts to 0.63 μm (evaluated as the average distance between 13 hybrid particles present in the clusters attached to the PEM and placed at a z-distance of about 2 μm above the basal deposit layer). This particle-to-particle distance is equivalent to the particle size since it was evaluated on directly attached hybrids. Nevertheless, the average particle-to-particle distance of the deposit is substantially greater due to the dominant random distribution of the hybrids on the surface. The hybrids deposited on the PEM surface as well as in the area of removed PEM (the scratched region) are attached firmly enough to withstand shear forces generated by solution mixing and forces

accompanying irradiation by IR laser (Fig. 35). The suspension is still rich in hybrids, that are predominantly in a state of discrete particles or sparse small clusters, after overnight incubation (not documented by the microphotographs presented in Figure 23).

Most of the hybrids remained discrete during overnight incubation indicating that cooling to **4°C prevents cluster formation.** However, a few smaller clusters formed during the period of incubation. A plausible explanation for their formation is based on the notion of an **interaction between hybrids and PLL released from the PEM** into the suspension, since PLL is assumed to play a dominant role in hybrid attachment (section 4.6). This explanation is supported by two phenomena presented. First, the size of hybrids reduces during overnight incubation as it can be inferred from a comparison between particle size before incubation (0.86 μm) and after incubation (0.63 μm). Second, the thermoresponsive properties of hybrids were reduced after overnight incubation as is discussed in section 4.7.2. Both phenomena are also observed when hybrid suspension is directly mixed with a PLL solution, that leads to PLL penetration into the microgels (section 4.9.1). This indicates that the aforementioned phenomena are caused by the PLL present in the suspension. Such free PLL penetrates microgels leading to their non-thermal shrinking and promotes cluster formation. The praxis of saturating the PEM with PLL shortly before preparation of the deposit could thereby enhance the undesired PLL-triggered shrinking of hybrids.

Particle-to-particle distance of hybrids in the basal layer of the deposit substantially exceeds the actual particle size (0.63 μm). The possibility of close packing of hybrids is thereby excluded. This conclusion is supported by the absence of periodic order of hybrids in the deposit. A prolonged period of sedimentation may possibly lead to an increase of density of hybrids in the deposit. Nevertheless, achieving the close packing would probably require a considerably longer time—if achievable at all—due to progressive occupation of the available free surface during sedimentation and **the need to reorganize the hybrids** already attached to the surface with a random distribution. This reorganization might be propelled by capillary forces and ionic strength increase when methods based on drying of the suspension are employed (section 4.6.1). Such a driving force for reorganisation is probably missing when a sedimentation-based method is employed.

A substantial amount of hybrids was concentrated nearby the PEM surface during the sedimentation, but not attached to the surface. The deposition of all available hybrids uniformly over the PEM surface would plausibly create a very high deposit layer. The same total amount of hybrids is used for the drying-based method of the hybrid deposition. Nevertheless, formation of a **convex meniscus on the hybrid suspension** during drying causes that most of the hybrids dispensed deposit on the outer rim of the sample while a relatively thin deposit layer is formed in the centre of the sample (section 4.6.4). Hence, it can be anticipated that wet methods of hybrid deposition have potential of a better resource economy of hybrid suspension in comparison to the drying-based methods.

Finally, the sandwich obtained after overnight incubation, still overlaid by hybrid suspension, was let to dry up in an open atmosphere with the help of a fan shortly after acquiring the photomicrographs presented in Figure 23. Afterwards, the sandwich obtained was rehydrated with the buffer. The sandwich in dry state, as well as in the following rehydrated state, was imaged by means of photomicrography in

transmission mode. The acquired photomicrographs are presented in Figure 24.

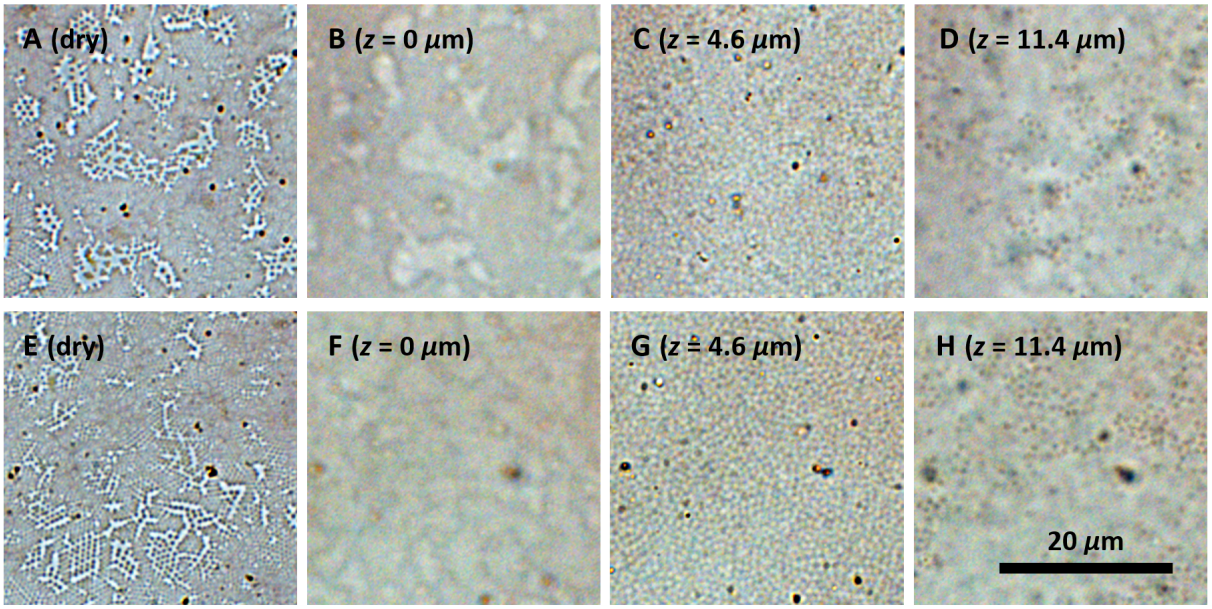

Fig. 24. The hybrid deposit obtained after drying the suspension in an open atmosphere. The top row of images (A–D) corresponds to the region of deliberately removed PEM with sparse PEM scraps on the glass surface. The bottom row of images (E–H) corresponds to the region of deposited PEM with the native island structure. The images in columns originate from the same photomicrograph. The first column (A, E) corresponds to the dry state after a complete dry-up of suspension. Other images correspond to the state after rehydration and washing with cold buffer. Images in the second column (B, F) visualize the PEM. Images in the third column (C, G) visualize the basal layer of the deposit. Images in the fourth column (D, H) correspond to layer about 6.8 μm above the basal layer. The accumulated z-distance is denoted in the captions of the images. All images were acquired as colour transmission photomicrographs of identical acquisition settings at RT.

One of the phenomena documented in Figure 24 is the simultaneous spatial correlation of several aspects: the lattice constant of the periodically ordered deposit in the dry state (image A and E), apparent size of the deposited hybrids in the dry state (image A and E), apparent interparticle space in the dry state (image A and E), and curvature of the underlying surface (image B and F). In detail, images B and F, acquired in the rehydrated state, document topography of the PEM since the curved PEM surface act as a convex lens bending the passing light and thereby rendering the PEM visible in a transmission mode (section 4.6.1). Namely, the island structure of the PEM area (image F) and PEM scraps left in the scratched region (image B) are identifiable. The surface of the PEM in the area presenting the island structure is rather mildly curved, while the surface of the PEM scraps is more curved as it can be concluded from the intensity of light refraction on these features. The regions free of PEM represent a flat surface (image B). Dry hybrids are attached to all three regions (the mildly curved surface, the highly curved surface, the flat surface) in a form of a predominantly periodically ordered monolayer (image A and E). The lattice constant of dry hybrids deposited on the flat surface is rather uniform, accounting to not more than 0.61 μm (evaluated from images A and E as an average distance between 30 closely positioned hybrids in the areas, where hybrids were resolvable). The estimation is limited by available imaging resolution, which does not enable assessment of apparent particle size and

apparent interparticle space of the deposit. Oppositely, on the curved surface, the lattice constant, as well as the apparent size of the hybrids and the apparent spacing between the hybrids, appears to be much greater than on the flat surface, yet variable. The curvature of the underlying surface appears to correlate positively with the other three parameters discussed. When rehydrated, this correlation is still present, but not easy to identify due to diminished contrast and presence of multilayer deposit (images C and G). This correlation is visible in Figure 34 and other photomicrographs not shown as well.

The phenomenon of the increased lattice constant of the hybrids (as well as the apparent size of hybrids and the apparent interparticle space of the hybrids) deposited on the curved PEM surface can be possibly justified by **light refraction on the curved PEM surface**. The curved surface probably acts as a magnifying glass creating an enlarged image of the objects in the vicinity of the surface. This hypothesis is supported by transmission *z*-stacks acquired at hydrated condition that indicate that hybrids of greater apparent size are placed at increased *z*-position in comparison to the hybrids of usual apparent size deposited on a flat area below (data not presented). The apparent interparticle space is plausibly below the resolution power and becomes observable only on the curved-surface areas magnifying the image. The deposited hybrids are probably closely packed as it is indicated by their periodic order independent from the curvature of the surface. Further research would be necessary to corroborate or refute the hypotheses discussed. Nevertheless, this is not in the scope of the work presented.

The **lattice constant evaluated at the dry state** of the hybrids deposited on the flat PEM surface (≤ 0.61 μm) is similar to the constant evaluated from the hybrids dried on a plain glass surface (0.60 μm; section 4.5; Figure 18, image B). This indicates, that the shrinkage of the hybrids by drying proceeds to an equivalent degree regardless of the attachment of the hybrids to the PEM surface.

The images C, D, G, and H of Fig. 24, acquired after rehydration, present important effects as well. The presence of periodic order of the deposited hybrids is reduced to very limited areas after the deposit rehydration. Therefore, the lattice constant cannot be evaluated from images C, D, G, and H. Instead, an average distance between two closely positioned hybrids can be evaluated. It is anticipated, that this value is equivalent to the lattice constant (section 4.5). Identification of the closely positioned hybrids can be a difficult task for human eyes. Nevertheless, since a uniform set of values was obtained, the closest possible distance between two particle cores was plausibly identified.

The average distance between two closely positioned hybrids after rehydration is about 0.92 μm in the basal (the first) layer of deposited hybrids (evaluated as average on 15 closely positioned hybrids of images C, G) and 0.93 μm in the volume of the deposited hybrid multilayer (evaluated as average of 19 closely positioned hybrids of images D, H). The average distance evaluated in the mass of the multilayer deposit is equivalent to the particle size since it is evaluated on directly attached hybrids. The lattice constant evaluated at the basal layer (0.92 μm) and in the upper layers (0.93 μm) of the deposited multilayer does not substantially differ. This indicates, that local **conditions in the vicinity to the PEM do not trigger additional shrinking/swelling of the hybrids** in respect to the layers more distant from the PEM surface. Moreover, from comparison of these values with the lattice constant of conclusively swollen hybrids in the deposit obtained by the drying-based approach for sandwich

preparation (1.0 μm; section 4.8.2), it can be concluded, that the hybrids presented here are in a swollen state. Hence, PLL, an anticipated glue of the sandwich (section 4.6 and Fig. 23) and a trigger of the non-thermal shrinking after penetration of the interior of the hybrids (section 4.9.1), is probably evenly distributed within the hybrid deposit obtained by the drying-based approach, but not substantially penetrating the interior of the hybrids.

During rehydration, the hybrids expand their size from less than about 0.6 μm to about 0.9 μm. Hence, the hybrids occupy more space. The need for additional space during rehydration leads to **spatial rearrangement of the hybrids deposited**. First, the zones of increased inter-particle distance are filled during rehydration (compare images A to C and E to G). Areas originally free of hybrids at dry state are filled after rehydration. Second, the increasing size of hybrids during rehydration may lead to an increase of horizontal pressure when the available space in a layer is occupied. This pressure is then released either by ejecting some of the hybrids into upper layers of the deposit (compare monolayer in image E versus multilayer in images G and H) or by delamination of the entire hybrid deposit from the PEM surface and formation of an invagination (Figure 29). These processes document strength, flexibility, and limits of the adhesion between the PEM and the hybrids on one hand and between hybrids on the other hand.

Importantly, hybrids attached already during sedimentation (Figure 23)—that were found to be shrunken probably due to PLL penetration into the interior of the hybrids—are indiscernible from the swollen hybrids attached by drying. It plausibly means that all hybrids in any part of the deposit depicted in Figure 24, images C, D, G, and H, are in a swollen state. This observation may indicate that the **PLL, penetrated into the microgels** attached to PEM during sedimentation, **was expelled** during the subsequent drying. Such reverse PLL release may be a consequence of hybrid collapse during the drying process or a consequence of washing the deposit by PLL-free buffer. Some results obtained during sandwich preparation indicate that washing by fresh buffer or mixing the buffer in the incubation chamber lead to reverse swelling of hybrids after their PLL-triggered shrinking (data not presented). Such reverse swelling is indicated in section 4.6.3, Figure 26 as well. More research in this direction could bring more solid answers.

Noteworthy, the hybrids deposited in the regions free of PEM (PEM was deliberately removed by mechanical scratching, images A–D) remain attached after rehydration by buffer and agitated washing similarly as hybrids attached to the PEM (images F–I). The documented **attachment of hybrids in the region of mechanically removed PEM** can be possibly facilitated by molecular remnants of PEM left on the surface after PEM removal, by the priming layer of PEI on the glass surface or by direct interaction between hybrids and glass surface as was already documented in Figure 19.

4.6.3 Centrifugation of hybrids

In an effort to accelerate the formation of a hybrid layer, centrifugation was employed instead of sedimentation (section 4.6.2). An application of centrifugal force was already reported in the literature as a possible way of microgel deposition from their suspension (South et al. 2009). The centrifugal force

is assumed to transport the hybrids towards the PEM surface and enhance attachment of hybrids by pressing the hybrids towards the PEM surface. A cooled centrifuge (Biofuge Stratos, Heraeus) with swinging rotor for well plates (up to 3000 RPM ~ 1400 g) was employed in this set of experiments. A well plate was milled in a way to accommodate and support the incubation chamber for glass slips during the centrifugation. The procedure of sandwich preparation followed here originates from the sedimentation-based procedure described in section 4.6.2 whereas centrifugation is employed instead of sedimentation. The centrifugation was performed at various temperatures (4–30°C), various relative centrifugal forces (160–1400 g), and various durations (range of minutes).

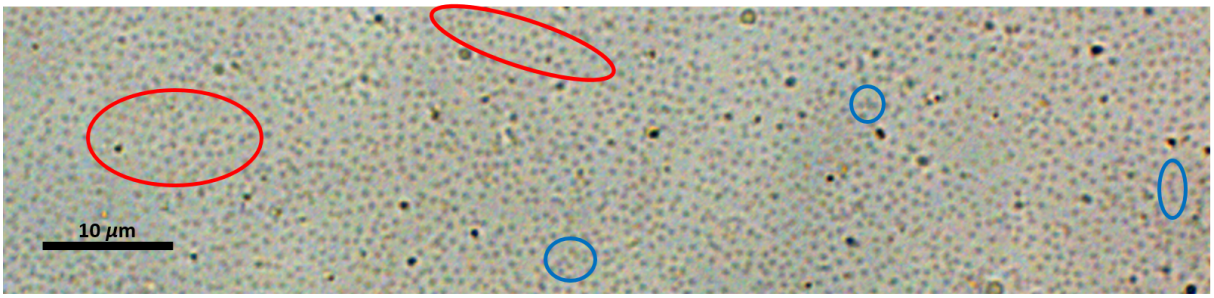

Fig. 25. Colour transmission photomicrograph of a hybrid deposit on PEM prepared by the centrifugation-based approach. The centrifugation was performed at a relative centrifugal force of 160 g for 10 min at ambient temperature. The photomicrograph was acquired at RT. Some of the periodically ordered areas are denoted by the red ovals and some of the hybrid clusters are denoted by the blue ovals.

As it is documented by Figure 25, a substantial amount of hybrids is accumulated on the PEM surface during centrifugation lasting for 10 minutes at relative centrifugal force of 160 g. The attachment of the hybrids to the PEM surface can be inferred from their ability to withstand solution mixing. Hybrids attach to the PEM surface exclusively as a monolayer. A rather small proportion of the deposit area resembles periodic order while the order of most of the hybrids deposited is distorted to a certain degree probably due to partial positional freedom of the hybrids. This state can be described as a *loose periodic order*. The lattice constant evaluated from the periodically ordered areas accounts to 0.84 μm (evaluated as the average distance between 21 closely positioned particles in periodically ordered zones of the deposit). Some of the periodically ordered areas are highlighted in Figure 25 by the red ovals. Simultaneously, a few hybrids are positioned substantially closer to each other than those in the periodically ordered regions. The particle-to-particle distance in these closely positioned regions accounts to about 0.65 μm (evaluated as the average distance between 12 closely positioned particles of the deposit). This value is probably equivalent to the particle size since it originates from the closest positioned hybrids of the deposit—probably clusters. Some of these clusters are highlighted in Figure 25 by the blue ovals.

The sandwich prepared by centrifugation, presented in Figure 25, resembles the results achieved after one day of hybrid sedimentation (Figure 23). Noteworthy, the hybrids did not only enrich at the PEM surface but **attached to the surface** as well. It indicates that centrifugation effectively brought the hybrids from their suspension to the PEM surface and substantially shortened the period of time needed

for attachment of hybrids to the PEM surface in comparison to the sedimentation approach. This acceleration is probably a consequence of centrifugal force, that presses hybrids towards the PEM and thereby keeps them in position while not allowing them to diffuse around. This is a major advantage over the sedimentation based method, where transport of hybrids to the PEM surface, as well as the attachment of hybrids onto the PEM, takes a rather long time.

The value of the lattice constant, found in the periodically ordered zones of Figure 25, is well comparable to the value of the lattice constant typically evaluated on closely packed hydrated deposits (e.g. figures 21, 24). Nevertheless, the particle-to-particle distance identified in sparse particle clusters as the ones presented in Figure 25 (0.65 μm) corresponds well to the usual values found in shrunken or dry hybrids (e.g. figures 18, 23, 24) indicating that the **hybrids are actually shrunken**. Comparing the value of the lattice constant measured in ordered arrays to the value of the particle-to-particle distance in clusters provides evidence that the packing is not close, although numerous regions show periodic order. The existence of periodic order may plausibly be explained by attachment of swollen hybrids on the PEM surface at the first place, followed by their shrinkage. The shrinkage may be caused by migration of PLL from the PEM to the interior of the hybrids (as discussed in section 4.6.2 and in the following paragraphs).

The centrifugal deposition was repeated at increased relative centrifugal force (1400 g) and prolonged time (30 min) of centrifugation to further increase the density of the hybrid deposit prepared. The centrifugation was performed at 4°C in order to prevent the formation of hybrid clusters or triggering the phase transition of hybrids due to heating of the sample during centrifugation.

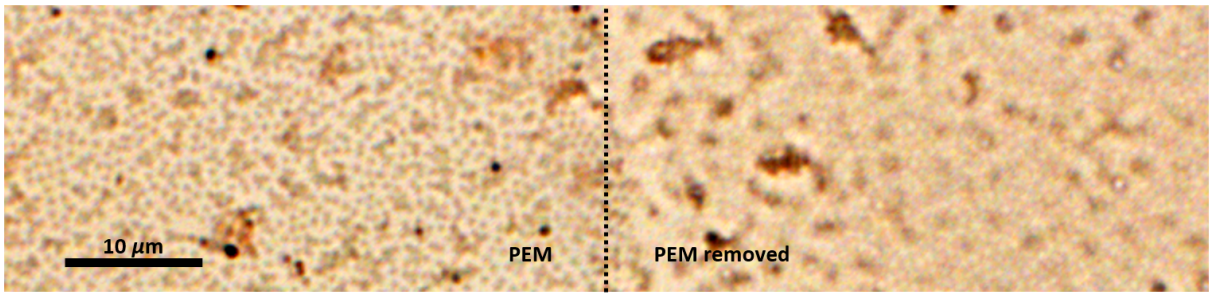

Fig. 26. Colour transmission photomicrograph of a hybrid deposit on the PEM prepared by centrifugation. Centrifugation was performed at the relative centrifugal force of 1400 g for 30 min at 4°C. The left part of the image represents the area of the sample with the deposited PEM while the right part represents an area of deliberately removed PEM (the scratched region). The object plane is positioned just above the layer of hybrids deposited on the PEM surface. The photomicrograph was acquired at RT.

Figure 26 presents a photomicrograph of a hybrid deposit on the PEM surface obtained after 30 min of centrifugation by relative centrifugal force of about 1400 g at 4°C. The deposit appears to be formed by a monolayer of hybrids and a sparsely presented hybrid clusters. The hybrids deposited on the PEM surface are loosely periodically ordered. The lattice constant evaluated in the ordered regions accounts to 0.87 μm (evaluated as the average distance between 21 closely positioned particles in the ordered regions of the deposit). The particle-to-particle distance in the clusters is estimated to not more than about 0.6 μm since the size of the particles is on the limit of resolution. Interestingly, in the region of

removed PEM, the photomicrograph documents a bulk of hybrids heaped-up on the sample surface during the centrifugation. These hybrids, accumulated on the bottom of suspension, produce relatively weak contrast and are therefore challenging to identify by naked eye. The accumulated hybrids are periodically ordered and the lattice constant evaluated accounts to 0.86 μm (evaluated as the average distance between 24 closely positioned particles in the periodically ordered regions of the accumulated hybrid particles).

Values of the lattice constant of the hybrid deposit, the particle-to-particle distance in clusters, and the ordering of the deposit obtained here are equivalent to those of the deposit prepared by centrifugation performed at lower speed and shorter period of time (Figure 25). This indicates that the centrifugation running more than 10 min and faster than 160 g does not substantially enhance the quality of the deposit any further. Despite the presence of free interparticle space between shrunken deposited hybrids, there are **no further hybrids filling the interparticle space** and attaching to the PEM surface. To do so, it would be probably necessary to reorganise the spatial positions of already attached shrunken hybrids in order to create free space for swelled hybrids approaching the PEM surface. Such a reorganisation force is probably missing here.

Interestingly, Figure 26 presents **hybrids accumulated on the surface of the substrate** (observable on the right side of the image) and the hybrids deposited on the PEM surface (documented on the left side of the image) side by side—at the identical *z*-position of the object plane. The image created in transmission mode by hybrids in these two regions substantially differs. The accumulated hybrids create an image of inverted and reduced contrast in comparison to the image of the hybrids deposited. The reduced contrast can be plausibly justified by the different swelling state: shrunken state of the deposited hybrids and swollen state of the accumulated hybrids. This justification is corroborated by the evaluated particle size of the deposited hybrids (≤ 0.6 μm), that corresponds well to the usual values found in shrunken or dry hybrids (e.g. figures 18, 23, 24, 25) and by the evaluated lattice constant of the accumulated hybrids (0.86 μm), that is equivalent to a typical lattice constant of closely packed swollen hybrids (figures 21, 24). The enhanced contrast of the attached hybrids probably masks an image created by swollen hybrids accumulated above them—at the same z-position as the hybrids visualized in the region of removed PEM. Possible attachment of the accumulated hybrids to each other was not examined, although it would be of interest.

A detailed examination of the complete sets of acquired images of the deposit presents another aspect of the system studied. As it is discussed above, the hybrid clusters, as well as the single hybrids attached to the PEM surface, are in the shrunken state while the accumulated hybrids in suspension are in the swollen state shortly after the centrifugation (Figure 26). The shrunken state of hybrids is probably caused by the PLL-triggered shrinking of the hybrids (sections 4.6.2, 4.6.3, 4.9.1) after penetration of the hybrid's interior by free PLL. Nevertheless, the hybrids bound in clusters swell again within a range of minutes after the centrifugation as can be inferred from increasing apparent particle size and diminishing contrast (data not presented). This observation can be possibly explained by the reduction of PLL concentration in the vicinity of the hybrid clusters and reverse **release of the PLL from the shrunken hybrids**. The clusters discussed are usually attached to the PEM by a single spot and thereby

somehow pivoting on the surface. An unintentional mixing of the suspension during the handling of the sample after the centrifugation may reduce the PLL concentration in vicinity of the PEM.

4.6.4 Drying at low temperature

It is anticipated that a multilayer deposit of rather low and uniform thickness is optimal for effective control over the molecular transport through this interface (section 2.2.4). Substantial thickness variability of deposits obtained by the drying-based approach (section 4.6.1), is caused by formation of hybrid clusters before deposition of the hybrids on the PEM surface. It is intended here to prepare a deposit of uniform thickness by cooling the sample during the process of suspension drying and thereby prevent cluster formation.

Practically, the PEM preloaded with PLL is overlaid by 200 μL of hybrid suspension and placed into a dry chamber—a sealed Petri dish filled with cold, dry silica gel absorber with $CoCl_2$ saturation indicator. The dry chamber with the sample is kept at 4°C until the microgel suspension dries-up, which takes at least one day usually. The same procedure was employed for the successful deposition of plain microgels on PEM as well.

The dry sandwich prepared by the procedure described here (image not presented) resembles the dry sandwich prepared by drying at RT (Fig. 24). Notably, most of the area of the dry sandwich is only partially covered by hybrids. During rehydration, hybrids swell within a minute and their size substantially increases. It leads to spatial rearrangement of hybrids deposited on the PEM surface and increased surface coverage, as is discussed in section 4.6.1.

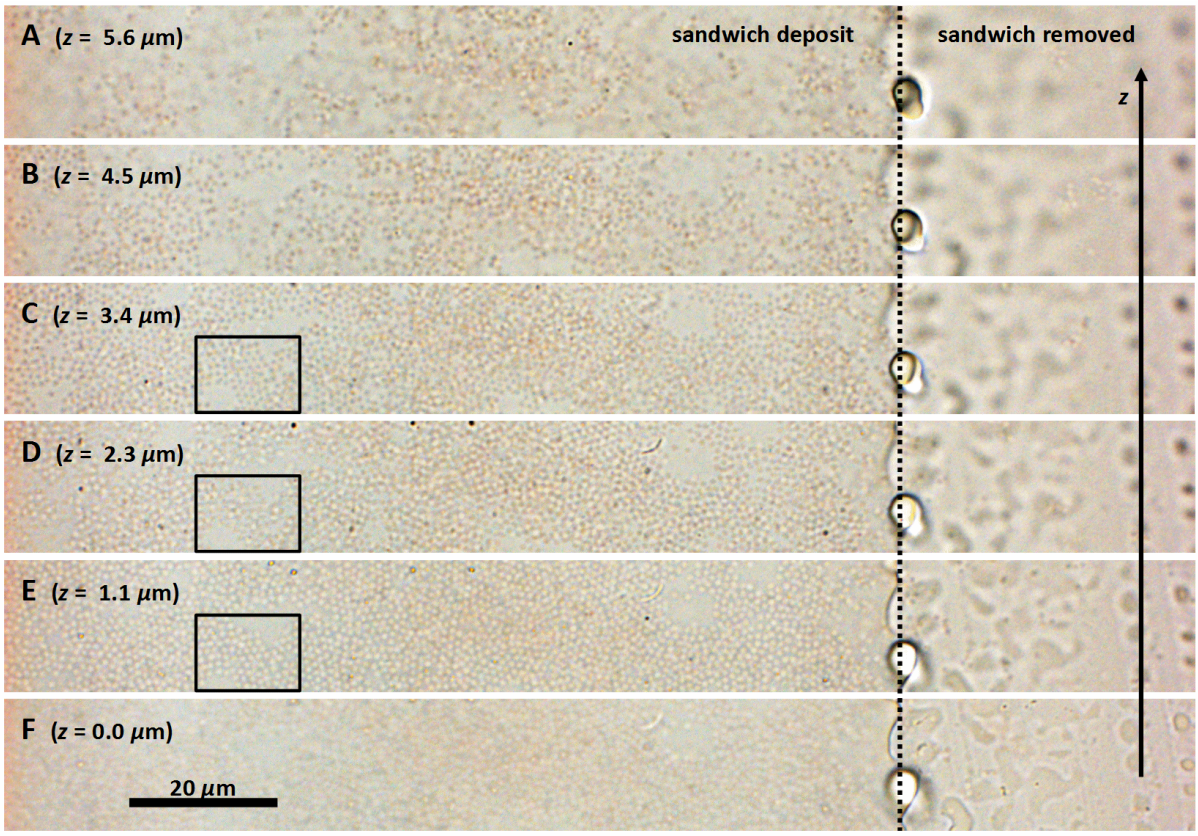

Fig. 27. z-stack of colour transmission photomicrographs of a sandwich prepared by the procedure of drying at low temperature and rehydrated in buffer. Image A corresponds to a position in the buffer just above the sandwich, image F corresponds to the z-position of the PEM. Images documenting the sandwich are displayed in between. The z-step between subsequent images is 1.13 μm. The accumulated z-distance is denoted in the captions of the images. The right side of every image represents a zone where sandwich is deliberately removed (the scratched region). The black rectangle denotes an area of deposit predominantly formed by a monolayer of hybrids. The hybrids are visualised in images C and E while being indiscernible in image D. Images were acquired at RT.

The rehydrated deposit prepared by drying at low temperature is documented in Figure 27. The deposit on top of the PEM is formed by a hybrid multilayer of variable thickness. Some small areas are not covered by the hybrid deposit. Most of the area is covered by one or two layers of hybrids. A few areas are covered by a multilayer that builds up to about 5 μm high. Most of the hybrids in the basal layer of the deposit are periodically ordered with the lattice constant accounting to 1.06 μm (evaluated as the average distance between 23 closely positioned hybrids in the periodically ordered region of the basal layer of the deposit displayed in image E of Figure 27). The lattice constant evaluated in the second deposited layer accounts to 1.07 μm (evaluated as the average distance between 20 closely positioned hybrids in the periodically ordered regions of the second layer of the deposit displayed in image B of Figure 27). This lattice constant is equivalent to the particle size since it originates from hybrids directly attached to each other. The attachment is strong enough to withstand solution mixing and NIR laser irradiation (section 4.7.3). The sandwich in the buffer environment is stable for at least half an hour at RT. Nevertheless, a small proportion of hybrids gradually detaches from the deposit shortly after rehydration in some cases.

By assessing the local variability of deposit height from the z-stack of images (Figure 27) in comparison

to the deposit prepared by drying at room temperatures (Figure 21), it can be concluded that drying at low temperature provides **deposit of reduced height variability** by a factor of approximately two. This is probably the consequence of drying performed at low temperature reducing the formation of hybrid clusters as is intended. Nevertheless, substantial variability between regions of one sample as well as between samples is still present regarding the deposit height and proportion of the uncovered areas. The regions uncovered by the deposit plausibly act as a completely open gate that may locally mask the intended gating effect of the surrounding deposit. A schematic overview of the sandwich preparation process by drying at low temperature is presented in Figure 28.

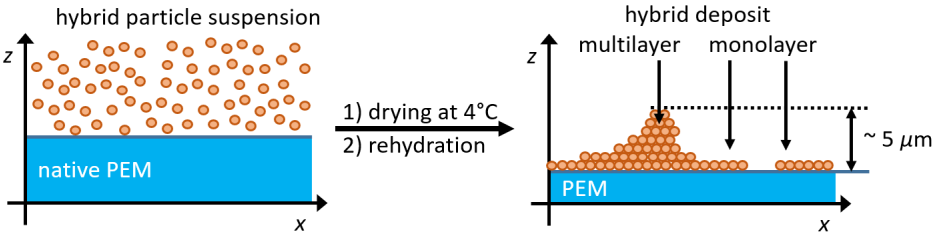

Fig. 28. Schematic diagram (cross-section) of the sandwich preparation technique based on hybrid suspension drying at 4°C. The left image depicts the sample before drying while the right image depicts the sandwich obtained after drying and rehydration.

Further, the height distribution of the deposit over the whole area of a sample was assessed. Relatively thin deposits occur in the centre while relatively thick deposits are located at the edge of the sample (data not presented). This **radial distribution of hybrid density** is probably caused by the presence of a concave meniscus during drying of hybrid suspension in incubation chamber. Since the geometry of the sample holder limits the area accessible to the microscope objective to the central region, the presented microscopy images are all acquired from the central region of the sample.

The evaluated lattice constants of the first and the second deposited layer of hybrids (1.06 μm and 1.07 μm, respectively) are nearly identical. Moreover, both lattice constants are equivalent to the lattice constants evaluated from other cases of hydrated closely packed multilayers (Fig. 21, Fig. 24). This equivalency indicates, that the basal layer, as well as upper deposited layers, are formed by **closely packed swollen hybrids** (assuming the conclusive close packing of upper deposited layers, section 4.5). Moreover, it indicates, that **the attachment to the PEM surface does not trigger any further shrinking or swelling** of the hybrids in comparison to the upper deposited layers of hybrids. The same is concluded for the deposit prepared by the method of drying at RT (Fig. 24).

The *z*-stack presented in Figure 27 is acquired with *z*-step width of 1.13 μm that is finer than the sectioning of other z-stacks presented in this work. This fine sectioning enables **visualization of the deposited particles twice at different *z*-position.** This phenomenon is well exemplified by the basal layer of the deposit since it is a well-defined plane. The hybrids of the basal layer (denoted by the black rectangle) appear as dark objects in image C, they are not observable in image D, and finally, they are again observable as bright objects in image E. The particles of the basal layer are too far from the object plane to be effectively visualized in the images B and F. This phenomenon is discussed in section 4.5 in

detail. Briefly, a particle is visualized by transmission microscopy as a bright object with a dark outline when the particle is further away from objective than the object plane and vice versa. An image of low contrast is produced when the object plane crosses the centre of the particle.

By careful refocusing, while observing the sandwich, it can be determined, that centres of the swollen hybrids deposited in the basal layer of the deposit are positioned about half a micrometer above the PEM surface. It indicates, that the hybrids deposited in the basal layer are **not embedded into PEM** but rather attached on-top of the PEM surface (data not presented).

The thickness of the PEM before and after performing the drying-based method of sandwich preparation was evaluated as well. The PEM thickness before drying accounts to about 4 μm whereas after drying and rehydration to only about 2.5 μm (section 3.9). This applies also for the case when hybrids are omitted from the drying procedure in order to prepare a reference sample. This phenomenon is discussed in section 4.7.3 and mostly 4.9.2.

Occasionally, an interesting phenomenon appears during rehydration of the dry deposit. The hybrid layer may peel off from the PEM surface while keeping a form of a layer protruding into the buffer (Fig. 29). This process is hereinafter referred to as the *delamination*.

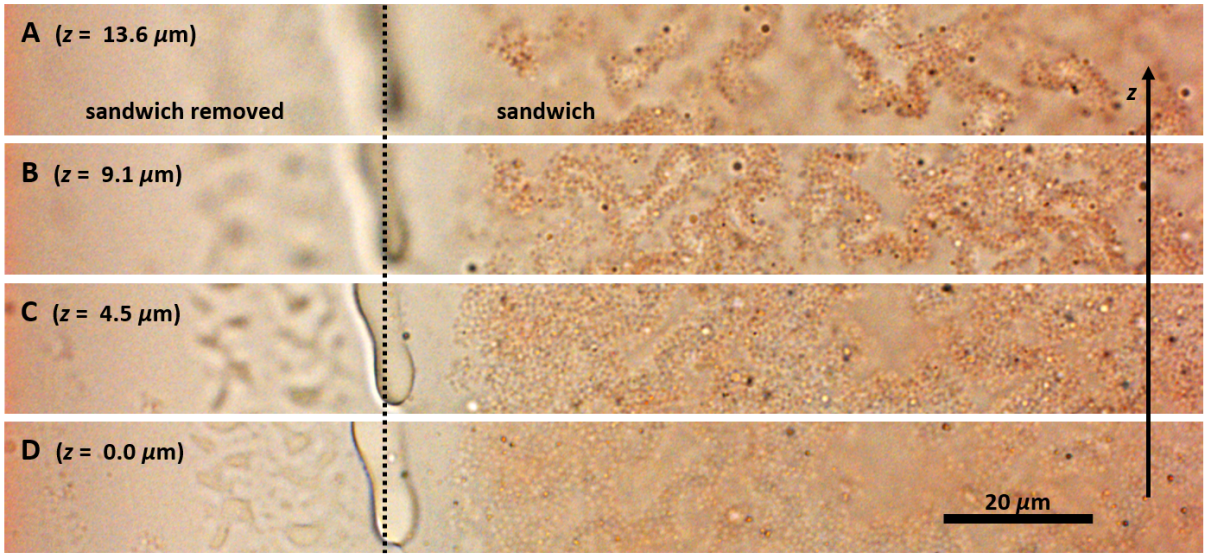

Fig. 29. z-stack of colour transmission photomicrographs depicting a hybrid deposit delaminated from the PEM surface. The sandwich is prepared by the drying-based method at low temperature and rehydrated in the buffer. The z-step between subsequent images is 4.54 μm. The accumulated z-distance is denoted in the captions of the images. Image A corresponds to a z-position in the buffer just above the sandwich while image D corresponds to the z-position of the PEM—visualising the basal layer of the hybrid deposit. The hybrid deposit in the delaminated zones extends through the complete z-span of the displayed stack. The left side of every image presents a zone where the sandwich is deliberately removed. Images were acquired at RT.

An example of the delaminated deposit is documented in Figure 29 by a set of transmission photomicrographs acquired at gradually increasing *z*-positions. The photomicrographs present a hybrid deposit of relatively uniform thickness deposited on the PEM surface. In the delaminated areas, the deposit on the PEM surface is missing while it is present as high as 15 μm above the PEM surface. By

manual refocusing of the sample during microscopy observation, an invagination of hybrid deposit extending high above the PEM can be clearly identified.

The delamination phenomenon was already discussed in section 4.6.2 (Fig. 24) as a consequence of the horizontal pressure building-up during the rehydration of the hybrid deposit. The proposed mechanism is briefly described here. The hybrids deposited by the drying procedure swell during rehydration, increase their size and occupy larger area on the PEM surface. In an ideal case, the swelling leads to the filling of the free space between dry hybrids that results in confluent coverage. When the theoretical coverage is greater than the available area, horizontal pressure within the hybrid layer builds up. This pressure can be released by the ejection of single hybrids into upper layers of deposit (section 4.6.2) or by the delamination of the complete hybrid deposit from the PEM surface while forming an invagination.

Finally, the procedure of sandwich preparation by drying of the hybrid suspension at low temperature was chosen as the optimal approach and further employed as a **standard approach for sandwich preparation**. This approach is therefore employed for the preparation of the sandwich employed for experiments documented in the sections 4.7, 4.8, 4.9, 4.10.

4.7 IR laser irradiation of the sandwich

One of the cornerstones of the work presented is the capability of the deposited hybrid particles to shrink under NIR light irradiation (section 2.2.1). The surface-attached PNIPAM microgels are documented to reversibly shrink at temperatures above 32°C (Nerapusri et al. 2006; Pacholski 2015; Yunker et al. 2014). The gold nanorods absorb light radiation of certain wavelengths while transforming it into heat. The wavelength of the LSPR absorption band of gold nanorods is known to be tunable by varying the aspect ratio of the nanorods (Nikoobakht and El-Sayed 2003). Gold nanorods presenting the absorption band in the NIR region are thereby available. It is documented in the literature, that PNIPAM microgels can be modified by gold nanorods, that results in the hybrid particles sensitive to NIR light while reacting by reversible shrinkage (Gorelikov, Field, and Kumacheva 2004; Karg et al. 2007). This feature is intended to be employed for the purpose of the work presented here and therefore it needs to be conserved after hybrids are attached in a form of deposit layer to the HA/PLL PEM surface that is not well documented in the recent literature until now.

The sandwiches prepared by various methods, as described in section 4.6, were tested for susceptibility to NIR light shortly after their preparation. The samples in a buffer environment were irradiated by NIR laser light while simultaneously observing a reaction of the sandwich by means of light transmission microscopy.

4.7.1 Sandwich prepared by drying

Drying of hybrid suspension on the PEM surface let to the successful attachment of hybrids as was

described in section 4.6.1 (drying at RT) and 4.6.2 (drying at 4°C). The prepared sandwiches were rehydrated by buffer and a chosen area of the deposited hybrid monolayer was irradiated by laser. Photomicrographs documenting the influence of irradiation by NIR laser on the swelling state of the deposited hybrids are displayed in the following Figure 30 and Figure 34. The observed reaction of sandwiches prepared by the drying-based method at RT or at 4°C is equivalent.

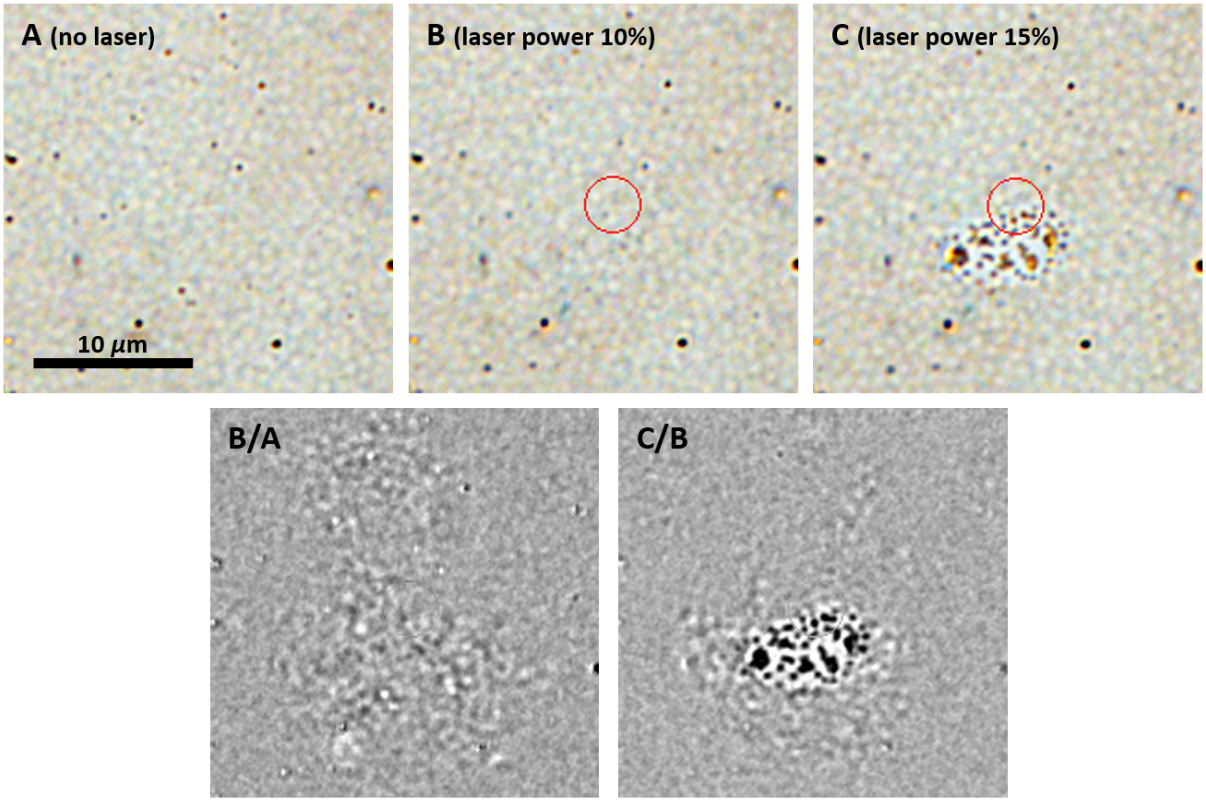

Fig. 30. Transmission photomicrographs of hybrid deposit in the buffer environment irradiated by NIR laser of various power. Image A: no irradiation. Image B: irradiation by the focused laser of 10% power. Image C: irradiation by the focused laser of 15% power. The photomicrographs were acquired from the identical area of the sample in the time-sequence as presented. The area irradiated is marked approximately by the red circle. Image B/A was obtained by monochromatization and division of image B by image A. The image obtained enhances the differences between the images A and B. Image C/B was obtained equivalently to image B/A. The object plane of the objective crosses the position of the hybrid deposit. Photomicrographs were acquired at ambient temperature. The sandwich preparation was described in section 4.6.2.

Image B of Figure 30 documents rather insignificant changes of the state of deposited hybrids upon irradiation by a laser of 10% power in comparison to the state without irradiation (image A). This can be further concluded from image B/A, which enhances the differences between the corresponding photomicrographs. Upon irradiation by a laser of 15% power (image C), the state of hybrid deposit substantially differs from the state without irradiation. This is clearly indicated by image C/B as well. Darker, more contrasting, and somehow smaller hybrids are present in the irradiated area in comparison to the hybrids surrounding the irradiated area. The spatial distribution of most of the shrunken hybrids over the PEM surface is unchanged. A minor proportion of the irradiated hybrids forms clusters of few particles that remain attached to the PEM surface. Importantly, Figure 30 documents that the hybrids

attached are not removed from the PEM surface by the laser irradiation.

All documented **changes in the image created by hybrid particles** following the laser irradiation can be explained by their heat-triggered shrinkage. **First,** the reduction of the apparent diameter of the irradiated hybrids presumably corresponds to the thermally-triggered shrinking of the hybrids. Nevertheless, the visual assessment of change of hybrid diameter from a transmission photomicrograph is weak evidence as is discussed in section 4.5. As the diameter of the irradiated hybrids deposited on the PEM surface reduces, a free void between the hybrids expands. This free void is well documented in image C. **Second,** the hybrids in the irradiated region appear darker in comparison to hybrids out of the irradiated region. This effect is probably a consequence of hybrid shrinkage leading to reduced particle diameter and thereby lower position of the particle centre relative to the PEM surface in comparison to the position of the swollen particle centre. A scheme of such a situation is displayed in Figure 31. Hybrid particles are visualised as dark or bright objects with a contour depending on their *z*-position relatively to the object plane of the objective since every hybrid particle acts as an optical lens (section 4.5). **Third,** the hybrids irradiated appear more contrasting than the hybrids out of the irradiated zone probably due to a combination of two effects, that intensify the light refraction: reduced particle diameter and increased refractive index due to the water excretion from the microgels upon shrinking. **The three aforementioned effects** indicate that the NIR laser irradiation of hybrids induces their thermally-triggered shrinkage. Noteworthy, the acquired photomicrographs document the capability of a transmission photomicroscopy to discriminate between the swollen and the shrunken state of the surface-deposited hybrid particles.

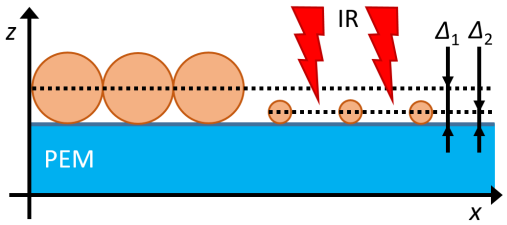

Fig. 31. Schematic representation (side view) of a sandwich with hybrid particles in the swollen state (larger spheres) and hybrid particles in the shrunken state induced by IR laser irradiation (smaller spheres) deposited on the PEM surface. The parameters Δ_1 and Δ_2 denote the distance between the PEM surface and centres of the swollen or the shrunken hybrids, respectively.

The laser of 10% power (Figure 30, image B) induces a very limited reaction of the hybrids, while the laser of 15% power (image C) induces the characteristic thermally-triggered shrinking. This demonstrates the presence of a laser power **threshold for the occurrence of the thermally-triggered shrinking**. This threshold is plausibly related to the temperature distribution around the irradiated region exceeding the phase transition temperature of PNIPAM as is displayed in Fig. 32. Furthermore, the equivalent explanation is applicable to the presence of another phenomenon as well.

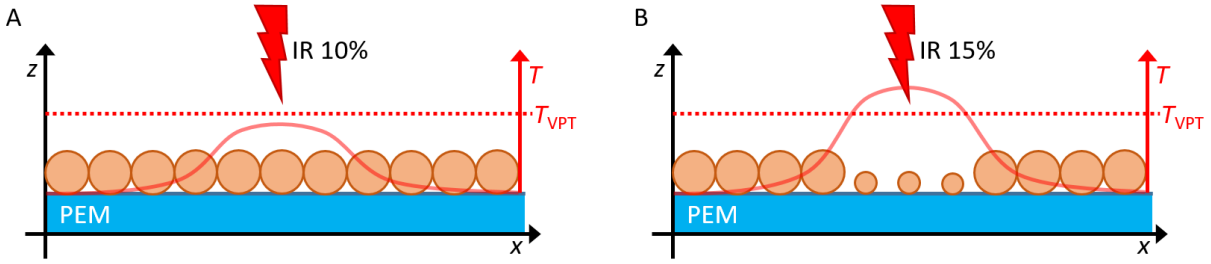

Fig. 32. Schematic representation (side view) of the proposed temperature profile created by IR laser of different power by irradiating the hybrid deposit. Image A represents the situation when the temperature created by the laser irradiation does not exceed the volume phase transition temperature (T_{VPT}) in any area of the deposit. Image B represents the situation when the threshold temperature is locally exceeded leading to the thermally-triggered shrinking of the deposited hybrids. The scheme is meant to document the situations displayed in Figure 30, images B and C.

The heat produced by AuNRs, irradiated by the CW NIR laser, quantitatively dissipates at least units of micrometers away already after several microseconds of the irradiation (Keblinski et al. 2006; Nguyen et al. 2016). Moreover, the laser employed is not in perfect focus at the object plane. Hence, it can be estimated that **the temperature distribution** across the plane of the hybrid deposit established during laser irradiation can be approximated on a micrometer scale by a smooth decreasing function of distance from the irradiated centre as is denoted in Figure 32.

Despite the relatively smooth thermal profile, image C of Figure 30 documents **rather sharp spatial boundary** between the area of shrunken hybrids and the surrounding swollen hybrids. This indicates, that the on/off character of the volume phase transition, typical for pure PNIPAM microgels, is still conserved in this complex sandwich system. When the laser is deliberately defocused, the area of shrunken hybrids expands (Fig. 34, Fig. 36). This indicates that the radial distribution of the laser power effectively influences the spatial extension of the created thermal profile. The equivalent effect—the increasing size of the area of shrunken hybrids—is not significant when only laser power is increased. When the hybrids are irradiated by the laser of excessively high power, the local temperature rises above the boiling point of the surrounding medium and a bubble of vapour forms (data not presented).

The irradiation of the sandwich by laser has another consequence as well. A **flow of the liquid medium in the vicinity of the irradiated area** is observable when the medium contains a suspension of hybrid particles or other suspended particles visualizing the flow (data not presented). The liquid flows radially along the sandwich surface towards the irradiated region and after entering this region it rises towards the surface of the medium. Weakly attached hybrids may be removed by the liquid flow, while well-attached hybrids (most of the deposited hybrids) withstand the forces arising from the liquid flow. The radial flow along the surface extends into a distance of at least hundreds of micrometers. Therefore this phenomenon cannot be explained by molecular thermophoresis since the thermophoresis is driven by thermal gradient directly. The observed phenomenon can be rather explained by the convective flow induced by the increased temperature of the medium. This convective flow enables fairly effective mass transport in the solution nearby the irradiated area as well as some extent of cooling by transporting a colder medium to the heated region. This may play a certain role for elucidating why the sandwich area

presenting the thermally-shrunken hybrids upon laser irradiation (Figure 30, image C) is somehow smaller than can be assumed by considering the thermal diffusivity in water (about 0.14 $\mu m^2/\mu s$) solely.

A further important aspect of the shrinking of deposited hybrids triggered by laser irradiation and reverse swelling is **kinetics**. **First**, it is observed that the hybrids attached to the PEM surface shrink in not more than a fraction of a second after the onset of the laser irradiation. The reverse process—swelling—proceeds for about a second until hybrids become fully swollen again after the laser goes off. This illustrates the rate of the swelling, as well as the rate of heat dissipation, of every single hybrid particle. **Second**, the spatio-temporal extension of the thermal profile created by the laser-irradiation of the sandwich can be inquired from the observable area of shrunken hybrids. It is observed, that the stable extension of the area of shrunken hybrids is established within not more than a fraction of a second after the onset of the irradiation. It indicates that the stable spatial extension of the thermal profile on a micrometer scale is established in a relatively rapid manner as well. The reverse disappearance of the area of shrunken hybrids after the laser goes off proceeds similarly rapid. The rapid rate of establishment of the thermal profile when the laser goes on as well as its rapid disappearance when the laser goes off documents effective heat dissipation in the system. The heat dissipation is probably advanced by the convective flow of buffer medium around the heated region as discussed in the paragraph above. Since all four mentioned processes are relatively rapid, it was not possible to acquire corresponding data with the equipment employed.

A particularly interesting aspect of the shrinking of the PEM-deposited hybrids is **the spatial rearrangement of the hybrids**. The integrity of sandwich arise from the PEM–hybrid attachment and the hybrid–hybrid attachment, that are documented by physical stability of a multilayer deposit (section 4.6.1). The quality of this attachment define the development of the sandwich under the strain induced by the shrinking of the hybrids. Figure 30 documents a typical case. A major proportion of hybrids in the monolayer deposit keeps the spatial position of the hybrids upon thermally-triggered shrinking while the interparticle void expands. This implies that the strength of the PEM–hybrid attachment dominates over the hybrid–hybrid attachment in this case. A scheme depicting the situation discussed is displayed in Figure 33, zone A. An opposite situation is presented in Figure 30 as well. A minor proportion of shrunken hybrids forms small clusters indicating, that the hybrid–hybrid attachment locally dominates over the hybrid–PEM attachment in a measure of strength or rigidity. When a multilayer of hybrids is deposited on the PEM surface, the cumulative strength of hybrid–hybrid attachment usually dominates over the hybrid–PEM attachment. Consequentially, the deposit shrinks predominantly in a form of clusters (data not presented). A scheme depicting the situation discussed is depicted in Figure 33, zone B.

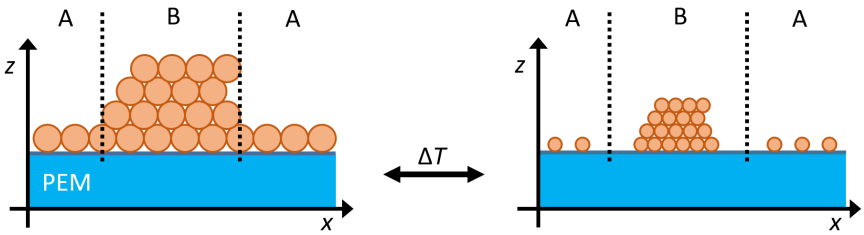

Fig. 33. Schematic diagram (side view) of the hybrid deposit on the PEM surface undergoing a transformation upon the thermally-triggered shrinking of the hybrids. The deposited hybrid particles (orange spheres) are in the swollen state at RT (left image) or in the shrunken state at elevated temperature (right image). The transformation proceeds by either of two typical scenarios depending on the dominant attachment force of the hybrid particle to its environment. Zone A denotes the case, which is characteristic by the collective hybrid-PEM attachment being stronger/tougher than the collective hybrid-hybrid attachment. This case is typical for the monolayer deposits. Zone B denotes the opposite case, which is typical for the multilayer deposits.

Two presented scenarios of spatial redistribution of hybrids upon shrinking document an elastic character of the discussed attachment and limits of its extension.

Reversibility and repeatability of the shrinking–swelling cycle of the hybrids in the deposit is an important aspect of the system developed as well. Therefore, these aspects were assessed by a brief—a few seconds lasting IR laser irradiation, that triggers the local shrinking of hybrids in the sandwich while observing the changes induced by the irradiation.

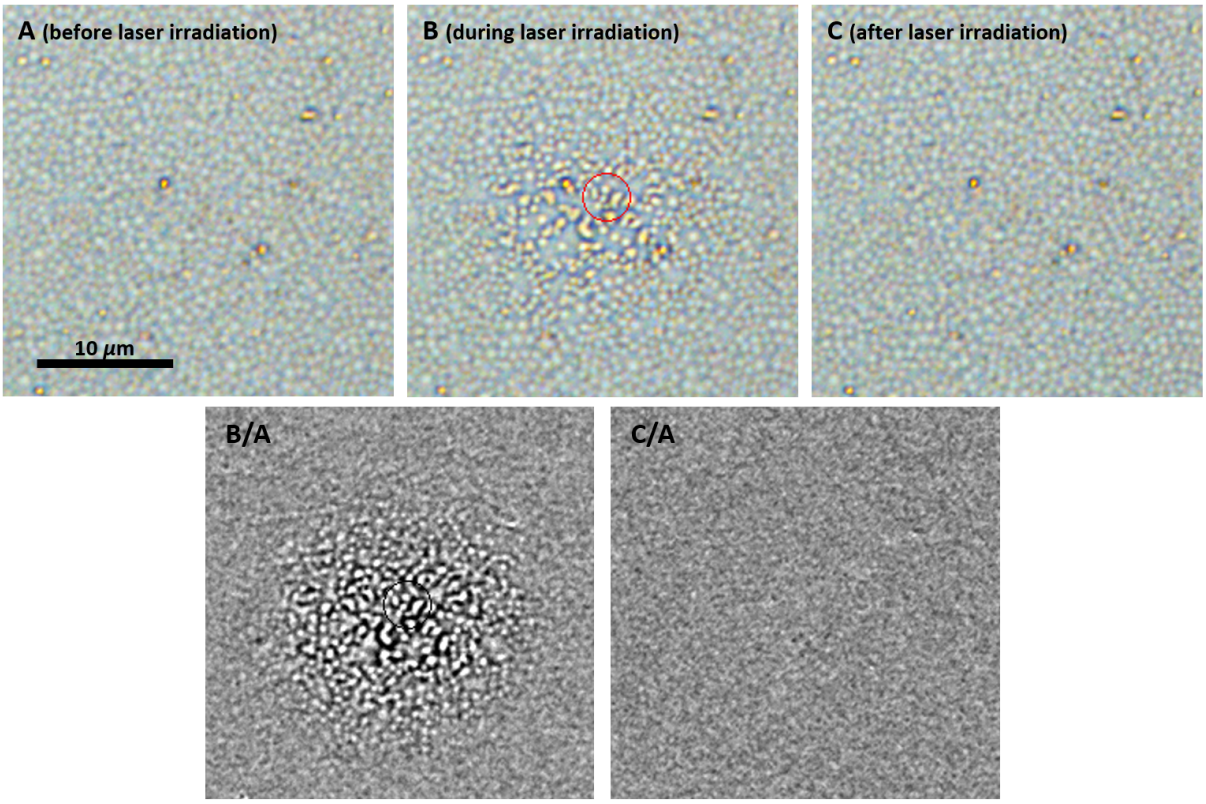

Fig. 34. Transmission photomicrographs of the sandwich in a buffer environment at various stages of laser irradiation. Image A: before laser irradiation. Image B: laser irradiation by focused NIR laser light of 20% power, duration of several seconds, a nominal centre of the irradiated area marked by the red circle. Image C: after the irradiation. The images were acquired on the same area of the sample. Image B/A was obtained by monochromatization and division of image B by image A. The image obtained enhances differences

between the corresponding input images. For image C/A applies the equivalent as for image B/A. The object plane is placed at the PEM surface approximately. Photomicrographs were acquired at ambient temperature. The preparation procedure of the sandwich is described in section 4.6.2.

Figure 34 depicts the deposit formed predominantly by a monolayer of hybrids. The reversibility of the effects following the laser irradiation was assessed as follows. The differences between the state of the deposit before and during the laser irradiation as well as before and after the irradiation are highlighted in the images B/A and C/A, respectively. First, image B/A indicates the shrinking of the hybrids and a certain level of their spatial rearrangement upon laser irradiation. The changes, visualized by image B/A, are spatially more gradual and spread over a greater area in comparison to the changes as can be inferred from image B alone. Second, image C/A documents no major difference in the spatial arrangement and swelling of hybrids after irradiation in comparison to the state before the irradiation. It indicates that the shrinking and spatial rearrangement of the surface deposited hybrids following their brief laser irradiation are fully reversible. Nevertheless, longer-lasting laser irradiation induces irreversible changes as is described in section 4.7.3. Finally, the shrinking–swelling cycle is repeatable at least tens of times as can be inferred from repeated short-lasting irradiation of the sandwich by the laser light (more cycles were not tested).

A force action of laser on attached hybrids is another disputable aspect of the IR laser irradiation. The mode of the IR laser irradiation employed is equivalent to the mode of **optical tweezers**. Therefore, the irradiation may manifest itself as a force on the hybrid particles, that is directed towards the focus of the IR laser. Nevertheless, figures 30 and 34 do not document any prominent displacement of the irradiated hybrids towards the centre of irradiation. It indicates, that the magnitude of this force is too small to play a significant role in the displacement of the deposited hybrids.

4.7.2 Sandwich prepared by sedimentation or centrifugation

The sandwiches prepared by the procedure of hybrid suspension sedimentation (as described in section 4.6.2) or centrifugation (as described in section 4.6.3) were examined for their susceptibility towards irradiation by IR laser. The observed characteristics of sandwiches prepared by sedimentation and centrifugation were equivalent. The effects following the irradiation are documented in Figure 35.

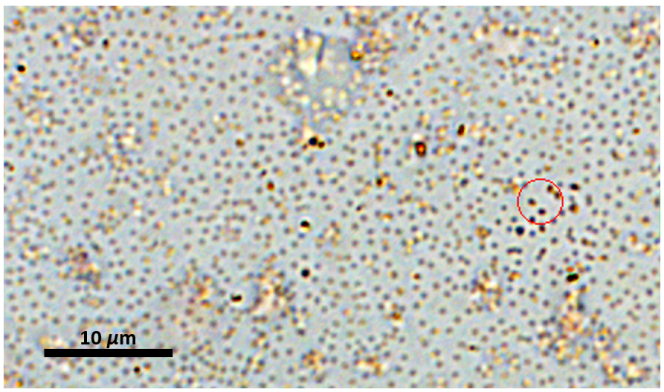

Fig. 35. Colour transmission photomicrograph of a hybrid deposit on the PEM surface in the buffer environment while irradiated by IR laser. The area irradiated is approximately marked by the red circle (on the right side of the image). The object plane passes just above the basal layer of the hybrids deposited. Irradiation is performed by the laser of 15% power and the focus of the laser matching the object plane. The photomicrograph is acquired at ambient temperature. The sandwich preparation employed is described in section 4.6.2.

The photomicrograph documents that the hybrids under laser irradiation are visualised as darker objects in comparison to the hybrids positioned out of the irradiated area. The apparent size of the irradiated hybrids does not differ any significantly from the apparent size of the hybrids positioned out of the irradiated area. The slight change of hybrid brightness indicates that the hybrids are actually irradiated and probably undergo shrinking to a limited extent. The relation between the visualised state of hybrids and the actual swelled/shrunken state of hybrids is discussed in section 4.6.1. The extent of shrinkage induced by the laser irradiation is substantially reduced in comparison to the extent of the shrinkage following the laser irradiation of a sandwich prepared by the drying-based method (section 4.7.1). This limited ability of the hybrids to shrink is in accordance with the conclusion drawn in the section on preparation of the sandwich (section 4.6.2 and 4.6.3). It states that the hybrids deposited by sedimentation- or centrifugation-based method are already at a certain level of the shrunken state.

4.7.3 Thermally-induced swelling of PEM

The laser-induced heating of the sandwich influences not only the state of the hybrids in the deposit but the state of the underlying PEM as well. When the sandwich is irradiated by laser for a rather short period of time (up to a minute approximately), the morphological changes of the PEM induced are minor and instantaneously reversible after the laser goes off and the heat dissipates (data not presented). When the sandwich is irradiated for a longer period of time, some of the heat-induced changes of the PEM are not fully reversible any more. The process of thermally-induced transformation of PEM during the long-term irradiation is documented in Figure 36. In order to keep the heat production by laser irradiation steady over a prolonged period of time, a deliberately defocused laser beam is employed rather than the focused laser beam. The area of a sandwich influenced by the laser grows larger with the defocusing of the laser. Thereby, the consequential effects are easier to resolve and less dependent on the actual spatial distribution of the hybrids in the irradiated area.

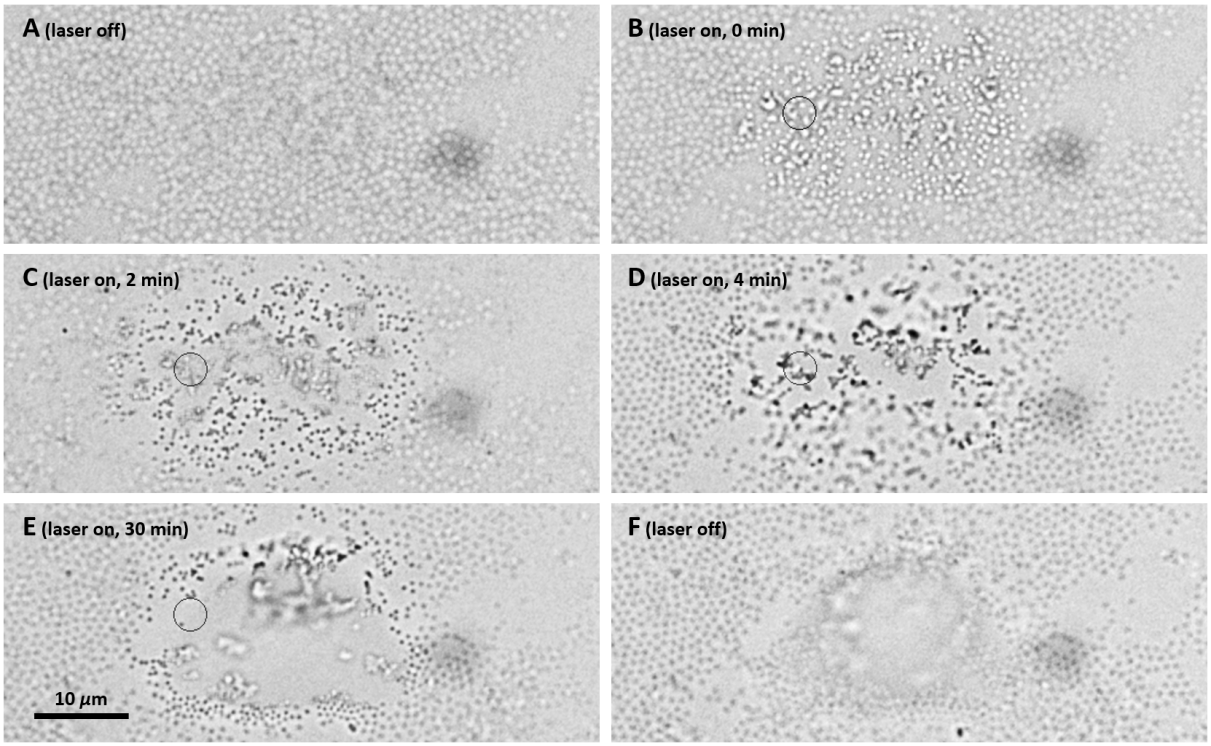

Fig. 36. Time sequence of monochrome transmission photomicrographs depicting the sandwich in the buffer environment under a long-lasting IR laser irradiation. The laser activity and the time after the start of the irradiation is indicated in the captions of images. When the laser is active, the nominal centre of the laser-irradiated area is marked by the black circle of about 5 μm size. All images presented are corrected for artefacts by a flat field image. Loading of the sandwich with dextran was performed between the images D and E (section 4.9.2).

Image B of Figure 36 documents, that the hybrids shrink instantaneously after laser irradiation is activated—as is discussed in section 4.7.1. After about 2 minutes of continuous laser irradiation (image C), the *z*-position of some hybrids in the irradiated region increases relative to the *z*-position of the surrounding hybrids. The *z*-position of a hybrid particle relative to the object plane can be inferred from the brightness of the visualized particle as is discussed in sections 4.5 and 4.6.4. The alteration of the PEM thickness in the irradiated zone is indirectly indicated this way since the hybrids are still attached to the PEM surface. As the time of irradiation progresses (images D and E), the thickness and the size of the morphologically transformed area increases. Concomitantly, the hybrids deposited in the irradiated region progressively form clusters. Finally, the laser is deactivated after half an hour lasting irradiation (image F), the thickness and the size of the morphologically transformed area abruptly reduce, but it does not recover to the state before the irradiation.

The gradual increase of the PEM thickness during the irradiation can be explained by the **thermally-induced swelling of the PEM**. The swelling is probably a reverse process of the PEM thickness reduction, that occurs during the drying-based method of the sandwich preparation (section 4.9.2). The increased temperature in the irradiated region probably leads to the weakening of attachment between oppositely charged polyelectrolytes. It enables the water molecules to enter the PEM and compensate the charge resulting in swelling of the heated region. Interestingly, during systemic heating of the sandwich from room temperature to about 50°C, there is no recognisable alteration of the PEM

thickness as is determined by an independent assay employing microscopy (section 4.8.2) or spectroscopy (section 4.8.1). It indicates that the temperature leading to the thermally-induced swelling of PEM is higher than about 50°C. Thereby it can be concluded, that the temperature of the sandwich in the laser-irradiated region under the conditions employed here plausibly exceeds 50°C.

Due to the spatial rearrangement of the deposited hybrids following the thermal swelling of the PEM in the irradiated region, the **efficiency of the IR light transformation to heat** is probably altered. The swelling process rather removes the hybrids from the centre of the irradiated area as indicated in image E. Nevertheless, the sudden morphological changes of the sandwich in the irradiated zone following the laser deactivation indicate that a substantial amount of heat is still being produced even after half-hour lasting irradiation. A plain PEM and a PEM with deposited unmodified microgels were irradiated by the laser in an equivalent experimental setting serving as a control experiment. There are no observable changes in the PEM morphology, the sandwich morphology, or microgel swelling state after a short- as well as long-time period lasting laser irradiation (data not presented).

4.8 Sandwich response to ambient temperature

The reaction of the deposited hybrids induced by the laser irradiation is identified as the thermally-triggered shrinking of the hybrids in section 4.7.1. To verify that the phenomena observed arise from the heating and not from the laser irradiation itself, a sandwich was systemically heated up while following the effects of thermally-triggered shrinking. Absorption spectroscopy and transmission microscopy were therefore employed.

4.8.1 Spectroscopy analysis

A sandwich deposited on a single side of a glass slip inserted into a temperature-controlled spectroscopy cuvette filled with diH_2O serves as a sample. The glass slip is placed diagonally in the cuvette—under approximately 45° of angular deflection from the incident light beam. The absorbance of the sample is anticipated to be very weak since the sample is a surface deposited layer. Therefore, careful assessment of the background signal was performed before every set of measurements (data not presented). The light reflection on glass surfaces and absorption of water were identified as the main components of the background signal. The signal arising from the surface reflection is spectrally invariant in the examined interval of wavelengths (400–1100 nm). Water introduces an absorption shoulder rising towards the red end of the spectrum and a dominant absorption peak centred at about 975 nm (A_{975} ~ 0.2). Minor absorption peaks of water, centred at about 740 nm and 840 nm, are projected into the data recorded as well. These features of the water absorption spectrum are endorsed by literature (Waggener 1958).

A further control experiment was performed to characterise the changes in the absorption spectrum arising from the systemic heating of a control sample. The control sample—a native PEM deposited on one side of a glass slip immersed in a water-filled cuvette—was heated from 10°C to 50°C in a stepwise

manner of 5°C steps, and afterwards cooled back to 10°C in a reverse manner (the *thermal cycle*). The spectra acquired during the thermal cycle are documented in Figure 37.

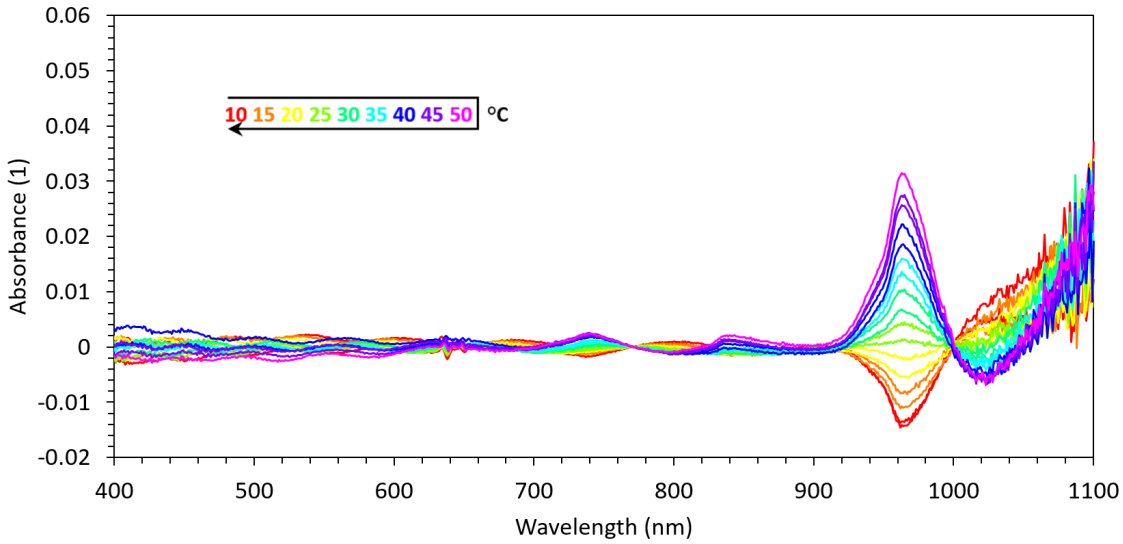

Fig. 37. Absorption spectra of the control sample at various temperatures of the thermal cycle. The control sample is the native PEM deposited on a single side of the glass slip inserted in a water-filled cuvette. The sample was heated in a stepwise manner from 10°C to 50°C and afterwards cooled back to 10°C while recording a spectrum every 5°C (~ the thermal cycle). The absorbance of every single spectrum is adjusted by offsetting the absorbance values during data post-processing to match the zero absorbance at 770 nm wavelength. All spectra are related to the identical blank acquired with a sample consisting of a plain glass slip in diH_2O at 23°C.

The spectra presented in Figure 37 document three well-pronounced temperature-variable absorption peaks centred at approximately 740 nm, 840 nm, and 965 nm. The absorbance of these peaks is positively associated with the temperature. The temperature-dependent changes are mostly reversible as documented by the spectral pair recorded at 10°C—the first and the last spectra of the temperature cycle. Nevertheless, other spectral pairs acquired at the same nominal temperature during positive and negative temperature sweep are similar but not identical as they exhibit a certain shift. Further, the spectra present a kind of fringe pattern at its blue end. The spectral position of the fringes weakly correlates with temperature. Lastly, the spectra present a constant rise of absorbance towards their red-end and rather random inclined ramp of absorbance towards their blue-end.

The spectral position of the three temperature-variable absorption peaks identified overlaps with the spectral position of three absorption peaks of water as it was determined in a baseline measurement and is discussed at the beginning of this chapter. Hence, it can be concluded that the three temperature-variable absorption peaks originate from the **thermal dependence of water absorption.** The minor temperature-variable peaks centred at 740 nm and 840 nm probably interfere with the fringe pattern in a constructive manner, which leads to partial alteration of peak shape and amplitude. Therefore, the component of actual water absorbance in these peaks is probably lesser than their size displayed.

The incomplete match between a pair of absorption spectra acquired at the same nominal temperature originates plausibly from incomplete stabilisation of the sample temperature during the thermal cycle.

Only the acquisition of the spectra recorded at 10°C were granted a prolonged equilibration time to stabilise the sample temperature closer to the nominal temperature, which leads to closer matching of absorbance values at the positions of the temperature-variable peaks.

The width of fringes in the **fringe pattern**, that appears at the blue end of the spectra (Figure 37), is positively associated with the wavelength of the probe light—the fringes become broader as the wavelength of probe light increases. Such association is typical for light interference on a thin layer. It indicates, that the fringe pattern probably stems from light interference on a thin layer—plausibly on the PEM since this layer is thin enough and smooth. The origin of the fringe pattern is corroborated by a control experiment employing only a plain glass slip (no PEM), that presents no fringe pattern in the acquired spectra (data not presented). Moreover, the light interference on the glass-deposited PEM is observable by a naked eye as a characteristic rainbow-coloured pattern appearing in reflected light. Based on the geometry of the sample, the thickness of the PEM can be evaluated from the width of the fringes. The spectral distance between all identifiable subsequent constructively-interacting interference maxima was assessed from every spectrum of the thermal cycle. A set of spectral distances as a function of the probe light wavelength was employed to invert the thickness of the layer responsible for interference. Such fringe pattern analysis of the thickness of the PEM results to about 3.4 μm. The thickness evaluated corresponds well to the thickness of a native PEM, as determined by means of microscopy (~ 4 μm).

The PEM thickness was evaluated from every spectrum of the thermal cycle acquired. The data obtained do not indicate any substantial **association of the thickness of the PEM with the temperature** in the interval examined (10°C–50°C). This finding is in agreement with the microscopy observations (section 4.8.2).

Although there is no substantial thermal variation of the fringe width present, the fringe patterns acquired at different temperatures are shifted in a spectral dimension proportionally to the temperature. This association can be possibly explained by the physical bending of the glass slip inside the cuvette during the thermal cycle, which results in variations of the angular deflection of the glass slide from the incident light beam. This bending is a consequence of physical stress, that plausibly arises from a tight fit of the glass slip in the cuvette in combination with the thermal expansion coefficient of the borosilicate glass slip being substantially lower than the coefficient of a polystyrene-based cuvette. The presence of this stress is corroborated by occasional breakage of the glass slip in the cuvette during the cooling phase of the thermal cycle.

Every single spectrum of figures 37 and 38 is adjusted by off-setting in order to match the zero absorbance at 770 nm. The need for such adjustment originates from **an unequal baseline** of the spectra acquired at different temperatures. This baseline inequality is wavelength-independent and its extent is loosely positively associated with temperature. A possible cause of this effect is the bending of the glass slip inside the cuvette during the thermal cycle. This bending is already discussed in the previous paragraph. The bending plausibly leads to alteration of the incident light angle followed by altered light reflection on the glass surface. This explanation is in general agreement with Fresnel relations. The reflection phenomenon is only negligibly wavelength dependent under the conditions

employed here, as is indicated by Fresnel equations involving thermal variability of refractive indices of glass and water. Therefore, the unequal baseline can be corrected by simple off-setting the spectrum on the absorbance axis. The adjustment point at 770 nm was chosen since the absorbance of hybrids at this wavelength is thermally invariant. It is documented by the absorption spectra of hybrid suspension recorded at various temperatures (section 3.1).

Lastly, the steady positive or negative ramp of absorbance towards blue- and red-end of the spectra is associated rather with time of the data acquisition than with temperature of the sample. It indicates that these changes are caused by weakly controlled parameters influencing the measurement and therefore do not convey any valuable information.

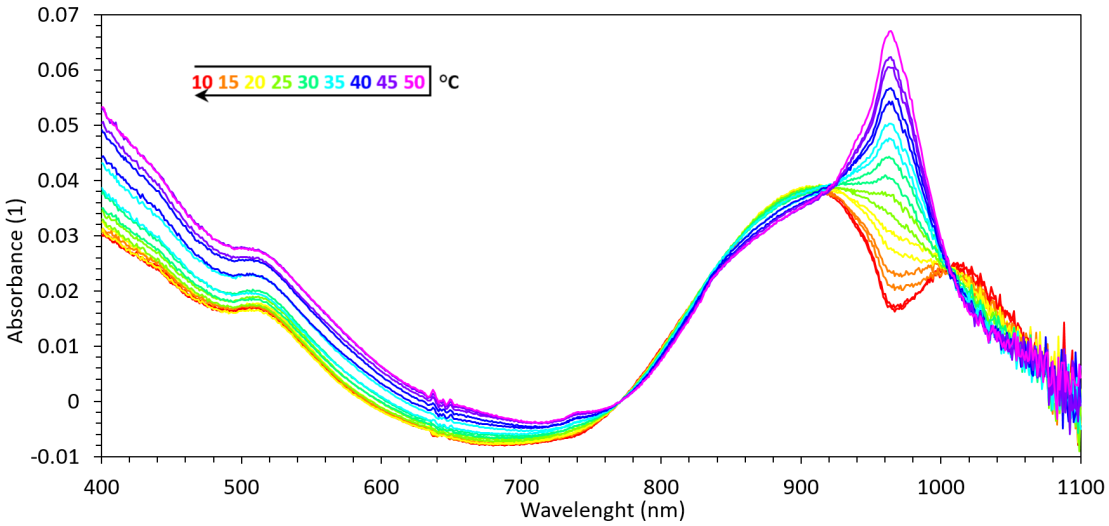

Fig. 38. Absorption spectra of the sandwich at various temperatures of the thermal cycle. The sample is a PEM–hybrid sandwich deposited on a single side of a glass slip, that was prepared by the drying-based method at low temperature. The sample was heated in a stepwise manner from 10°C to 50°C and afterwards cooled back to 10°C while recording a spectrum every 5°C (~ the thermal cycle). The absorbance of the every single spectrum was adjusted by offsetting the spectra in data post-processing to match the zero absorbance at 770 nm wavelength. All spectra are related to the identical blank measurement acquired with a plain glass slip in diH_2O at 23°C as a sample.

The spectra of hybrid–PEM sandwich deposited on a single side of a glass slip acquired during the thermal cycle are presented in Figure 38. The spectra acquired comprise several phenomena. First, the dominant temperature-variable absorption peak, centred at about 965 nm, as well as the diminutive temperature-variable peaks, centred at 740 nm and 840 nm, are present. These absorption peaks arise from the thermal dependence of water absorption as is determined by the control experiment (Figure 37). Noteworthy, the two minor peaks presented in Figure 37 appear substantially greater than the equivalent peaks presented in Figure 38 as was anticipated from the constructive interaction with the fringe pattern.

Second, the absorption spectra of the sandwich (Figure 38) present **no fringe pattern** unlike the spectra of native PEM (Figure 37). The absence of the fringe pattern is most probably a consequence of the presence of hybrids on the PEM surface disrupting the interference on a thin layer but giving rise to the light scattering. The light interference phenomenon could appear on the sandwich as well, when highly

periodically ordered hybrid layer is assembled on a surface (Pacholski 2015; Horigome and Suzuki 2012; Weng et al. 2016). Nevertheless, this phenomenon was not identified in the acquired spectra.

Third, a smaller absorption peak centred at approximately 510 nm and a greater absorption peak centred at approximately 930 nm are present in the acquired spectra (Figure 38). The smaller peak appears as temperature-invariant while the greater peak somewhat transforms in a reversible temperature-associated fashion. It shifts towards higher wavelengths and/or decreases its amplitude with increasing temperature. The absorption peak centred at about 510 nm corresponds to the absorption band of the TSPR and the peak centred at about 930 nm corresponds to the LSPR absorption band of the AuNRs comprised in the hybrids employed (Figure 5/images CD; section 2.2.2). The **shifting of the LSPR band** towards higher wavelengths and/or decrease of its amplitude with increasing temperature cannot be clearly discriminated in the spectra presented due to the presence of a temperature-variable peak of water at 965 nm. It partially overlaps the LSPR absorption band nearby its amplitude and thereby makes the discrimination of the effects ambiguous. Nevertheless, both red-shifting, as well as the reduction of the amplitude of LSPR peak, are consequences of shrinkage of hybrid particles as it is documented in the literature (Karg et al. 2007). This relation is based on increasing plasmon coupling between neighbouring AuNRs attached to the surface of microgels while undergoing the shrinkage.

Fourth, all absorption spectra of Figure 38 comprise an absorption ramp rising towards its blue-end. The steepness of the ramp is positively associated with the temperature of the sample. The ramp probably comprises two major components: **light scattering** on the deposited hybrid particles and absorption of AuNRs deposited on the surface of the microgels (section 3.1). It is documented in the literature, that the suspension of hybrid particles effectively scatters incident light radiation (Karg et al. 2007). The shrunken hybrids are of a higher refractive index than the swollen hybrids, which leads to intensified light scattering and thereby an increased steepness of the absorption ramp recorded.

The spectra of Figure 38 were further evaluated to reveal the relation between the absorbance acquired at 400 nm and the temperature of the sample. The temperature-dependent changes of absorbance in this region can be plausibly attributed to the light scattering on the hybrid particles as discussed in the previous paragraph.

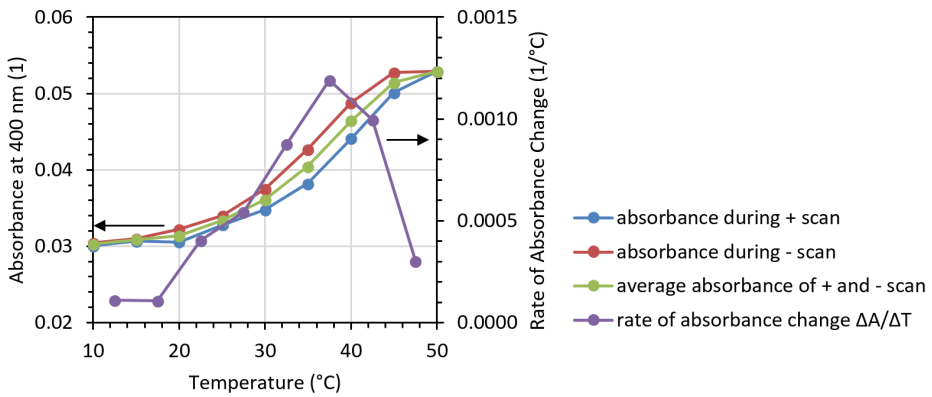

Fig. 39. The absorbance of the sandwich at 400 nm (the left vertical axis) and the rate of absorbance change (the right vertical axis) at various temperatures during the thermal cycle. The rate of absorbance

change is evaluated from the average absorbance of the positive and the negative scan of the thermal cycle. Note, that the data point acquired at 50°C is probably negatively biased by temperature hysteresis at the temperature sweep turning point. The data presented are another representation of the absorbance at 400 nm from Figure 38.

Figure 39 documents, that the light scattering intensity—expressed as the absorbance at 400 nm—is positively associated with temperature. Yet, the association is not linearly proportional throughout the complete temperature interval examined. The rate of absorbance change, plotted in Figure 39 on the right axis, indicates the sensitivity of the scattering intensity to a change of the temperature at various temperatures. The maximal sensitivity is found in the temperature interval of 35–40°C, which corresponds to the temperature of the volume phase transition of the attached hybrids. This finding is in acceptable agreement with the T_{VPT} of plain P(NIPAM-AAA) microgels accounting to 41°C as determined from the temperature development of zeta potential (Figure 5). Hence, the data presented corroborate, that the hybrids attached on the PEM by drying at low temperature preserve their thermoresponsivity. It can be concluded that the hybrids undergo the reversible volume phase transition in a temperature region 35–40°C.

These values of T_{VPT} are higher than the value of T_{VPT} typical for pure PNIPAM (~32°C; section 2.2.1). This shift is expectable since it is known that the presence of a charged group (here: allylacetic acid, AAA) in the PNIPAM-based polymer leads to a positive shift of its T_{VPT} value (Karg et al. 2008; 2009).

4.8.2 Microscopy analysis

As is presented in this section, VPT of the sandwich-deposited hybrids triggered by systemic heating was followed by means of transmission microscopy. A transmission photomicrograph of a hydrated sandwich at room temperature and afterwards at the increased temperature was acquired. The temperature of the sample is not accurately known due to thermal gradients between the atmosphere of the microscopy chamber (that is thermally controlled) and the body of the microscope. The temperature of the sample is estimated at approximately 50°C.

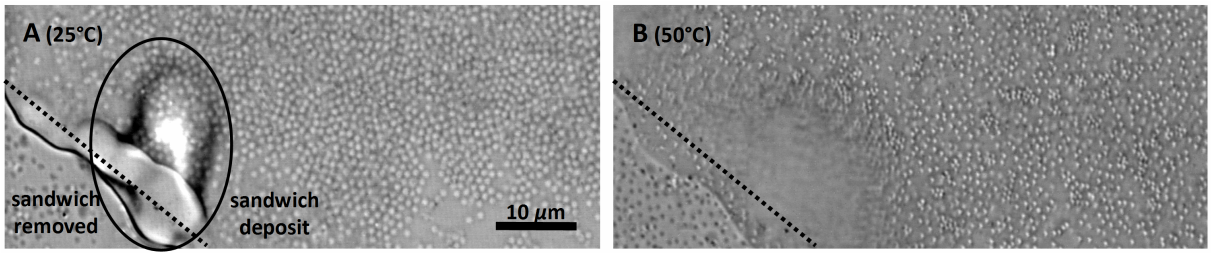

Fig. 40. Monochrome scanning transmission photomicrographs of the sandwich in the buffer environment at 25°C (image A) and 50°C (image B) approximately. The images correspond to the same area of the sample. Image B was acquired about 3.5 hours after image A while the system was gradually heated. The left bottom corner of the images depicts a reference zone where the sandwich is deliberately removed. The black oval indicates the position of a PEM shaving, that emerges when the PEM is peeled off from the reference zone and afterwards it lands on the area adjacent to the reference zone. The object plane of the objective crosses the sample in the z-position of the PEM.

Figure 40 presents photomicrographs, that visualize the basal layer of the hybrids deposited on the PEM surface. At room temperature (image A), the hybrids are periodically ordered in closely packed areas, or random-distributed in more loosely packed areas. Some sparse areas of the sample are not covered with hybrids. The lattice constant evaluated in the periodically ordered areas of the deposit at room temperature accounts to about 1.0 μm (evaluated as the average distance between 18 closely positioned hybrids in the periodically ordered regions of the basal layer of the deposit displayed in image A of Figure 40). At the elevated temperature of about 50°C (image B), the periodic order of the hybrids is lost while most of the PEM is covered with rather random-distributed hybrid particles. Importantly, the hybrids remain attached to the PEM surface during the 3.5-hour lasting process of increasing the temperature up to about 50°C. However, position of single hybrids on the PEM surface gradually changes during this time, which can be explained by the viscous-fluid nature of the PEM. Please note that the hybrids deposited on the PEM are visualised as bright objects while the hybrids, that landed in the scratched region, are visualized as dark objects due to their different *z*-position relatively to the object plane as discussed in section 4.5. Lastly, image A documents a PEM shaving (reminiscent of a wood shaving; indicated by the black oval in Figure 40) located at the border between the zone presenting the sandwich and the reference zone with the sandwich removed. The PEM shaving was created unintentionally when peeling off the sandwich from the reference zone while adhering to the periphery of this zone. The shaving afterwards lands on the area adjacent to the zone of the removed sandwich. This shaving, that resides on the sandwich surface, gradually fuses with the underlying PEM. This fusion still proceeds even about 3.5 hours after the creation of the shaving (image B). This process documents the viscous-fluid quality of the HA/PLL PEM.

The periodic order of the hybrids at room temperature indicates the close packing of the hybrids. This inference is corroborated by the lattice constant evaluated, that is very similar to the lattice constants of other conclusively closely packed deposits at equivalent conditions (figures 21, 24, 27). Further, **the loss of the periodic order** after the temperature increase indicates, that the deposited hybrids gained more spatial freedom, which is most probably a consequence of the thermally-triggered shrinking of hybrids. This conclusion is supported by the visual estimation of particle size, that reduced by a factor of two after to the temperature increase. Nevertheless, the size of particles, as visualized by transmission microscopy, serves only as a hint for estimation of the particle size, as it is discussed in section 4.5.

More accurate values of the hybrid **particle size** were obtained by aggregating the results of all repetitions of this experiment. Based on these results, it can be concluded that increasing the temperature of the sandwich from room temperature to about 50°C induces the deposited hybrids to shrink from about 1.02 μm diameter (n = 110) to 0.56 μm (n = 79) diameter (the particle diameter was evaluated as the lattice constant in the conclusively closely packed regions). Further, these values can be compared with the values of hydrodynamic diameter of unmodified microgels: about 1.5 μm at 20°C and about 0.5 μm at 45°C (Figure 5, image A). While the size of the shrunken hybrid particle and the shrunken microgel particle does not differ any substantially, the size of the swollen hybrid particle (evaluated from the lattice constant) is substantially lower than the size of the swollen microgel particle (determined by DLS). This difference in the particle size can be explained by several phenomena: i)

partial shrinking of microgels during their modification by AuNRs, ii) partial shrinking of microgels following the interaction of hybrids with PLL released from the PEM, iii) partial overlapping of the hairy exterior of hybrids when closely packed on the PEM surface. Regardless of the actual cause, this discrepancy imply that the hydrodynamic radii of the swollen microgel cannot be employed as a reference value for the size of hybrids in the deposit.

Finally, the **thickness of the PEM** in a sandwich was evaluated from the *z*-stack photomicrographs acquired during the gradual systemic heating. The acquired data indicate, that there is no substantial change of the PEM thickness during heating of the sandwich from RT to about 50°C (data not presented). However, due to the *z*-sectioning interval of the data acquired, changes of the PEM thickness smaller than about 0.5 μm are not probably discerned.

4.9 Loading of macromolecules into sandwich

The work presented aims on controlling the molecular transport between the HA/PLL PEM and its water-based environment. Several cornerstones of this goal were laid and presented in the previous sections. First, a method of sandwich preparation was developed with the aim to achieve a gating of molecular transport by the layer of the hybrids deposited on-top of the PEM (section 4.6). Drying of hybrid suspension on the PEM surface at low temperature is identified as the optimal method for this purpose (section 4.6.4). Second, the sandwiches prepared by various methods were tested for their susceptibility to irradiation by IR laser light (section 4.7). The sandwiches prepared by drying-based methods comprise hybrid particles that are capable of the volume phase transition in a reversible manner when triggered by the laser irradiation. The thermal responsivity of the hybrids was further examined by the systemic heating of the sandwich while following the temperature-dependent changes by spectroscopy and microscopy techniques (section 4.8). The ability of the hybrids incorporated in the sandwich to undergo the volume phase transition triggered by temperature change is hereby confirmed.

In this section, the ability of the deposited layer of hybrids to control the molecular transport of a model molecule from solution into the PEM of a sandwich is examined. Various model molecules are assessed and the optimal molecule for the purpose is selected. An ideal model molecule should not alter the qualities of the sandwich, it readily loads into the PEM in high quantities and it cannot permeate through the closed gate formed by the hybrid deposit.

Practically, the *loading experiment* is performed by exchanging the buffer environment of the hydrated sandwich for the buffer solution of the molecule tested followed by incubation at the unmixed condition. The molecular uptake and possible concomitant changes of the sample are followed by means of photomicroscopy in transmission and fluorescence mode. The incubation is usually allowed to proceed for half an hour, followed by replacement of the loading solution for a washing buffer (*the release experiment*).

4.9.1 PLL-FITC

PLL can be readily loaded from its solution into the HA/PLL PEM similarly, as it occurs during the PEM build-up process (section 2.2.3). Introduction of FITC-labelled PLL into the sandwich is assumed to alter the qualities of the sandwich in a minimal way since the PLL is a building block of the PEM as well as a glue of the sandwich (section 4.6.1). The photomicrographs acquired during the loading experiment are displayed in Figure 41.

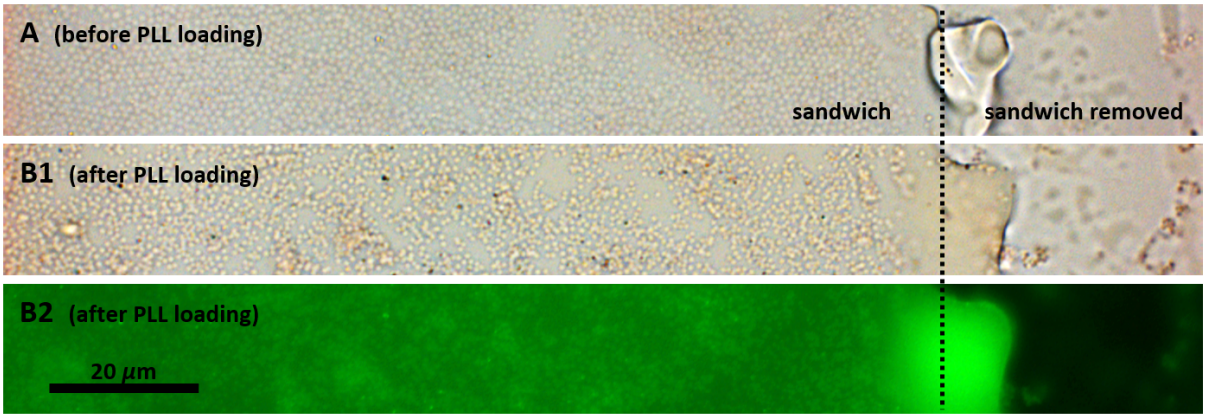

Fig. 41. Colour transmission (images A, B1) and monochrome epifluorescence (image B2) photomicrographs of a hydrated sandwich before (image A) and after (images B1, B2) 15 min of incubation with 0.5 mg/mL buffer solution of PLL-FITC at RT. The right side of the images displays an area where the sandwich is deliberately removed (the scratched region). The images correspond to the identical area of the sample. The object plane of the objective passes the sample in the z-position of PEM. Thereby, the basal layer of the deposit on the PEM surface is effectively visualised in the transmission mode. Images were acquired at RT. The sandwich was prepared as described in section 4.6.2.

Image A of Figure 41 documents the condition of the sandwich before the incubation with the PLL-FITC solution. The sandwich resembles a typical form of a sandwich prepared by drying-based procedure performed at low temperature followed by rehydration (section 4.6.4). Most of the PEM surface is covered by the hybrids. The hybrids deposit predominantly in one or two layers on the PEM surface (the full *z*-stack indicating this aspect is not presented here). The hybrids arrange in some areas in a periodic manner while in other areas are rather random-distributed. A minor proportion of the PEM is completely uncovered by hybrids. The bright object appearing at the border between the sandwich area and the scratched region (image A) is a PEM shaving unintentionally formed during the removal of the sandwich in the scratched region as was discussed in section 4.8.2. Image B of Figure 41 documents the state of the sandwich after the incubation with PLL-FITC solution for 15 minutes. The hybrids of the deposit lost their periodic order in comparison to the situation before the incubation. Further, the PEM shaving became outspread. Image B2 (fluorescence mode equivalent of image B1) documents a fluorescence signal originating in PEM (mostly pronounced in the region of the shaving, presenting a thick PEM layer) and in the deposited hybrids as well.

The procedural and the visual equivalency to the sandwiches prepared by drying-based procedure at low-temperature (sections 4.6.4 and 4.7.1) intimates that the hybrids of the sandwich before incubation (image A of Figure 41) are in swollen state and the periodically ordered areas of the deposit are closely

packed. The periodic order of hybrids is fully lost during the incubation with the PLL-FITC solution (image B). This indicates that the close packing of hybrids is lost as well. The probable cause of this transformation is an attractive interaction of positively charged PLL-FITC molecules with negatively charged microgels (copolymer of allylacetic acid) resulting in charge compensation and non-thermal shrinkage of the hybrids—the **PLL-triggered shrinking of hybrids.** This explanation is further supported by several other observations. First, a prominent fluorescence is localised inside the hybrids after incubation with PLL-FITC (image B1) indicating an increased concentration of PLL-FITC inside the hybrids. This means that molecules of PLL penetrate not only PEM during incubation but hybrids as well. Second, the PLL-triggered shrinking of hybrids was already discussed in sections 4.6.3 and 4.7.2 as a plausible explanation of the non-thermal hybrid shrinking described there.

It can be summarized, that a few aspects playing a crucial role in the applicability of PLL as the model molecule were revealed. The PLL presented in the loading solution triggers the non-thermal shrinking of hybrids during a course of not more than several minutes, which substantially reduces the size of the hybrids. The ability of such hybrids to shrink upon IR laser irradiation is thereby eliminated as it is documented in section 4.7.2. Although these effects rule out the applicability of PLL as a model molecule, several loading experiments following the time development of fluorescence signal inside the PEM of the sandwich were performed. The results acquired do not present any substantial difference in loading kinetics of the PLL-FITC into the sandwich and into the control plain PEM (data not presented). Based on the findings collected, it can be concluded that PLL is not applicable as a model molecule for the gating properties of the deposit.

4.9.2 Dextran-FITC

Dextran is a promising candidate as a model molecule for loading experiments since it is not charged, variable molecular masses are available, and it is a widespread substance of numerous applications in biotechnology, medicine, or surface chemistry. Three different molecular masses (70, 10, 4 kDa) of dextran-FITC were tested under various test conditions. Notably, some experiments employed the *native PEM* (the PEM resulting from the layer-by-layer preparation procedure and stored at hydrated conditions) while other experiments employed the *plain PEM* (the PEM obtained by drying the native PEM followed by rehydration—an equivalent procedure to sandwich preparation drying based method as described in section 4.6.4). The fluorescence photomicrographs presented in this section were acquired in the confocal mode. This mode can effectively discriminate the fluorescence signal originating from different *z*-positions and thereby it provides more detailed information on the system than the epifluorescence mode.

The loading experiments employing **70 kDa dextran** indicate, that molecules of dextran-FITC of 70 kDa molecular mass gradually penetrate only about 2 μm deep into about 4 μm thick native PEM during an hour lasting loading experiment (data not presented). This observation indicates, that mobility of 70 kDa dextran in the native PEM significantly limits the applicability for loading and release experiments.

Afterwards, **10 kDa dextran** was employed for the loading experiment. Its molecules are smaller than the molecules of the 70 kDa dextran and therefore it is assumed to be more mobile in the PEM. The loading experiments were performed with the native as well as the plain PEM.

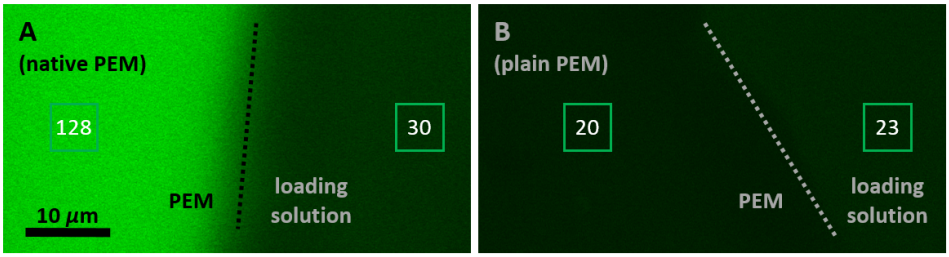

Fig. 42. Confocal fluorescence photomicrographs of the PEM after half an hour of loading with dextran-FITC of 10 kDa molecular mass (0.125 mg/mL solution in buffer). The native PEM (image A), as well as the plain PEM (image B), were employed. The fluorescence signal is collected from an optical slice about 2 μm thick, crossing the z-position of the PEM. The right side of both images depicts a reference zone where the PEM is deliberately removed (the scratched region) and thereby it is filled with the loading solution. The green boxes indicate average fluorescence intensity in the area.

The photomicrographs acquired after half an hour lasting loading the PEM with 10 kDa dextran are displayed in Figure 42. The loading solution is still present and the intensity of fluorescence can be inferred from the region of the removed sandwich. Image A documents a relatively high intensity of the fluorescence signal in the native PEM (~ 128)—about 4.3-times higher than the intensity of the signal in the dextran solution (~ 30). Image B documents rather weak fluorescence signal in the plain PEM (~ 20)—about 0.9-times the intensity of the signal in the dextran solution (~ 23). It can be approximated, that the intensity of fluorescence is proportional to the dextran concentration in the environments considered. The rate of loading the 10 kDa dextran into the native or the plain PEM is equivalent at the onset of the loading. However, the loading of native PEM proceeds for about 20 minutes until an apparent equilibrium is reached while the loading of plain PEM reaches the equilibrium already after about a minute (data not presented).

The fluorescence intensity in various z-positions of the PEM (both the native and the plain) during loading with 10 kDa dextran presents no substantial trend. It indicates that the **mobility of 10 kDa dextran in the PEM** at the onset of loading is significantly higher than the mobility of 70 kDa dextran. Therefore, the loading of 10 kDa dextran is not substantially limited by gradual penetration through the PEM as observed with 70 kDa dextran. This observation corroborates the anticipated negative correlation between the molecular size of the dextran and its molecular mobility inside the PEM.

Further, the data presented in Figure 42 indicate that loading of 10 kDa dextran into **the native and the plain PEM** proceeds differently. The partition constant of the dextran for the native PEM is about 5-time higher than the constant for the plain PEM. This difference can be possibly explained in the light of the transformation of the native PEM to the plain PEM by drying. The typical thickness of the native PEM employed here is about 4 μm, of the dry PEM is less than 0.5 μm and of the plain PEM is 2.5 μm in average (section 3.9). The thickness of the native PEM is about double the thickness of the plain PEM obtained by drying followed by rehydration. This reduction of thickness can be rationalised as follows.

As the native PEM dries up, hydration water is removed and the system rearranges into a more compact state with intrinsic charge compensation between oppositely charged polyelectrolytes. The positively and the negatively charged polyelectrolytes become more interconnected. Afterwards, when the dry PEM is rehydrated, the state of the PEM does not recover completely while it partially attains the compact structure with less available binding sites/free space for the dextran molecules in comparison to the state before the drying. This mechanism can explain the reduced thickness of the plain PEM as well as the reduced partition constant of the dextran in the plain PEM in comparison to the native PEM. The kinetics of the loading remains uninfluenced probably since it is limited by the molecular mass of the dextran under the conditions employed.

The value of the partition constant obtained when the sandwich is loaded with 10 kDa dextran is equivalent to the value obtained when the plain PEM is loaded (data not presented). Such unfavourable partitioning makes the data collection challenging and it does not reflect the objective of the work. Therefore, 10 kDa dextran is not considered a suitable test molecule.

Finally, **4 kDa dextran** was examined for its applicability as the test molecule. The loading experiments were performed with the sandwich or the plain PEM as a control sample at room temperature of about 25°C or at a systemically elevated temperature of about 50°C.

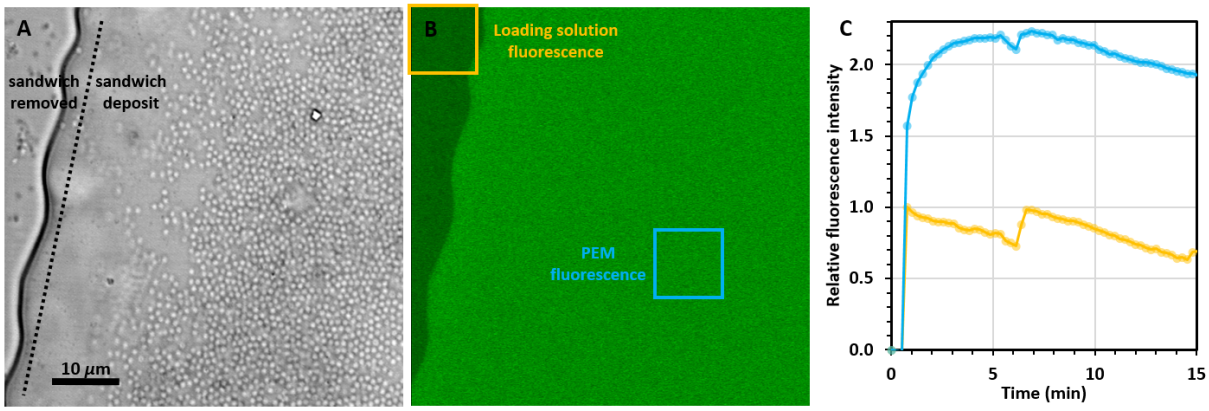

*Fig. 43. Loading of the sandwich with dextran-FITC of 4 kDa molecular mass. **A**: monochrome transmission photomicrograph of the sandwich in the buffer environment before loading. The object plane of the objective is crossing the z-position of the PEM surface. Thereby, the basal deposit of the hybrids on the PEM surface is effectively visualized. **B**: Confocal fluorescence photomicrograph of the sandwich in the loading solution at the time point of two minutes after the start of loading. The fluorescence signal is collected from an optical slice about 2 µm thick, crossing the z-position of the PEM. The colour-coded squares indicate the areas employed for evaluation of fluorescence intensity displayed in plot C. Images A and B correspond to the identical area of the sample. The zone of removed sandwich (the scratched region), that serves as a reference, is located on the left side of the images. **C**: Time development of fluorescence intensity in the loading solution of 4 kDa dextran (yellow data line) and in the PEM (blue data line) during the loading experiment. The data are corrected for detector offset and normalized to the fluorescence intensity of the loading solution at the onset of loading. The data displayed are evaluated from a maximum-value z-stack overlay in order to limit the influence of the focus drifting on the fluorescence intensity evaluated from the PEM. The efficacy of this measure on correcting the data of fluorescence intensity in the solution is limited since the focus drifting influences the z-depth of the solution included in the acquired data. Thereby, the gradual decrease of the yellow data line is caused mainly by the focus drifting. The gradual decrease of the blue data line is caused mainly by photobleaching. The repetition time of image acquisition is 15 s. The loading experiment was performed at room temperature of about 25°C.*

Figure 43 presents the data acquired during the loading of the sandwich with 4 kDa dextran at room temperature. Image A documents the presence of a deposited layer formed by closely packed hybrids on most of the PEM surface with some uncoated regions. The packing density of the hybrids deposited is markedly reduced in the vicinity of the scratched region due to mechanical stress arising during sandwich removal from the scratched region. Image B—acquired two minutes after the onset of the loading—documents substantially increased fluorescence intensity in the PEM relative to the fluorescence intensity of the loading solution. The fluorescence intensity is uniformly distributed in the *xy* plane of the PEM—there is no spatial correlation with the presence of the deposit on the PEM. Plot C of Figure 43 documents the kinetics of loading of 4 kDa dextran: a rapid loading at the onset gradually levels off until a maximum is reached about 5 minutes after the onset of the loading. Finally, after reaching its maximum, the fluorescence intensity in PEM starts to gradually decrease probably due to photobleaching.

The deposited layer of closely packed hybrids is disrupted by sparse regions of missing hybrid particles (image A of Figure 43). Since these uncovered regions are documented together with the regular deposit-covered regions within one image, it can serve as a control area during the loading experiment. Thereby, it was determined, that none of the photomicrographs acquired during the loading experiment presents substantially different fluorescence intensity in the region uncovered in comparison to the regions covered. This indicates that **the gating ability** (the reduction of the rate of loading) of the deposit towards 4 kDa dextran is less significant than the rate of dextran diffusion inside the HA/PLL PEM that smears the difference between covered and uncovered areas. It can be summarized, that on the temporal scale from 15 seconds (the repetition rate of the data acquisition) to tens of minutes and on the spatial scale from units to tens of micrometers, there is no substantial influence of the presence of the deposited hybrid layer recognisable.

Importantly, when the loading is performed with the plain PEM instead of the sandwich, at 50°C instead of 25°C, or a combination of both—with the plain PEM at 50°C, the results obtained are equivalent to those presented in Figure 43. The loading experiments were repeated several times with equivalent results. From the data acquired, it can be concluded that there is no substantial correlation between **the rate of dextran loading and various conditions** of the experiments performed (presence/absence of the deposit of hybrids; 25°C/50°C).

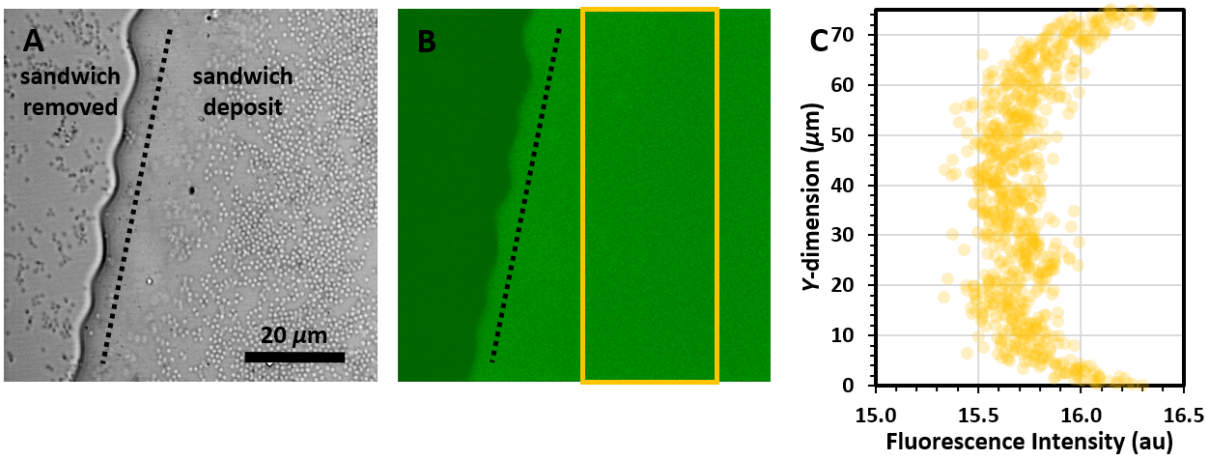

Fig. 44. The sandwich loaded with dextran-FITC of 4 kDa molecular mass in the buffer medium. ***Image A****: monochrome transmission mode. The object plane of the objective is crossing the z-position of the PEM surface and thereby effectively visualizing the basal deposit of the hybrids on the PEM surface.* ***Image B****: confocal fluorescence mode. The fluorescence signal is collected from an optical slice about 2 μm thick, crossing the middle of the PEM. Image B was acquired during the time interval 5.0–7.4 s after the start of the z-stack acquisition as a third image of the z-stack. In image B, the yellow rectangle denotes the area employed for evaluation of the fluorescence intensity profile depicted in* ***plot C****. The data in the region denoted by the yellow rectangle are averaged over the horizontal dimension resulting in a one-dimensional fluorescence intensity profile presented in plot C. Bleaching, accompanying the data acquisition, reduces the fluorescence intensity in the PEM and gives rise to a diffusional recovery. The data presented were acquired a few minutes after the exchange of the dextran loading solution for the washing buffer. Images A and B correspond to the identical area of the sample. The sample employed here is the same as the sample of Figure 43. A reference area of deliberately removed sandwich (the scratched region) filled by buffer is present on the left side of the photomicrographs.*

Figure 44 documents a phenomenon, that plausibly arises from the **diffusion of dextran in the PEM**. Plot C indicates a presence of a spatial gradient of fluorescence intensity rising towards an edge of the area scanned. This gradient is rather faint in comparison to the noise of the signal and therefore it is not directly observable in the image B. This gradient is probably caused by photobleaching of FITC arising from the repeated scanning of a well-defined area by the laser of CLSM during the *z*-stack acquisition. Outside the scanned area, the fluorophore remains rather unbleached. Molecular diffusion enables intermixing of the bleached and the unbleached dextran-FITC, which manifests as a recovery profile along the edge of the scanned area. The rate of diffusion of 4 kDa dextran in the PEM can be estimated from the recovery profiles acquired during various stages of repeated loading experiments. The estimate is based on the time of continuous scanning of the area (usually about 10 s) and the extent of the recovery approximated as a distance from the edge of the scanned area that was influenced by the diffusional recovery (usually about 5–20 μm). The estimate of the diffusion rate of 4 kDa dextran in the PEM usually falls into a range from units to tens of $\mu m^2/s$.

The **partition constant** of 4 kDa dextran, that describes its partitioning between the PEM and the loading solution, was found to be 2.4 ± 0.6 ($x \pm s$, n = 11). The evaluation is based on the fluorescence intensity of the loading solution and the PEM, determined about 25 minutes after the start of loading—sufficiently long after reaching the apparent loading equilibrium. The value of the constant does not present any obvious correlation with the temperature of the system or other considered parameters such

as fluorescence intensity in the solution, fluorescence intensity in the PEM, the batch of the PEM, or thickness of the PEM. However, it may negatively correlate with the presence of the hybrid deposit on the PEM surface. In order to clarify this association, more data needs to be collected.

Noteworthy, after half an hour lasting incubation of the sandwich in the solution of dextran-FITC of 4 kDa molecular mass, the **fluorescence signal originating from the interior of the hybrids** is lower than that of the loading solution if any at all (data not presented). This indicates, that 4 kDa dextran do not load into the interior of the hybrids in any major quantity under the conditions given. This conclusion is consistent with the concept of hybrid deposit acting as a barrier to the molecular transport. Nevertheless, this aspect is necessary but not sufficient condition of achieving the effective barrier property.

Two parallel phenomena occur after the exchange of the loading solution for the buffer with intermediate washout by the buffer: i) gradual reduction of the fluorescence intensity in the PEM and ii) increase of the fluorescence intensity in the buffer shortly after replacing the loading solution by the buffer (data not presented). The phenomena indicate, that the dextran, once loaded into the PEM of the sandwich, **spontaneously releases** after the exchange of the loading solution for buffer. The release reduces the amount of 4 kDa dextran in the PEM approximately no more than by a few folds per an hour of the passive washing. This estimation is based on a rather singular observation that enabled to assess the temporal development of fluorescence intensity in the PEM during the passive washing without prominent photobleaching.

Photobleaching reduces the fluorescence intensity acquired during imaging much more rapidly than the release of dextran-FITC during the passive washing—approximately 100-fold faster. The actual rate of photobleaching depends on the imaging method employed and its settings. However, the effect of the photobleaching is rather spatiotemporally confined unlike the effect of the spontaneous dextran release. This difference allows to distinguish them from each other.

The **changes in the PEM thickness**, that may accompany the loading with 4 kDa dextran and the following washing, were evaluated. The PEM of the sandwich and the plain PEM were assessed. From the statistical evaluation of all applicable results, it can be concluded, that none of the cases mentioned leads to a substantial change of the PEM thickness. This finding indicates, that the loading or the releasing of the dextran is not accompanied by any substantial changes of molecular interactions, that stabilize the PEM structure.

The results discussed in this section can be summarized in the following points. The dextran-FITC of 4 kDa molecular mass loads into the PEM of the sandwich in a substantial amount with relatively fast kinetics. The diffusion of the dextran in the PEM is fast enough not to limit the loading process. The presence of dextran causes no adverse changes to the sandwich as well as its functionality (Figure 44). Therefore, the 4 kDa dextran is considered a good test molecule for further loading and release experiments. Yet, no correlation between the presence of the hybrid deposit on the PEM and kinetics of loading, as well as between the state of the deposit (swollen/shrunken hybrids) and kinetics of loading, was found. It indicates that the hybrid deposit is too permeable to engender a rate-determining step of the molecular transport during the loading, and thereby it is not able to effectively steer the rate of the

transport.

4.10 IR laser influence on dextran loaded sandwich

The objective of the work presented in this chapter is a control over release kinetics of a test molecule—4 kDa dextran—by controlling the swelling state of the hybrids deposited on the surface of the molecular reservoir. The laser irradiation of the hybrids, employed for that purpose, leads to the local heating which influences the local characteristics of the system (section 4.7). Various phenomena accompanying this process are presented and discussed in this chapter.

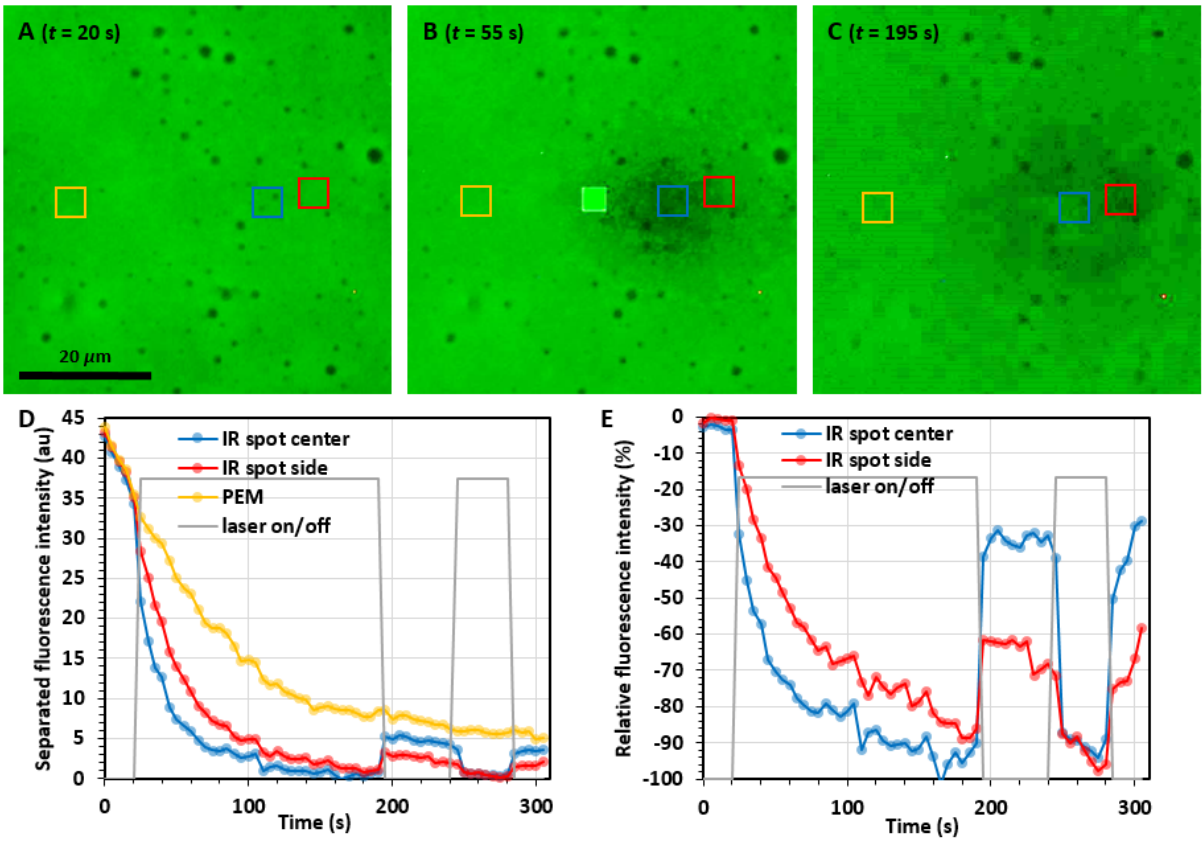

Fig. 45. Temporal development of the fluorescence intensity in the dextran-FITC of molecular mass of 4 kDa -loaded PEM of the sandwich in the buffer environment under discontinuous IR laser irradiation. Images ***A–C****: epifluorescence photomicrographs of the sandwich at the time point 20 s (A), 55 s (B), and 195 s (C) after the onset of the time-lapse acquisition (time = 0 s). The full green square in the centre of image B informs about the activity of the IR laser—it does not convey any image information. The irradiated spot is centred about 10 μm in the right-direction from the green square. The irradiation is performed with a defocused laser of 50% power. Contrast and brightness of the micrographs are adjusted independently in order to correct for photobleaching. The time-lapse acquisition was triggered about 40 minutes after the end of loading (i.e. the start of the active phase of washing).* ***D****: plot of the temporal development of the fluorescence intensity in the centre of the irradiated spot (the blue data line), on the side of the irradiated spot (the red data line), and out of the irradiated spot (the yellow data line). The fluorescence intensity in the solution was evaluated as well, the data acquired were smoothed by a 5-point stencil and subtracted from the fluorescence intensity data resulting in the 'Separated fluorescence intensity' plotted in image D. The position of the data origin is marked in images A–C by the colour-coded rectangles.* ***E****: plot of the temporal development of the relative fluorescence intensity. The data presented are obtained from the data*

of plot D by relating the values of fluorescence intensity in the irradiated zone to the values of the fluorescence intensity outside the irradiated zone. The relation is calculated as: (blue – yellow) / (yellow – solution) data lines of the plot D to obtain relative fluorescence intensity in the centre of the irradiated spot and (red – yellow) / (yellow – solution) data lines of the plot D to obtain relative fluorescence intensity on the side of the irradiated spot.

The effects of the laser irradiation on the fluorescence intensity in the sandwich loaded with dextran-FITC are documented in Figure 45. The sandwich is incubated in the buffer under no-flow condition (the passive phase of the release experiment) while the time-lapse acquisition of epifluorescence photomicrographs proceeds. Images A, B, and C present selected photomicrographs, that document the spatial distribution of the fluorescence in the PEM at various stages of the experiment. A chosen region of the sandwich (near the centre of the image) is irradiated by a defocused IR laser with an intermediate interval without irradiation—as it is indicated by the grey data line in the plots of the figure. The temporal development of fluorescence intensity in three characteristic regions of the sandwich was evaluated from the set of acquired time-lapse photomicrographs (plots D and E).

One of the prominent effects following the laser irradiation is the gradual reduction of the fluorescence intensity in the area irradiated by the laser (hereinafter referred to as *the fluorescence drop*). Spatially, **the fluorescence drop** has a smooth gradient towards the centre of the irradiated area, as it is indicated by image B of Figure 45. Temporal development of the fluorescence intensity in the fluorescence drop is indicated by the blue and the red data lines of plot D and E during the first laser irradiation (time interval 20–190 s). The fluorescence intensity gradually decreases until it disappears almost completely after a few minutes of continuous laser irradiation. The fluorescence drop develops faster in the centre of the irradiated region than on the periphery of the irradiated region as can be inferred from the comparison between the blue and the red data line.

Upon deactivation of the laser, the fluorescence drop remains first unchanged. The area of the fluorescence drop gradually expands and smears by the time as it can be concluded from a comparison of the area 1.5 min after the deactivation of the laser (Figure 46) to the area immediately after the deactivation of the laser (Figure 45, image C). This phenomenon is plausibly caused by the diffusion of dextran in the PEM, which is discussed in section 4.9.2.

The presence of the fluorescence drop may be explained by one or more of the following effects:

[a] The gating ability of the deposit of hybrids. An accelerated molecular transport is assumed in the area of a sandwich, where the microgels deposited are shrunken or missing. Nevertheless, this effect is documented to have very limited influence if any at all under the conditions employed, as it is concluded in section 4.9.2.

[b] Change of physico-chemical properties of the PEM due to the increased temperature. Dextran may be spontaneously released from the PEM of the sandwich into the surrounding solution, as it is discussed in section 4.9.2. The increased temperature may elevate the kinetics of this process.

[c] Intensified photobleaching in the region heated. Photobleaching is a major effect responsible for the reduction of fluorescence intensity during data acquisition as it is discussed in section 4.9.2, Figure 44. Photobleaching of FITC is known to proceed with a complex system of reactions (Song et al. 1995; 1996).

Rate of chemical reactions is classically dependent on the temperature (Elibol et al. 2009; Le Gros et al. 2009).

[d] Temperature dependence of fluorescence quantum yield. This effect is a general attribute of molecular fluorophores and therefore it is assumed to affect the region heated by the IR irradiation (Liu et al. 2005). Separate estimation of the magnitude of this effect indicates, that the quantum yield reduction in the area irradiated accounts for the reduction of the fluorescence signal by no more than 20% (data not presented) while the fluorescence drop discussed reaches up to nearly 100% reduction of the fluorescence intensity (Figure 45). Moreover, the quantum yield reduction is assumed to act without lag to any temperature changes. Since the temperature increase in the heated region is rapid, as it is indicated by the rate and extent of hybrid shrinking when the laser goes on (section 4.7.1), this effect can explain a minor proportion of a rather gradual reduction of the fluorescence intensity at most. Therefore it can be concluded that this effect plausibly contributes to the fluorescence drop. However, the magnitude of this effect is relatively minor.

[e] Thermophoresis. This process transports molecules along or against a thermal gradient. The direction and the rate of the transport are described by sign and magnitude of the Soret coefficient, that varies, except others, with the temperature and the molecular mass of the molecules transported. Polysaccharides in their solution are known to experience the thermophoresis (Kishikawa et al. 2012; Sugaya, Wolf, and Kita 2006). Since thermophoresis is a mechanism that induces molecular transport, it reduces the concentration of the molecule transported at one place while increases its concentration at another place. This could be possibly observed as a redistribution of the fluorescence intensity in the PEM, when the dextran-FITC is transported. An increase of the fluorescence intensity above the intensity of surrounding in the area around the irradiated zone was actually registered in only one experiment of all performed (data not presented). Nevertheless, this experiment was not exceptional by any of the controlled parameters. This may indicate that the magnitude of the thermophoresis of 4 kDa dextran in the PEM is usually insignificant while being masked by another effect such as diffusion of the dextran, the release of the dextran, or solution streaming in the irradiated area.

Another notable effect of the laser irradiation is the fluorescence intensity increase in the centre of the irradiated area of the dextran-loaded sandwich after the laser goes off (hereinafter referred to as *the central increase of fluorescence intensity*). The photomicrograph documenting **the central increase of fluorescence intensity** is displayed in image C of Figure 45. The fluorescence drop, documented by image B, is still present after the laser irradiation (image C). However, it is extending over a greater area of the sandwich. At the same time, a region of increased fluorescence intensity is documented in the centre of the area previously irradiated by the laser and now presenting the fluorescence drop. The temporal development of the fluorescence intensity in the centre and on the side of the irradiated spot is documented by plot D and E. The central increase gradually appears within a few seconds after the laser is deactivated (the time points 195 s and 285 s) and it remains undiminished for at least 40 s (image E, blue data line, time interval 195–240 s). After the laser is reactivated, the central increase swiftly disappears. The fluorescence intensity substantially increases in the central region of the previously irradiated area (image E, blue data line), while the increase is much weaker on the side of the region

(image E, red data line). Accordingly, it can be concluded that the increase takes place in the central region of the irradiated area predominantly. Therefore the effect is referred to as the *central* increase of the fluorescence intensity.

Based on the results obtained from the repetitions of this experiment, it can be generalised that the central increase of fluorescence intensity develops within a variable time interval starting at the end of the irradiation: on the scale from a few seconds (as documented in Figure 45) to minutes or even more (data not presented). Once the effect is present, it remains relatively undiminished for at least an hour when the sample is left undisturbed. In most cases, there is a good spatial correlation between the presence of this effect and the presence of a PEM region transformed by the thermally-induced swelling of the PEM (section 4.7.3). This correlation is documented by Figure 46.

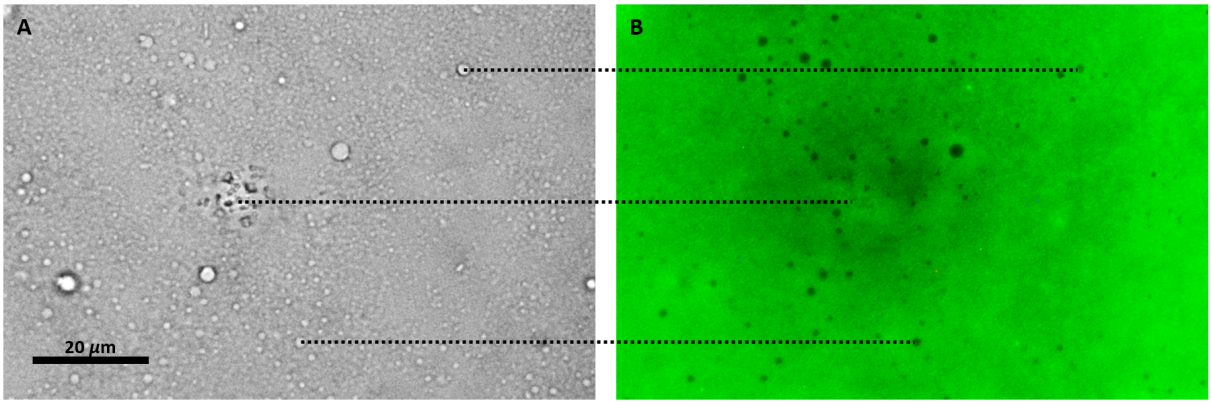

Fig. 46. Monochrome transmission (image A) and epifluorescence (image B) photomicrographs of the sandwich loaded with dextran-FITC of molecular mass of 4 kDa after the IR laser irradiation (the laser is deactivated). The micrographs were acquired 42 s after each other, 48 min after an exchange of the dextran loading solution for the buffer, 1.5 min after deactivation of the laser. A defocused laser of 50% power irradiated the area of the sandwich for 3.5 min in total. The dashed horizontal lines are of identical length and indicate corresponding positions on images A and B. The top and the bottom line serve as a reference gauge, that points out some random-chosen features, while the middle line indicates the centre of the irradiated area. This is the identical area of the same sample as depicted in Figure 45.

The figure depicts the state of a sandwich loaded with dextran-FITC of 4 kDa molecular mass after 3.5 min of irradiation by the NIR laser during the release experiment. Image A documents a presence of a region morphologically transformed by the thermally-induced PEM swelling (section 4.7.3) that is located in the centre of the area previously irradiated by the laser (denoted by the middle dashed line). Image B documents the identical region of the sample in an epifluorescence mode. The fluorescence intensity surrounding the irradiated area is reduced due to the fluorescence drop phenomenon, which is discussed at the beginning of this section.

By comparing the image A and B of Figure 46, it can be concluded that the area transformed by the thermally-induced PEM swelling spatially correlates with the area presenting the central increase of fluorescence intensity. This correlation is probably a consequence of increased PEM thickness in the swelled region (section 4.7.3) leading to an increased amount of the dextran loaded per unit area of the PEM. It is not possible to determine whether an amount of the dextran loaded per unit volume of the swelled PEM (the concentration) is altered as well since the photomicrographs were acquired in the

epifluorescence mode, which collects the fluorescence signal from the entire field depth.

The central increase of fluorescence intensity develops within a **variable interval of time** starting at the moment of deactivation of the laser, as it is described above in this section. However, the morphological transformation, that arises from the heat-induced swelling of the PEM and causes the central increase phenomenon, develops nearly instantaneously after the deactivation of the laser (section 4.7.3). Therefore, there must be another effect, that causes the central increase to develop gradually. This gradual development can be possibly explained by the gradual replenishing of the dextran-FITC in the previously irradiated area. The PEM, as well as the incubation medium, that surround the area, plausibly serve as a source of dextran-FITC for this replenishment. In this regard, the variable rate of the development observed can be explained by a poorly controlled concentration of dextran-FITC in the surrounding since the passive phase of the release experiment is performed in unmixed conditions and the convection of the medium (section 4.7.1) is absent after the deactivation of the laser.

An overview of the phenomena, that manifest themselves by changes of fluorescence intensity, induced by the laser irradiation of the dextran-FITC loaded sandwich in the buffer shortly after the deactivation of laser is depicted by the scheme of Figure 47.

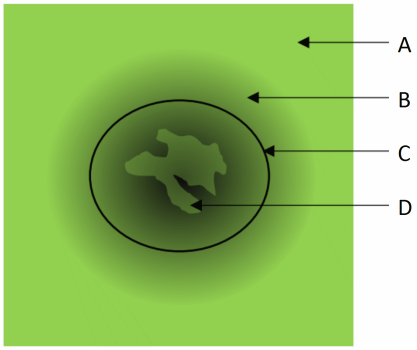

Fig. 47. A scheme summarizing typical phenomena induced by NIR laser irradiation of the dextran-FITC loaded sandwich in a buffer environment. The scheme mimics a photomicrograph in epifluorescence mode acquired shortly after the deactivation of the laser. The regions denoted by arrows correspond to:
***A**: sandwich loaded with dextran-FITC of molecular mass of 4 kDa incubated in buffer*
***B**: the fluorescence drop—an effect manifested by gradually reducing fluorescence intensity in the area irradiated*
***C**: an outline of an area presenting the thermally-triggered shrinking of hybrids, when irradiated by laser*
***D**: the central increase of fluorescence intensity—an effect manifested by increased fluorescence intensity in the region that was transformed by the 'thermally-induced swelling of PEM' during long-lasting irradiation*

Noteworthy, when a sandwich, that is being incubated in the loading solution of dextran-FITC of 4 kDa molecular mass, is irradiated by laser, the effect of fluorescence drop is suppressed while the intensity of the central increase is enhanced (data not presented). This observation can be explained on the basis of the previous conclusions. An **exchange of dextran molecules** between the PEM and the loading solution, which serves as a reservoir of the dextran-FITC, counteracts the depletion of the dextran in the irradiated zone and thereby suppresses the fluorescence drop. The thermally-induced PEM swelling progresses during the laser irradiation of the sandwich regardless of the presence of the loading solution

or the buffer. Therefore, the central increase dominates over the fluorescence drop when the sandwich is irradiated by IR laser at the presence of the loading solution of dextran-FITC.

5. Conclusions

The need for understanding the multi-fractional diffusion motivated the development of software (NBJ-FRAP-1) capable of analysing data of the *fluorescence recovery after photobleaching* (FRAP, sections 4.1–4.4). The software implements a ***simulation–optimization-based approach*** (S-approach) that enables assessment of both single- and multi-fractional diffusion. The approach is based on simulation of a range of possible scenarios of a single-fractional diffusion process in a first step, followed by fitting a linear combination of the simulated data into the data obtained experimentally. A classical approach, based on the analytical solution of molecular diffusion (A-approach), was compared with the S-approach. Both approaches provide robust and well comparable results when samples consist of a single diffusive fraction.

Multi-fractional diffusion was assessed by employing a sample that consists of two diffusive fractions with diffusion coefficients differing by a factor of 100. The S-approach identified the fractions and determined their diffusion coefficients. However, it was not possible to resolve diffusion coefficients that differ by a factor of five or two only. The achievable resolving power of the S-approach is governed by the quality and the quantity of the input data. To reflect this relation, Tikhonov–Phillips regularization of possible solutions is employed.

Finally, the **diffusion rate of protein cytochrome c** in the biopolymer-based HA/PLL PEM is assessed to demonstrate the practical applicability of the S-approach. The result shows that the distribution of the diffusion coefficients of the cytochrome c in the PEM shifts towards slower fractions with progressing time, which indicates changes in interactions between the components of this system.

The results presented demonstrate the potential of the S-approach for comprehensive analysis of molecular diffusion. The capabilities of the S-approach deepen the understanding of the molecular dynamics and thereby foster the development of drug release systems, for example.

Motivated by promising applications in drug release, the research presented in the second part of the thesis (sections 4.5–4.9) focuses on the on-demand **control of molecular transport through the PEM–solution interface.** A remotely and spatiotemporally addressable gate formed by P(NIPAM-AAA) microgel-AuNR hybrid particles deposited on the surface of HA/PLL PEM is therefore fabricated.

A layer of closely packed photoresponsive hybrids attached on the PEM, that serves as a molecular reservoir, is an anticipated prerequisite of the effective control over the molecular transport. Fabrication of such a sandwich structure was a novel task not yet described in the literature. Several approaches for the **fabrication of the sandwich** were tested (section 4.6). Drying of suspension of hybrids on the surface of HA/PLL PEM at low temperature was identified as the optimal approach. It results in a well-attached mono- or multi-layer deposit of closely packed swollen hybrids with relatively low variability of the layer thickness. The hybrids attach to each other and to the PEM surface (section 4.6.4). The thermoresponsivity of the hybrids, as well as their sensitivity to NIR laser irradiation, is not impaired by

their deposition in the sandwich (section 4.7.1). The sandwich is stable in buffer medium for at least several hours.

The mechanism of attachment of the hybrids to the surface of HA/PLL PEM is of interest since it rationalises the strategy of sandwich preparation. The results indicate, that PLL acts as a glue, that binds the components of the sandwich (section 4.6.1). PLL probably leaks from the PLL-rich PEM (section 4.6.3) and mediates a PEM–hybrid attachment as well as a hybrid–hybrid attachment. Elevated concentration of PLL in the hybrid suspension may promote the formation of undesirable hybrid clusters (section 4.6.2). Moreover, the free PLL molecules can penetrate the interior of microgels, resulting in their shrinking (section 4.9.1). This PLL-triggered shrinking can be explained by the compensation of charge of P(NIPAM-AAA) molecules by PLL molecules.

It was documented here, that **irradiation of the sandwich by IR laser** leads to the thermally-triggered shrinking of the deposited hybrids (section 4.7.1). The process is rapid, reversible, and repeatable. A stable thermal profile in the irradiated area of the sandwich is established in a fraction of a second after the laser goes on. The sandwich remains intact when the laser irradiation lasts no more than several tens of seconds. Longer irradiation period causes irreversible swelling and deformation of the PEM in the irradiated area (section 4.7.3).

The gating of the sandwich was tested by FITC-labelled **dextran of 4 kDa** molecular mass. It loads into the PEM in several seconds reaching an equilibrium characterised by the PEM–solution partition constant of 2.4 ± 0.6 ($x \pm s$, $n = 11$) (section 4.9.2). It was found that the hybrid deposit is too permeable to engender a rate-determining step of the molecular transport during the loading, and thereby it is not able to effectively steer the rate of the transport.

The dextran, once loaded in the PEM, may spontaneously release into a surrounding medium. The concentration of dextran in the PEM thereby reduces by approximately no more than few folds per hour of the passive release (section 4.9.2). The **localised control over the molecular transport** was tested by irradiating the sandwich pre-loaded with dextran-FITC by NIR laser. The fluorescence intensity in the irradiated region actually decreases in a range of seconds of the irradiation. The effects plausibly involved in the reduction of fluorescence intensity are: i) thermal dependence of physico-chemical properties of the PEM; ii) accelerated photobleaching in the region heated; iii) thermal dependence of fluorescence quantum yield; or iiii) thermophoresis. These effects probably act simultaneously and influence the fluorescence intensity with various modality (section 4.10).

The findings acquired in the second part of this work that is focused on assembly and study of the novel multicomponent sandwich structure motivate further research on such externally activated drug release systems. Despite the sandwich was shown to be ineffective in controlling the dextran transport, the concept was not refuted. A deeper understanding of the discussed mechanisms would enable further development of this system and harnessing its promising potential.

6. Bibliography

Aggarwal, Neha, Noomi Altgärde, Sofia Svedhem, Kai Zhang, Steffen Fischer, and Thomas Groth. 2014. "Study on Multilayer Structures Prepared from Heparin and Semi-Synthetic Cellulose Sulfates as Polyanions and Their Influence on Cellular Response." *Colloids and Surfaces B: Biointerfaces* 116 (April): 93–103. https://doi.org/10.1016/j.colsurfb.2013.12.043.

Alemán, J., A. V. Chadwick, J. He, M. Hess, K. Horie, R. G. Jones, P. Kratochvíl, et al. 2007. "Definitions of Terms Relating to the Structure and Processing of Sols, Gels, Networks, and Inorganic-Organic Hybrid Materials (IUPAC Recommendations 2007)." *Pure and Applied Chemistry* 79 (10): 1801–29. https://doi.org/10.1351/pac200779101801.

Alevra, Mihai, Peter Schwartz, and Detlev Schild. 2012. "Direct Measurement of Diffusion in Olfactory Cilia Using a Modified FRAP Approach." *PLoS ONE* 7 (7). https://doi.org/10.1371/journal.pone.0039628.

Arbeloa, I. López. 1981. "Dimeric and Trimeric States of the Fluorescein Dianion. Part 1. - Molecular Structures." *Journal of the Chemical Society, Faraday Transactions 2: Molecular and Chemical Physics* 77 (10): 1725–33. https://doi.org/10.1039/F29817701725.

Axelrod, D., D. E. Koppel, J. Schlessinger, E. Elson, and W. W. Webb. 1976. "Mobility Measurement by Analysis of Fluorescence Photobleaching Recovery Kinetics." *Biophysical Journal* 16 (9): 1055–69. https://doi.org/10.1016/S0006-3495(76)85755-4.

Bevington, Philip R., and D. Keith. Robinson. 2003. *Data Reduction and Error Analysis for the Physical Sciences*. McGraw-Hill.

Braeckmans, Kevin, Liesbeth Peeters, Niek N. Sanders, Stefaan C. De Smedt, and Joseph Demeester. 2003. "Three-Dimensional Fluorescence Recovery after Photobleaching with the Confocal Scanning Laser Microscope." *Biophysical Journal* 85 (4): 2240–52. https://doi.org/10.1016/S0006-3495(03)74649-9.

Burke, Susan E., and Christopher J. Barrett. 2003. "PH-Responsive Properties of Multilayered Poly(L-Lysine)/Hyaluronic Acid Surfaces." *Biomacromolecules* 4 (6): 1773–83. https://doi.org/10.1021/bm034184w.

Burmistrova, Anna, and Regine von Klitzing. 2010. "Control of Number Density and Swelling/Shrinking Behavior of P(NIPAM-AAc) Particles at Solid Surfaces." *Journal of Materials Chemistry* 20 (17): 3502–7. https://doi.org/10.1039/b923969c.

Bütergerds, Dörte, Cornelia Cramer, and Monika Schönhoff. 2017. "PH-Dependent Growth Laws and Viscoelastic Parameters of Poly-L-Lysine/Hyaluronic Acid Multilayers." *Advanced Materials Interfaces* 4 (1): 1600592. https://doi.org/10.1002/admi.201600592.

Cinquemani, Eugenio, Vassilis Roukos, Zoi Lygerou, and John Lygeros. 2008. "Numerical Analysis of FRAP Experiments for DNA Replication and Repair." In *Proceedings of the IEEE Conference on Decision and Control*, 155–60. https://doi.org/10.1109/CDC.2008.4738718.

Culbertson, Christopher T., Stephen C. Jacobson, and John M. Ramsey. 2002. "Diffusion Coefficient Measurements in Microfluidic Devices." *Talanta* 56 (2): 365–73. https://doi.org/10.1016/S0039-9140(01)00602-6.

Decher, Gero. 1997. “Fuzzy Nanoassemblies: Toward Layered Polymeric Multicomposites.” *Science* 277 (5330): 1232–37. https://doi.org/10.1126/science.277.5330.1232.

Decher, Gero, and Jong-Dal Hong. 1991. “Buildup of Ultrathin Multilayer Films by a Self-Assembly Process, 1 Consecutive Adsorption of Anionic and Cationic Bipolar Amphiphiles on Charged Surfaces.” *Makromolekulare Chemie. Macromolecular Symposia* 46 (1): 321–27. https://doi.org/10.1002/masy.19910460145.

Elibol, Oguz H., Bobby Reddy, Pradeep R. Nair, Brian Dorvel, Felice Butler, Zahab S. Ahsan, Donald E. Bergstrom, Muhammad A. Alam, and Rashid Bashir. 2009. “Localized Heating on Silicon Field Effect Transistors: Device Fabrication and Temperature Measurements in Fluid.” *Lab on a Chip* 9 (19): 2789–95. https://doi.org/10.1039/b906048k.

Elson, Elliot L., and Douglas Magde. 1974. “Fluorescence Correlation Spectroscopy. I. Conceptual Basis and Theory.” *Biopolymers* 13 (1): 1–27. https://doi.org/10.1002/bip.1974.360130102.

Ernst, Dominique, and Jürgen Köhler. 2013. “Measuring a Diffusion Coefficient by Single-Particle Tracking: Statistical Analysis of Experimental Mean Squared Displacement Curves.” *Physical Chemistry Chemical Physics* 15 (3): 845–49. https://doi.org/10.1039/c2cp43433d.

Fernández-López, Cristina, Lakshminarayana Polavarapu, Diego M. Solís, José M. Taboada, Fernando Obelleiro, Rafael Contreras-Cáceres, Isabel Pastoriza-Santos, and Jorge Pérez-Juste. 2015. “Gold Nanorod-PNIPAM Hybrids with Reversible Plasmon Coupling: Synthesis, Modeling, and SERS Properties.” *ACS Applied Materials and Interfaces*. American Chemical Society. https://doi.org/10.1021/am5087209.

Fernández-Nieves, A., F. J. De las Nieves, and A. Fernández-Barbero. 2004. “Static Light Scattering from Microgel Particles: Model of Variable Dielectric Permittivity.” *Journal of Chemical Physics* 120 (1): 374–78. https://doi.org/10.1063/1.1629281.

Frank, G. A., M. C. Marconi, and H. R. Corti. 2008. “An Alternate Solution of the Fluorescence Recovery Kinetics after Spot-Bleaching for Measuring Diffusion Coefficients. 1. Theory and Numerical Analysis.” *Journal of Solution Chemistry* 37 (11): 1575–91. https://doi.org/10.1007/s10953-008-9330-y.

Geisel, Karen, Walter Richtering, and Lucio Isa. 2014. “Highly Ordered 2D Microgel Arrays: Compression versus Self-Assembly.” *Soft Matter* 10 (40): 7968–76. https://doi.org/10.1039/c4sm01166j.

Glotsos, Dimitris, Spiros Kostopoulos, Kostas Ninos, and Dionisis Cavouras. 2009. “Interpretation of Binding Kinetics in Fluorescence Recovery after Photobleaching Experiments Using a Novel Stochastic Simulation Strategy.” *Molecular Simulation* 35 (14): 1209–14. https://doi.org/10.1080/08927020903015353.

Gordon, G. W., B. Chazotte, X. F. Wang, and B. Herman. 1995. “Analysis of Simulated and Experimental Fluorescence Recovery after Photobleaching. Data for Two Diffusing Components.” *Biophysical Journal* 68 (3): 766–78. https://doi.org/10.1016/S0006-3495(95)80251-1.

Gorelikov, Ivan, Lora M. Field, and Eugenia Kumacheva. 2004. “Hybrid Microgels Photoresponsive in the Near-Infrared Spectral Range.” *Journal of the American Chemical Society* 126 (49): 15938–39. https://doi.org/10.1021/ja0448869.

Gros, M.A. Le, G. McDermott, M. Uchida, C.G. Knoechel, and C.A. Larabell. 2009. “High-Aperture Cryogenic Light Microscopy.” *Journal of Microscopy* 235 (1): 1–8. https://doi.org/10.1111/j.1365-2818.2009.03184.x.

Hallen, Mark A., and Anita T. Layton. 2010. “Expanding the Scope of Quantitative FRAP Analysis.”

Journal of Theoretical Biology 262 (2): 295–305. https://doi.org/10.1016/j.jtbi.2009.10.020.

Hauser, G. I., S. Seiffert, and W. Oppermann. 2008. "Systematic Evaluation of FRAP Experiments Performed in a Confocal Laser Scanning Microscope – Part II: Multiple Diffusion Processes." *Journal of Microscopy* 230 (3): 353–62. https://doi.org/10.1111/j.1365-2818.2008.01993.x.

Heskins, M., and J. E. Guillet. 1968. "Solution Properties of Poly(N-Isopropylacrylamide)." *Journal of Macromolecular Science: Part A - Chemistry* 2 (8): 1441–55. https://doi.org/10.1080/10601326808051910.

Hoare, Todd, and Robert Pelton. 2004. "Highly PH and Temperature Responsive Microgels Functionalized with Vinylacetic Acid." *Macromolecules* 37 (7): 2544–50. https://doi.org/10.1021/ma035658m.

Horecha, Marta, Volodymyr Senkovskyy, Alla Synytska, Manfred Stamm, Alexander I. Chervanyov, and Anton Kiriy. 2010. "Ordered Surface Structures from PNIPAM-Based Loosely Packed Microgel Particles." *Soft Matter* 6 (23): 5980–92. https://doi.org/10.1039/cosm00634c.

Horigome, Koji, and Daisuke Suzuki. 2012. "Drying Mechanism of Poly(N-Isopropylacrylamide) Microgel Dispersions." *Langmuir* 28 (36): 12962–70. https://doi.org/10.1021/la302465w.

Hsu, Bryan B., Samantha R. Hagerman, Kelsey Jamieson, Jovana Veselinovic, Nicholas O'Neill, Eggehard Holler, Julia Y. Ljubimova, and Paula T. Hammond. 2014. "Multilayer Films Assembled from Naturally-Derived Materials for Controlled Protein Release." *Biomacromolecules* 15 (6): 2049–57. https://doi.org/10.1021/bm5001839.

Irrechukwu, Onyinyechi N., and Marc E. Levenston. 2009. "Improved Estimation of Solute Diffusivity through Numerical Analysis of FRAP Experiments." *Cellular and Molecular Bioengineering* 2 (1): 104–17. https://doi.org/10.1007/s12195-009-0042-1.

Jaber, Sarah, Matthias Karg, Anthony Morfa, and Paul Mulvaney. 2011. "2D Assembly of Gold-PNIPAM Core-Shell Nanocrystals." *Physical Chemistry Chemical Physics* 13 (13): 5576–78. https://doi.org/10.1039/c0cp02494e.

Jessel, N., F. Atalar, P. Lavalle, J. Mutterer, G. Decher, P. Schaaf, J.-C. Voegel, and J. Ogier. 2003. "Bioactive Coatings Based on a Polyelectrolyte Multilayer Architecture Functionalized by Embedded Proteins." *Advanced Materials* 15 (9): 692–95. https://doi.org/10.1002/adma.200304634.

Johnson, Michael L., and Martin Straume. 1994. "Comments on the Analysis of Sedimentation Equilibrium Experiments." In *Modern Analytical Ultracentrifugation*, 37–65. Birkhäuser Boston. https://doi.org/10.1007/978-1-4684-6828-1_3.

Jonasson, J. K., J. Hagman, N. Lorén, D. Bernin, M. Nydén, and M. Rudemo. 2010. "Pixel-Based Analysis of FRAP Data with a General Initial Bleaching Profile." *Journal of Microscopy* 239 (2): 142–53. https://doi.org/10.1111/j.1365-2818.2009.03361.x.

Jönsson, Peter, Magnus P. Jonsson, Jonas O. Tegenfeldt, and Fredrik Höök. 2008. "A Method Improving the Accuracy of Fluorescence Recovery after Photobleaching Analysis." *Biophysical Journal* 95 (11): 5334–48. https://doi.org/10.1529/biophysj.108.134874.

Jourdainne, Laurent, Sigolène Lecuyer, Youri Arntz, Catherine Picart, Pierre Schaaf, Bernard Senger, Jean Claude Voegel, Philippe Lavalle, and Thierry Charitat. 2008. "Dynamics of Poly(L-Lysine) in Hyaluronic Acid/Poly(L-Lysine) Multilayer Films Studied by Fluorescence Recovery after Pattern Photobleaching." *Langmuir* 24 (15): 7842–47. https://doi.org/10.1021/la7040168.

Karg, Matthias, Yan Lu, Enrique Carbó-Argibay, Isabel Pastoriza-Santos, Jorge Pérez-Juste, Luis M. Liz-Marzán, and Thomas Hellweg. 2009. "Multiresponsive Hybrid Colloids Based on Gold Nanorods and Poly(NIPAM-Co-Allylacetic Acid) Microgels: Temperature- and PH-Tunable Plasmon Resonance." *Langmuir* 25 (5): 3163–67. https://doi.org/10.1021/la803458j.

Karg, Matthias, Isabel Pastoriza-Santos, Luis M. Liz-Marzán, and Thomas Hellweg. 2006. "A Versatile Approach for the Preparation of Thermosensitive PNIPAM Core–Shell Microgels with Nanoparticle Cores." *ChemPhysChem* 7 (11): 2298–2301. https://doi.org/10.1002/cphc.200600483.

Karg, Matthias, Isabel Pastoriza-Santos, Jorge Pérez-Juste, Thomas Hellweg, and Luis M. Liz-Marzán. 2007. "Nanorod-Coated PNIPAM Microgels: Thermoresponsive Optical Properties." *Small* 3 (7): 1222–29. https://doi.org/10.1002/smll.200700078.

Karg, Matthias, Isabel Pastoriza-Santos, Benito Rodriguez-González, Regine von Klitzing, Stefan Wellert, and Thomas Hellweg. 2008. "Temperature, PH, and Ionic Strength Induced Changes of the Swelling Behavior of PNIPAM-Poly(Allylacetic Acid) Copolymer Microgels." *Langmuir* 24 (12): 6300–6306. https://doi.org/10.1021/la702996p.

Kayitmazer, A. Basak, Daniel Seeman, Burcu Baykal Minsky, Paul L. Dubin, and Yisheng Xu. 2013. "Protein-Polyelectrolyte Interactions." *Soft Matter*. The Royal Society of Chemistry. https://doi.org/10.1039/c2sm27002a.

Keblinski, Pawel, David G. Cahill, Arun Bodapati, Charles R. Sullivan, and T. Andrew Taton. 2006. "Limits of Localized Heating by Electromagnetically Excited Nanoparticles." *Journal of Applied Physics* 100 (5): 054305. https://doi.org/10.1063/1.2335783.

Kishikawa, Yuki, Haruka Shinohara, Kousaku Maeda, Yoshiyuki Nakamura, Simone Wiegand, and Rio Kita. 2012. "Temperature Dependence of Thermal Diffusion for Aqueous Solutions of Monosaccharides, Oligosaccharides, and Polysaccharides." *Physical Chemistry Chemical Physics* 14 (29): 10147–53. https://doi.org/10.1039/c2cp41183k.

Klitzing, Regine von. 2006. "Internal Structure of Polyelectrolyte Multilayer Assemblies." *Physical Chemistry Chemical Physics*. The Royal Society of Chemistry. https://doi.org/10.1039/b607760a.

Klitzing, Regine von, and Helmuth Möhwald. 1996. "Transport through Ultrathin Polyelectrolyte Films." *Thin Solid Films* 284–285 (September): 352–56. https://doi.org/10.1016/S0040-6090(95)08340-5.

Kubitscheck, U., P. Wedekind, and R. Peters. 1998. "Three-Dimensional Diffusion Measurements by Scanning Microphotolysis." *Journal of Microscopy* 192 (2): 126–38. https://doi.org/10.1046/j.1365-2818.1998.00406.x.

Lavalle, Philippe, Valerie Vivet, Nadia Jessel, Gero Decher, Jean Claude Voegel, Philippe J. Mesini, and Pierre Schaaf. 2004. "Direct Evidence for Vertical Diffusion and Exchange Processes of Polyanions and Polycations in Polyelectrolyte Multilayer Films." *Macromolecules* 37 (3): 1159–62. https://doi.org/10.1021/ma035326h.

Lawson, Charles L., and Richard J. Hanson. 1995. *Solving Least Squares Problems*. *Solving Least Squares Problems*. Society for Industrial and Applied Mathematics. https://doi.org/10.1137/1.9781611971217.

Lehmann, Maren, Weronika Tabaka, Tim Möller, Alex Oppermann, Dominik Wöll, Dmitry Volodkin, Stefan Wellert, and Regine von Klitzing. 2018. "DLS Setup for in Situ Measurements of Photoinduced Size Changes of Microgel-Based Hybrid Particles." *Langmuir* 34 (12): 3597–3603. https://doi.org/10.1021/acs.langmuir.7b04298.

Liu, Wen Tso, Jer Horng Wu, Emily Sze Ying Li, and Ezrein Shah Selamat. 2005. "Emission

Characteristics of Fluorescent Labels with Respect to Temperature Changes and Subsequent Effects on DNA Microchip Studies." *Applied and Environmental Microbiology* 71 (10): 6453–57. https://doi.org/10.1128/AEM.71.10.6453-6457.2005.

Mai, Juliane, Saskia Trump, Irina Lehmann, and Sabine Attinger. 2013. "Parameter Importance in FRAP Acquisition and Analysis: A Simulation Approach." *Biophysical Journal* 104 (9): 2089–97. https://doi.org/10.1016/j.bpj.2013.03.036.

Minato, Haruka, Masaki Murai, Takumi Watanabe, Shusuke Matsui, Masaya Takizawa, Takuma Kureha, and Daisuke Suzuki. 2018. "The Deformation of Hydrogel Microspheres at the Air/Water Interface." *Chemical Communications* 54 (8): 932–35. https://doi.org/10.1039/c7cc09603h.

Müller, Paul, Petra Schwille, and Thomas Weidemann. 2014. "PyCorrFit—Generic Data Evaluation for Fluorescence Correlation Spectroscopy." *Bioinformatics* 30 (17): 2532–33. https://www.ncbi.nlm.nih.gov/pmc/articles/PMC4147890/.

Muzzio, Nicolás E., Danijela Gregurec, Eleftheria Diamanti, Joseba Irigoyen, Miguel A. Pasquale, Omar Azzaroni, and Sergio E. Moya. 2017. "Thermal Annealing of Polyelectrolyte Multilayers: An Effective Approach for the Enhancement of Cell Adhesion." *Advanced Materials Interfaces* 4 (1): 1600126. https://doi.org/10.1002/admi.201600126.

Muzzio, Nicolás E., Miguel A. Pasquale, Danijela Gregurec, Eleftheria Diamanti, Marija Kosutic, Omar Azzaroni, and Sergio E. Moya. 2016. "Polyelectrolytes Multilayers to Modulate Cell Adhesion: A Study of the Influence of Film Composition and Polyelectrolyte Interdigitation on the Adhesion of the A549 Cell Line." *Macromolecular Bioscience* 16 (4): 482–95. https://doi.org/10.1002/mabi.201500275.

Nazaran, P., V. Bosio, W. Jaeger, D. F. Anghel, and R. V. Klitzing. 2007. "Lateral Mobility of Polyelectrolyte Chains in Multilayers." In *Journal of Physical Chemistry B*, 111:8572–81. American Chemical Society. https://doi.org/10.1021/jp068768e.

Nerapusri, Verawan, Joseph L. Keddie, Brian Vincent, and Ibraheem A. Bushnak. 2006. "Swelling and Deswelling of Adsorbed Microgel Monolayers Triggered by Changes in Temperature, PH, and Electrolyte Concentration." *Langmuir* 22 (11): 5036–41. https://doi.org/10.1021/la060252z.

Nguyen, Son C., Qiao Zhang, Karthish Manthiram, Xingchen Ye, Justin P. Lomont, Charles B. Harris, Horst Weller, and A. Paul Alivisatos. 2016. "Study of Heat Transfer Dynamics from Gold Nanorods to the Environment via Time-Resolved Infrared Spectroscopy." *ACS Nano* 10 (2): 2144–51. https://doi.org/10.1021/acsnano.5b06623.

Nikoobakht, Babak, and Mostafa A. El-Sayed. 2003. "Preparation and Growth Mechanism of Gold Nanorods (NRs) Using Seed-Mediated Growth Method." *Chemistry of Materials* 15 (10): 1957–62. https://doi.org/10.1021/cm020732l.

Pacholski, Claudia. 2015. "Two-Dimensional Arrays of Poly(N-Isopropylacrylamide) Microspheres: Formation, Characterization and Application." *Z. Phys. Chem* 229 (2): 283–300. https://doi.org/10.1515/zpch-2014-0605.

Pelton, Robert. 2000. "Temperature-Sensitive Aqueous Microgels." *Advances in Colloid and Interface Science*. Elsevier Science Publishers B.V. https://doi.org/10.1016/S0001-8686(99)00023-8.

Pelton, Robert, and Felipe. Chibante. 1986. "Preparation of Aqueous Latices with N-Isopropylacrylamide." *Colloids and Surfaces* 20 (3): 247–56. https://doi.org/10.1016/0166-6622(86)80274-8.

Phillips, David L. 1962. “A Technique for the Numerical Solution of Certain Integral Equations of the First Kind.” *Journal of the ACM (JACM)* 9 (1): 84–97. https://doi.org/10.1145/321105.321114.

Picart, Catherine, Ph Lavalle, P. Hubert, F. J.G. Cuisinier, G. Decher, P. Schaaf, and J. C. Voegel. 2001. “Buildup Mechanism for Poly(L-Lysine)/Hyaluronic Acid Films onto a Solid Surface.” *Langmuir* 17 (23): 7414–24. https://doi.org/10.1021/la010848g.

Picart, Catherine, J. Mutterer, L. Richert, Y. Luo, G. D. Prestwich, P. Schaaf, J. C. Voegel, and P. Lavalle. 2002. “Molecular Basis for the Explanation of the Exponential Growth of Polyelectrolyte Multilayers.” *Proceedings of the National Academy of Sciences of the United States of America* 99 (20): 12531–35. https://doi.org/10.1073/pnas.202486099.

Picart, Catherine, Jerome Mutterer, Youri Arntz, Jean-Claude Voegel, Pierre Schaaf, and Bernard Senger. 2005. “Application of Fluorescence Recovery after Photobleaching to Diffusion of a Polyelectrolyte in a Multilayer Film.” *Microscopy Research and Technique* 66 (1): 43–57. https://doi.org/10.1002/jemt.20142.

Porcel, C., Ph Lavalle, G. Decher, B. Senger, J. C. Voegel, and P. Schaaf. 2007. “Influence of the Polyelectrolyte Molecular Weight on Exponentially Growing Multilayer Films in the Linear Regime.” *Langmuir* 23 (4): 1898–1904. https://doi.org/10.1021/la062728k.

Provencher, Stephen W. 1982. “A Constrained Regularization Method for Inverting Data Represented by Linear Algebraic or Integral Equations.” *Computer Physics Communications* 27 (3): 213–27. https://doi.org/10.1016/0010-4655(82)90173-4.

Reufer, M, P Díaz-Leyva, I Lynch, and F Scheffold. 2009. “Temperature-Sensitive Poly(N-Isopropyl-Acrylamide) Microgel Particles: A Light Scattering Study.” *Eur. Phys. J. E* 28: 165–71. https://doi.org/10.1140/epje/i2008-10387-2.

Sadegh Zadeh, Kouroush. 2011. “A Synergic Simulation-Optimization Approach for Analyzing Biomolecular Dynamics in Living Organisms.” *Computers in Biology and Medicine* 41 (1): 24–36. https://doi.org/10.1016/j.compbiomed.2010.11.002.

Saxton, Michael J. 1997. “Single-Particle Tracking: The Distribution of Diffusion Coefficients.” *Biophysical Journal* 72 (4): 1744–53. https://doi.org/10.1016/S0006-3495(97)78820-9.

Schmidt, Stephan, Thomas Hellweg, and Regine von Klitzing. 2008. “Packing Density Control in P(NIPAM-Co-AAc) Microgel Monolayers: Effect of Surface Charge, PH, and Preparation Technique.” *Langmuir* 24 (21): 12595–602. https://doi.org/10.1021/la801770n.

Schmidt, Stephan, Hubert Motschmann, Thomas Hellweg, and Regine von Klitzing. 2008. “Thermoresponsive Surfaces by Spin-Coating of PNIPAM-Co-PAA Microgels: A Combined AFM and Ellipsometry Study.” *Polymer* 49 (3): 749–56. https://doi.org/10.1016/j.polymer.2007.12.025.

Schmidt, Stephan, Michael Zeiser, Thomas Hellweg, Claus Duschl, Andreas Fery, and Helmuth Möhwald. 2010. “Adhesion and Mechanical Properties of PNIPAM Microgel Films and Their Potential Use as Switchable Cell Culture Substrates.” *Advanced Functional Materials* 20 (19): 3235–43. https://doi.org/10.1002/adfm.201000730.

Seiffert, S., and W. Oppermann. 2005. “Systematic Evaluation of FRAP Experiments Performed in a Confocal Laser Scanning Microscope.” *Journal of Microscopy* 220 (1): 20–30. https://doi.org/10.1111/j.1365-2818.2005.01512.x.

Selin, Victor, John F. Ankner, and Svetlana A. Sukhishvili. 2015. “Diffusional Response of Layer-by-Layer Assembled Polyelectrolyte Chains to Salt Annealing.” *Macromolecules* 48 (12): 3983–90.

https://doi.org/10.1021/acs.macromol.5b00361.

Serpe, Michael J., Clinton D. Jones, and L. Andrew Lyon. 2003. "Layer-by-Layer Deposition of Thermoresponsive Microgel Thin Films." *Langmuir* 19 (21): 8759–64. https://doi.org/10.1021/la034391h.

Smith, Andrew M., Michael C. Mancini, and Shuming Nie. 2009. "Bioimaging: Second Window for in Vivo Imaging." *Nature Nanotechnology*. Nature Publishing Group. https://doi.org/10.1038/nnano.2009.326.

Snowden, Martin J., Babur Z. Chowdhry, Brian Vincent, and Gayle E. Morris. 1996. "Colloidal Copolymer Microgels of N-Isopropylacrylamide and Acrylic Acid: PH, Ionic Strength and Temperature Effects." *Journal of the Chemical Society - Faraday Transactions* 92 (24): 5013–16. https://doi.org/10.1039/ft9969205013.

Song, L., E. J. Hennink, I. T. Young, and H. J. Tanke. 1995. "Photobleaching Kinetics of Fluorescein in Quantitative Fluorescence Microscopy." *Biophysical Journal* 68 (6): 2588–2600. https://doi.org/10.1016/S0006-3495(95)80442-X.

Song, L., C. A. G. O. Varma, J. W. Verhoeven, and H. J. Tanke. 1996. "Influence of the Triplet Excited State on the Photobleaching Kinetics of Fluorescein in Microscopy." *Biophysical Journal* 70 (6): 2959–68. https://doi.org/10.1016/S0006-3495(96)79866-1.

Soumpasis, D. M. 1983. "Theoretical Analysis of Fluorescence Photobleaching Recovery Experiments." *Biophysical Journal* 41 (1): 95–97. https://doi.org/10.1016/S0006-3495(83)84410-5.

South, Antoinette B., Rachel E. Whitmire, Andreós J. Garcióa, and L. Andrew Lyon. 2009. "Centrifugal Deposition of Microgels for the Rapid Assembly of Nonfouling Thin Films." *ACS Applied Materials and Interfaces* 1 (12): 2747–54. https://doi.org/10.1021/am9005435.

Speiser, S., and F. L. Chisena. 1988. "Optical Bistability in Fluorescein Dyes." *Applied Physics B Photophysics and Laser Chemistry* 45 (3): 137–44. https://doi.org/10.1007/BF00695282.

Steger, Katrin, Stefan Bollmann, Frank Noé, and Sören Doose. 2013. "Systematic Evaluation of Fluorescence Correlation Spectroscopy Data Analysis on the Nanosecond Time Scale." *Physical Chemistry Chemical Physics*. The Royal Society of Chemistry. https://doi.org/10.1039/c3cp50644d.

Sugaya, Rei, Bernhard A. Wolf, and Rio Kita. 2006. "Thermal Diffusion of Dextran in Aqueous Solutions in the Absence and the Presence of Urea." *Biomacromolecules* 7 (2): 435–40. https://doi.org/10.1021/bm050545r.

Sullivan, Kelley D., Ania K. Majewska, and Edward B. Brown. 2015. "Single- and Two-Photon Fluorescence Recovery after Photobleaching." *Cold Spring Harbor Protocols* 2015 (1): 13–23. https://doi.org/10.1101/pdb.top083519.

Sustr, David, Antonín Hlaváček, Claus Duschl, and Dmitry Volodkin. 2018. "Multi-Fractional Analysis of Molecular Diffusion in Polymer Multilayers by FRAP: A New Simulation-Based Approach." *Journal of Physical Chemistry B* 122 (3): 1323–33. https://doi.org/10.1021/acs.jpcb.7b11051.

Tang, Z., Y. Wang, P. Podsiadlo, and N. A. Kotov. 2006. "Biomedical Applications of Layer-by-Layer Assembly: From Biomimetics to Tissue Engineering." *Advanced Materials* 18 (24): 3203–24. https://doi.org/10.1002/adma.200600113.

Tannert, Astrid, Sebastian Tannert, Steffen Burgold, and Michael Schaefer. 2009. "Convolution-Based One and Two Component FRAP Analysis: Theory and Application." *European Biophysics Journal* 38

(5): 649–61. https://doi.org/10.1007/s00249-009-0422-4.

Tsuji, Sakiko, and Haruma Kawaguchi. 2005a. "Self-Assembly of Poly(N-Isopropylacrylamide)-Carrying Microspheres into Two-Dimensional Colloidal Arrays." *Langmuir* 21 (6): 2434–37. https://doi.org/10.1021/la047477z.

———. 2005b. "Self-Organization of Poly(N-Isopropylacrylamide)-Carrying Microspheres into Two-Dimensional Colloidal Thin Films." *E-Polymers*. https://doi.org/10.1515/epoly.2005.5.1.804.

Uhlig, Katja, Narayanan Madaboosi, Stephan Schmidt, Magnus S. Jäger, Jürgen Rose, Claus Duschl, and Dmitry V. Volodkin. 2012. "3d Localization and Diffusion of Proteins in Polyelectrolyte Multilayers." *Soft Matter* 8 (47): 11786–89. https://doi.org/10.1039/c2sm26500a.

Uhlig, Katja, Thomas Wegener, Jian He, Michael Zeiser, Johannes Bookhold, Inna Dewald, Neus Godino, et al. 2016. "Patterned Thermoresponsive Microgel Coatings for Noninvasive Processing of Adherent Cells." *Biomacromolecules* 17 (3): 1110–16. https://doi.org/10.1021/acs.biomac.5b01728.

Velk, Natalia, Katja Uhlig, Anna Vikulina, Claus Duschl, and Dmitry Volodkin. 2016. "Mobility of Lysozyme in Poly(L-Lysine)/Hyaluronic Acid Multilayer Films." *Colloids and Surfaces B: Biointerfaces* 147 (November): 343–50. https://doi.org/10.1016/j.colsurfb.2016.07.055.

Viger, Mathieu L., Wangzhong Sheng, Kim Doré, Ali H. Alhasan, Carl Johan Carling, Jacques Lux, Caroline De Gracia Lux, Madeleine Grossman, Roberto Malinow, and Adah Almutairi. 2014. "Near-Infrared-Induced Heating of Confined Water in Polymeric Particles for Efficient Payload Release." *ACS Nano* 8 (5): 4815–26. https://doi.org/10.1021/nn500702g.

Vikulina, A. S., S. T. Aleed, T. Paulraj, Yu A. Vladimirov, C. Duschl, R. Von Klitzing, and D. Volodkin. 2015. "Temperature-Induced Molecular Transport through Polymer Multilayers Coated with PNIPAM Microgels." *Physical Chemistry Chemical Physics* 17 (19): 12771–77. https://doi.org/10.1039/c5cp01213a.

Vinnakota, Kalyan C, David A Mitchell, Robert J Deschenes, Tetsuro Wakatsuki, and Daniel A Beard. 2010. "Analysis of the Diffusion of Ras2 in Saccharomyces Cerevisiae Using Fluorescence Recovery after Photobleaching." *Physical Biology* 7 (2): 026011. https://doi.org/10.1088/1478-3975/7/2/026011.

Vodouhê, Constant, Erell Le Guen, Juan Mendez Garza, Gregory Francius, Christophe Déjugnat, Joëlle Ogier, Pierre Schaaf, Jean Claude Voegel, and Philippe Lavalle. 2006. "Control of Drug Accessibility on Functional Polyelectrolyte Multilayer Films." *Biomaterials* 27 (22): 4149–56. https://doi.org/10.1016/j.biomaterials.2006.03.024.

Vogt, Cédric, Vincent Ball, Jérôme Mutterer, Pierre Schaaf, Jean Claude Voegel, Bernard Senger, and Philippe Lavalle. 2012. "Mobility of Proteins in Highly Hydrated Polyelectrolyte Multilayer Films." *Journal of Physical Chemistry B* 116 (17): 5269–78. https://doi.org/10.1021/jp300028v.

Volodkin, D., A. Skirtach, N. Madaboosi, J. Blacklock, R. von Klitzing, A. Lankenau, C. Duschl, and H. Möhwald. 2010. "IR-Light Triggered Drug Delivery from Micron-Sized Polymer Biocoatings." *Journal of Controlled Release : Official Journal of the Controlled Release Society* 148 (1). https://doi.org/10.1016/j.jconrel.2010.07.031.

Volodkin, Dmitry, Andre Skirtach, and Helmut Möhwald. 2010. "LbL Films as Reservoirs for Bioactive Molecules." In *Advances in Polymer Science*, 240:135–61. Springer, Berlin, Heidelberg. https://doi.org/10.1007/12_2010_79.

Volodkin, Dmitry, Andre Skirtach, and Helmuth Möhwald. 2012. "Bioapplications of Light-Sensitive Polymer Films and Capsules Assembled Using the Layer-by-Layer Technique." *Polymer*

International 61 (5): 673–79. https://doi.org/10.1002/pi.4182.

Waggener, W. C. 1958. "Absorbance of Liquid Water and Deuterium Oxide between 0.6 and 1.8 Microns: Comparison of Absorbance and Effect of Temperature." *Analytical Chemistry* 30 (9): 1569–70. https://doi.org/10.1021/ac60141a039.

Wei, Guangmin, Chuanzhuang Zhao, Javoris Hollingsworth, Zhi Zhou, Fan Jin, Zexin Zhang, He Cheng, and Charles C. Han. 2013. "Mechanism of Two-Dimensional Crystal Formation from Soft Microgel Particles." *Soft Matter* 9 (41): 9924–30. https://doi.org/10.1039/c3sm51927a.

Weiss, Matthias. 2004. "Challenges and Artifacts in Quantitative Photobleaching Experiments." *Traffic* 5 (9): 662–71. https://doi.org/10.1111/j.1600-0854.2004.00215.x.

Weng, Junying, Xiaoyun Li, Ying Guan, X. X. Zhu, and Yongjun Zhang. 2016. "Facile Assembly of Large-Area 2D Microgel Colloidal Crystals Using Charge-Reversible Substrates." *Langmuir* 32 (48): 12876–84. https://doi.org/10.1021/acs.langmuir.6b03359.

Wittemann, Alexander, and Matthias Ballauff. 2004. "Secondary Structure Analysis of Proteins Embedded in Spherical Polyelectrolyte Brushes by FT-IR Spectroscopy." *Analytical Chemistry* 76 (10): 2813–19. https://doi.org/10.1021/ac0354692.

Wu, X., R. H. Pelton, A. E. Hamielec, D. R. Woods, and W. McPhee. 1994. "The Kinetics of Poly(N-Isopropylacrylamide) Microgel Latex Formation." *Colloid & Polymer Science* 272 (4): 467–77. https://doi.org/10.1007/BF00659460.

Xu, Li, Victor Selin, Aliaksandr Zhuk, John F. Ankner, and Svetlana A. Sukhishvili. 2013. "Molecular Weight Dependence of Polymer Chain Mobility within Multilayer Films." *ACS Macro Letters* 2 (10): 865–68. https://doi.org/10.1021/mz400413v.

Yunker, Peter J, Ke Chen, Matthew D Gratale, Matthew A Lohr, Tim Still, and A G Yodh. 2014. "Physics in Ordered and Disordered Colloidal Matter Composed of Poly(N-Isopropylacrylamide) Microgel Particles." *Reports on Progress in Physics* 77 (5): 056601. https://doi.org/10.1088/0034-4885/77/5/056601.

Zadeh, Kouroush Sadegh, Hubert J. Montas, and Adel Shirmohammadi. 2006. "Identification of Biomolecule Mass Transport and Binding Rate Parameters in Living Cells by Inverse Modeling." *Theoretical Biology and Medical Modelling* 3 (October): 36. https://doi.org/10.1186/1742-4682-3-36.

Zavgorodnya, Oleksandra, and Michael J. Serpe. 2011. "Assembly of Poly(N-Isopropylacrylamide)-Co-Acrylic Acid Microgel Thin Films on Polyelectrolyte Multilayers: Effects of Polyelectrolyte Layer Thickness, Surface Charge, and Microgel Solution PH." *Colloid and Polymer Science* 289 (5–6): 591–602. https://doi.org/10.1007/s00396-011-2376-1.

Zhang, Gang, Dayang Wang, Zhong Ze Gu, Jürgen Hartmann, and Helmuth Möhwald. 2005. "Two-Dimensional Non-Close-Packing Arrays Derived from Self-Assembly of Biomineralized Hydrogel Spheres and Their Patterning Applications." *Chemistry of Materials* 17 (21): 5268–74. https://doi.org/10.1021/cm050414x.

Zhao, Mingyan, George Altankov, Urszula Grabiec, Mark Bennett, Manuel Salmeron-Sanchez, Faramarz Dehghani, and Thomas Groth. 2016. "Molecular Composition of GAG-Collagen I Multilayers Affects Remodeling of Terminal Layers and Osteogenic Differentiation of Adipose-Derived Stem Cells." *Acta Biomaterialia* 41 (September): 86–99. https://doi.org/10.1016/j.actbio.2016.05.023.

7. Appendix

7.1 List of common terms

‘**microgel**’—generally: a gel particle with equivalent diameter of approximately 0.1–100 μm. Here specifically: a P(NIPAM-AAA) hydrogel microparticle of about 1.5 μm hydrodynamic diameter at swollen state

‘**hybrid**’—the microgel particle with surface-attached AuNRs

‘**sandwich**’—a structure consisting of PEM with a layer of hybrids deposited on its surface

‘**deposit**’—a layer of hybrids deposited on the PEM surface

‘**basal layer of the deposit**’—the first layer of the deposit in direct contact with the PEM surface

‘**native PEM**’—polyelectrolyte multilayer in the state as obtained after preparation by the layer-by-layer deposition process

‘**plain PEM**’—polyelectrolyte multilayer obtained after drying and rehydration of the native PEM. The term refers to the PEM treated an equivalent way as the PEM during the fabrication of the sandwich by the drying approach while omitting the hybrids.

‘**loading experiment**’—an experimental phase, during which the sample (usually the sandwich or plain PEM) is being exposed to a buffer solution of a target molecule to be loaded into PEM under steady conditions. The molecule typically loaded is dextran-FITC of 4 kDa molecular mass.

‘**release experiment**’—an experimental phase, during which the sample (usually the sandwich or plain PEM) loaded with a target molecule (usually dextran-FITC of 4 kDa molecular mass) is exposed to a washing buffer, that lacks the molecule loaded. The ‘*active phase of the release experiment*’, also referred to as ‘*active washing*’, is the prime phase of the release experiment, during which the loading solution is exchanged for buffer by repeated washing of the sample with buffer. The active phase usually lasts about 50 s. The ‘*passive phase of the release experiment*’, also referred to as ‘*passive washing*’, is the phase following the active phase, during which the washing buffer is let to stand in a chamber with the sample without any agitation.

‘**partition constant**’—ratio of activity of a species in two environments separated by an interface at the equilibrium. Here applied as a ratio between concentration of a target molecule in PEM and in buffer environment at the equilibrium.

‘**irradiation**’—irradiation by CW NIR laser

‘**fluorescence drop**’—a phenomenon that usually occurs during laser irradiation of a sandwich loaded with dextran-FITC. It appears as a gradual reduction of fluorescence intensity in the irradiated area.

‘**central increase of fluorescence intensity**’—a phenomenon that usually occurs after longer-lasting irradiation of a sandwich loaded with dextran-FITC. It appears as an increase of fluorescence intensity in the centre of the irradiated area after the laser is deactivated. It spatially correlates with the area that presents thermally-induced swelling of PEM.

‘**periodic order**’—a regular pattern (typically of hexagonal order) presented by a 2D array of particles attached to the surface.

‘**loose periodic order**’—the periodic order, that includes certain positional freedom of elements of the pattern. It is a transition state between the *periodic order* and the *random distribution.*

‘**close packing**’—a state of the highest possible surface cover density achievable by deposition the spherical particles. It is equivalent to the *hexagonal close-packed* or the *face-centred cubic* lattice. ’**conclusively** ~ ’—the state of close packing is corroborated by the cohesion of particles in clusters or multilayers.

‘**loose packing**’—a state of somehow correlated distribution of particles over a surface with the cover density lower than the maximal possible density—the close packing.

‘**thermally-induced swelling of PEM**’—a phenomenon that appears as swelling of PEM in the region of a sandwich irradiated by IR laser that leads to production of heat in the region.

‘**thermally-triggered shrinking of hybrids**’—a phenomenon following the volume phase transition of the PNIPAM-based hybrid particles triggered by the temperature rising above the transition temperature T_{VPT}.

‘**PLL-triggered shrinking of hybrids**’—a phenomenon that appears as shrinkage of hybrid or microgel particle following the incubation of the particle in a PLL-containing medium.

7.2 List of abbreviations

Chemicals

AuNP	gold nanoparticle
AuNR	gold nanorod
CTAB	cetyltrimethylammonium bromide
CytC	cytochrome c
DMSO	dimethyl sulfoxide
FITC	fluorescein isothiocyanate
HA	hyaluronic acid
PEI	polyethylenimine
PLL	poly(L-lysine)
PMMA	poly(methyl methacrylate)
PNIPAM	poly(*N*-isopropylacrylamide)
P(NIPAM-AAA)	poly(*N*-isopropylacrylamide-*co*-allylacetic acid)
TRIS	tris(hydroxymethyl) aminomethane

Phenomenons, methods, and procedures

AFM	atomic force microscopy
CLSM	confocal laser scanning microscopy
CW	continuous wave
di	deionized
DIC	differential interference contrast
DLS	dynamic light scattering
Em	emission
Ex	excitation
FCS	fluorescence correlation spectroscopy
FRAP	fluorescence recovery after photobleaching
FWHM	full width at half maximum
IR	infra red
LSPR	longitudinal surface plasmon resonance
NA	numerical aperture
NIR	near-infra red
NNLS	non-negative least squares
PEM	polyelectrolyte multilayer

RT	room temperature
ROI	region of interest
SQD	sum of squared deviations
S/N	signal to noise ratio
TEM	transmission electron microscopy
TSPR	transversal surface plasmon resonance
VPT	volume phase transition
1D	one dimensional (spatially)
2D	two dimensional (spatially)
3D	three dimensional (spatially)

Units, quantities, and multiplicative prefixes

Da	dalton (unit of molecular mass)
°C	degree Celsius
h	hour
L	litre
m	metre
M	molar concentration (mol/L)
min	minute
mol	mole (unit of amount of substance)
s	second

x, s, n	arithmetic mean, standard deviation of the sample, sample size
M_w	molar mass
T_{VPT}	volume phase transition temperature

k	kilo- (10^3)
c	centi- (10^{-2})
m	milli- (10^{-3})
μ	micro-(10^{-6})
n	nano- (10^{-9})